

LEPTONS AND PHOTONS IN STRONG ELECTROMAGNETIC FIELDS

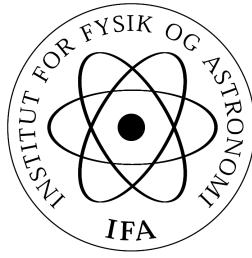


Ph.D Thesis

Tobias Nyholm Wistisen

October 26, 2016

Supervisor: Ulrik I. Uggerhøj
Department of Physics and Astronomy, Aarhus University



Contents

Contents	3
1 Introduction	13
1.1 Units	16
1.2 Publications	16
2 Crystalline Structure, Channeling and radiation emission	19
2.1 Crystal potentials and motion	19
2.2 Classical emission of radiation	24
2.3 Semi-classical method of radiation emission	27
3 Crystalline undulator - The Kostyuk undulator	35
3.1 The crystal and experimental setup	36
3.2 Theoretical modeling, simulations and experimental results	38
4 Channeling of electrons in bent crystals - SLAC experiment	43
4.1 Theory	44
4.2 Experimental setup and procedure	50
4.3 Data analysis and results	53
4.3.1 Multiple scattering of channeled particles parallel to the plane	59
4.3.2 Angular distribution of channeled particle orthogo- nal to the plane	60
4.3.3 Deflection angle of volume reflected particles	61
4.3.4 Efficiency of volume capture	61

4.3.5	Discussion of the dechanneling length and surface transmission	62
4.4	Conclusion	64
5	The Heisenberg-Euler-Schwinger effective Lagrangian and vacuum birefringence	69
5.1	The Heisenberg-Euler-Schwinger effective Lagrangian	70
5.2	The proposed experiment	72
5.3	Vacuum birefringence due to the interaction with an axion .	75
6	An interference phenomenon in nonlinear Compton scattering	79
6.1	Compton scattering as transitions between Volkov states . .	80
6.2	The Semi-classical Operator Method	84
6.3	Compton Interference	90
6.4	General considerations and numerical implementation . . .	91
7	Quantum synchrotron radiation in the case of a field with finite extension	97
7.1	Synchrotron radiation	98
7.2	Discussion of numerical results	107
7.3	The spectrum in the limit of a short extension of the field .	109
7.4	Discussion of experimental investigation and relevance in future colliders	112
8	Classical and quantum radiation reaction	115
8.0.1	2015 CERN NA63 experiment with 10GeV electrons	119
8.0.2	Simulation of the setup	125
8.1	2016 CERN NA63 180 GeV positrons	126
8.1.1	Theory	126
8.1.2	Experiment	131
8.1.3	Deconvoluting the experimental data	135
8.2	MIMOSA detectors and data analysis routines	139
9	Modification of particle production cross sections in strong fields	143
9.1	Theory	144

9.2 Considerations on the A_n functions 153

9.3 Classical approach 156

Bibliography **161**

Summary

This thesis is on the subject of the interaction of electrons and positrons with the electromagnetic field. When an electron or positron interacts with an electromagnetic field one can speak of “strong” versus “weak” fields. If the electron motion due to the field becomes relativistic in its average rest-frame, one can no longer call the field weak and this is what is usually referred to as classical non-linearity or that the field is strong in the classical sense. Another way of seeing the field as being “strong” is in terms of the Schwinger critical field. This is a field strength obtained by combining the fundamental constants of Plancks constant, the speed of light, the electron charge and mass to obtain an electric field strength of 1.3×10^{18} V/m or correspondingly the magnetic field strength of 4.4×10^9 T. This field strength cannot be reached in the laboratory, but with ultra-relativistic particles such field strengths can be reached in the rest-frame of the electron due to Lorentz boosting of the field. If this is the case we refer to it as quantum non-linearity. This thesis deals with a variety of electromagnetic processes where such non-linearities arise, both theoretically and experimentally. The main outcome of this thesis are the experimental results regarding the so-called quantum radiation reaction. That is, the first experimental observation has been made, of multiple high energy photon emissions from high energy positrons interacting with the field of an axially aligned silicon crystal such that we are in both of these non-linearity cases.

Dansk resume

Denne afhandling omhandler elektroners og positroners vekselvirkning med det elektromagnetiske felt. Når en elektron eller positron vekselvirker med et elektromagnetisk felt kan man tale om “stærke” vs. “svage” felter. Hvis elektronens bevægelse pga. feltets indvirkning bliver relativistisk i dens middel hvile-system kan man ikke længere tale om et svagt felt, og dette kaldes normalt klassisk ikke-linearitet, eller at feltet er stærkt i klassisk betydning. En anden måde at se feltet som værende “stærkt” er med henblik på det såkaldte Schwinger kritiske felt. Denne felt styrke opnås ved at kombinere de fundamentale naturkonstanter, Plancks konstant, lysets hastighed, elektronens ladning og masse for så at opnå en feltstyrke på $1.3 \times 10^{18} \text{V/m}$ eller $4.4 \times 10^9 \text{T}$ for det tilsvarende kritiske magnetfelt. Denne feltstyrke kan ikke opnås i laboratoriet, men med ultra-relativistiske partikler kan sådanne feltstyrker nås i elektronens hvilesystem pga. Lorentz sammentrykning af feltlinjerne. Hvis dette er tilfældet taler man om kvante ikke-linearitet. Denne afhandling omhandler et bredt udvalg af elektromagnetiske processer hvor en sådan ikke-linearitet finder sted, både i eksperiment og teori. Hovedresultatet i denne afhandling er de eksperimentelle resultater angående den såkaldte kvante strålingsreaktion. Det vil sige den første eksperimentelle observation er foretaget af gentagne højenergi foton udsendelser fra højenergi positroner som vekselvirker med feltet fra en silicium krystal, rettet ind langs akseren, således at begge de ovenfor nævnte krav til ikke-linearitet er opfyldte.

Acknowledgments

Looking back on the work done during my Ph.D studies, several people come to mind as having had a positive influence. First and foremost my supervisor Ulrik I. Uggerhøj. Ulrik is an experienced experimentalist and his positive outlook and encouragement in pursuing new ideas are admirable. Allan H. Sørensen was often helpful in theoretical questions on radiation emission and read several of my manuscripts before publication for which I am very thankful. Helge Knudsen has been helpful in providing criticism of manuscripts and talks and has been supportful during several CERN experiments. During my stay at SLAC, Uli Wienands acted as my local supervisor, but also collaborator. I enjoyed the company of Uli during our experiments at SLAC which certainly would not have been possible without him. I would like to thank Antonino Di Piazza for his interest in our CERN related experimental research and for the collaboration we have had on the theory of radiation reaction. During my stay at CERN, I enjoyed the exciting talks I had with Daniel Schulte about beam-beam interactions and the CLIC project in general. I would also like to thank Jakob Esberg, a previous Ph.D student of Ulriks group who was a postdoc in the CLIC project during my stay who helped me to quickly obtain an understanding of the field and who I enjoyed many lunch breaks with. During my time as a Ph.D student, the other students in the group, Rune Mikkelsen, Kristoffer K. Andersen, Søren L. Andersen and Trine Poulsen have been sources of both social and academic stimulation which I am grateful for.

Chapter 1

Introduction

The Ph.D project presented in this thesis is composed of several research topics within the same main area of research, namely investigations of radiation emission and/or particle production in “strong” electromagnetic fields by incoming high energy electrons, positrons or photons. We often speak of nonlinear processes in the strong field. A prime example of this is nonlinear Thomson or Compton scattering where incoming photons are scattered by e.g. an electron. When the density of incoming photons is low, the outgoing (scattered) density of photons is proportional to the incoming photon density and the field is “weak”. When the density of incoming photons increases this is no longer the case, and the non-linearity of the process here refers to a nonlinear dependence on the incoming photon density. The overall subject of this thesis are such nonlinear electromagnetic processes. While the case of a laser providing a monochromatic plane-wave field interacting with a beam of electrons is the quintessential example of Thomson/Compton scattering, processes which are completely analogous to these can be investigated via the phenomenon of ‘channeling’ where an incoming electron or positron is trapped in an oscillatory motion between atomic planes or a single atomic string in a single-crystal of e.g. silicon. The reason for this is that it can be shown that the classical motion entirely determines the characteristics of the emitted radiation, regardless of the background field giving rise to this motion. For this reason one can obtain the same radiation emission spectrum from a classical undulator or by scattering in a laser field since in both cases the classical motion is

approximately a sinusoidal transverse motion. Most physicists are familiar with the Liénard-Wiechart potentials of classical electrodynamics and therefore that the motion of the particle determines the radiation characteristics, however from most modern courses in particle physics, it is not obvious that the classical motion plays any central role when doing the calculation in QED, using Feynman diagrams. Here the electromagnetic field is quantized in terms of a traveling wave in vacuum, and by computing the Feynman diagram for Compton scattering one obtains a transition rate proportional to the density of the photons in the incoming wave - the classical motion never comes into play in any obvious way. Therefore in this approach one may think of the incoming field, and not the electron motion, as determining the radiation characteristics. This view is however more connected to the treatment of the quantization of incoming field and treating this as a perturbation, than to the fundamental physics. That the electron motion is fundamental in determining the radiation characteristics also beyond the classical regime, can be seen from the semi-classical method of Baier, Katkov & Strakhovenko, which will be described and used in several chapters of this thesis. This approach does not rely on quantizing the incoming field nor does it treat this field as a perturbation - it is exact in this respect. In chapter 6, chapter 7 and chapter 8 I investigate radiation emission under new circumstances where the field is strong using this method of calculation. In chapter 6 I investigate what happens if an electron collides with not just a single strong laser wave, but two superimposed monochromatic plane waves of different frequency, while in chapter 7 I investigate when it is acceptable to approximate the incoming field as constant, when it is not really constant and calculate how the spectrum changes when this approximation begins to break down. I relate this to the calculations of radiation emission currently in play in future linear colliders such as the Compact Linear Collider (CLIC) at CERN. In chapter 5 we investigate another kind of non-linearity which arises in QED. It is well known that Maxwells equations satisfy the superposition principle, i.e. that the total field is simply the sum of the fields from each source. However due to quantum corrections one can obtain an effective lagrangian of electrodynamics where several nonlinear processes arise such as the breakdown of the superposition principle. Other nonlinear processes which arise from this lagrangian is vacuum breakdown, where a

strong electric field will spontaneously decay due to electron/positron pair production or vacuum birefringence where a weak probing field (e.g. laser wave) travels through a strong external field and experiences an index of refraction which depends on the polarization wrt. the strong external field. In the mentioned chapter we look at vacuum birefringence and consider if an experiment to measure this effect could be designed. In chapter 3 and chapter 4 I describe experiments performed to investigate channeling in modified crystals. In chapter 3 we ask if a specially manufactured silicon crystal can add periodic kicks in the motion of the penetrating particle such that the emitted radiation spectrum is modified because of this. This is once again a nonlinear process since one cannot treat the channeling radiation, and the radiation induced by the periodic kicks, separately - and effects which can be seen as interference between these two arise, as will be seen. This project could, once it has matured, have real-world applications as it is in essence a type of miniature undulator, producing gamma rays. The study presented in chapter 4 does not deal with radiation emission, but looks in detail at the direction of the particles leaving a crystal bent along a circular arc, yielding information on the motion undertaken within the crystal. This study aims to increase the understanding of the dynamics of electrons in such a crystal and potential applications such as beam-extraction or collimation in particle accelerators have been suggested. In chapter 8 theoretical and experimental studies of radiation reaction of high energy electrons and positrons in single crystals as part of the NA63 CERN collaboration are shown. In the classical regime, radiation reaction is the continuous energy loss of a charged particle due to emission of radiation emission. The force due to this radiative energy loss is not present in the Lorentz force, and much controversy has surrounded this problem, since what would seem as the immediate solution to the problem yields problematic and unphysical results (not conserving energy and non-causal behaviour). A solution is thought to have been found to this problem, but it has never been experimentally tested. The central question here is then if we could test this in an experiment. In this chapter I show the design of an experiment to test this using channeling in a silicon crystal and what the experimental and theoretical results are. That such a fundamental problem in a fundamental branch of physics, classical electrodynamics, may finally see experimental tests is exciting. It turned

out, however, that we did not stay in the classical regime when the experiment was carried out, and instead we made a measurement of radiation reaction in the quantum regime which is equally interesting. Radiation reaction in the quantum regime is characterized by the process becoming dominated by the stochastic (as opposed to continuous) emission of photons with high energy, such that the recoil on the emitting particle can not be neglected, and that such emissions happen several times. We plan to redesign a new experiment which will stay within the classical regime of radiation reaction. In chapter 9 I look towards what I think will be an interesting path to follow in order to advance the field of QED in strong fields.

In this thesis several chapters contain a short introduction written for this thesis and then afterwards the content is identical to various papers on which I am first or single author. The paper in question will be mentioned in the introduction to the chapter. In addition it should be mentioned that chapter 2, chapter 3, a short preliminary version of chapter 4, chapter 5, a preliminary version of chapter 6 and section §8.2 were also part of my part A progress report [1].

1.1 Units

In this thesis natural units where $\hbar = c = 1$ and $e^2 = \alpha \simeq \frac{1}{137}$ are used unless otherwise stated. For 4-vectors we employ the $(+, -, -, -)$ metric and the dot product of two 4-vectors is defined as the contraction i.e. $a \cdot b = a^\mu b_\mu$. We use the Feynman slash notation $\not{a} = a_\mu \gamma^\mu$ where γ^μ are the Dirac gamma matrices.

1.2 Publications

I am the primary author of 5 peer reviewed scientific papers:

- Vacuum birefringence by Compton back scattering through a strong field. Phys. Rev. D 88, 053009 – Published 17 September 2013. [2]

- Experimental Realization of a New Type of Crystalline Undulator. Phys. Rev. Lett. 112, 254801 – Published 24 June 2014. [3]
- Interference effect in nonlinear Compton scattering. Phys. Rev. D 90, 125008 – Published 12 December 2014. [4]
- Quantum synchrotron radiation in the case of a field with finite extension. Phys. Rev. D 92, 045045 – Published 31 August 2015. [5]
- Channeling, volume reflection, and volume capture study of electrons in a bent silicon crystal. Phys. Rev. Accel. Beams 19, 071001 – Published 5 July 2016.[6]

In addition I am coauthor of 5 other peer reviewed scientific papers:

- Experimental investigation of the Landau-Pomeranchuk-Migdal effect in low-Z targets. Phys. Rev. D 88, 072007 – Published 15 October 2013. [7]
- Measurements of the spectral location of the structured target resonance for ultra relativistic electrons. Physics Letters B. 732, 1 May 2014, Pages 309–314. [8]
- Observation of Deflection of a Beam of Multi-GeV Electrons by a Thin Crystal. Phys. Rev. Lett. 114, 074801 – Published 19 February 2015. [9]
- Intense and energetic radiation from crystalline undulators. Nuclear Instruments and Methods in Physics Research Section B: Beam Interactions with Materials and Atoms. 355, 15 July 2015, Pages 35–38. [10]
- A method to measure vacuum birefringence at FCC-ee. arXiv preprint arXiv:1605.02861. (To be published in a conference book) [11]

Chapter 2

Crystalline Structure, Channeling and radiation emission

2.1 Crystal potentials and motion

Many of the subjects which I have investigated, and which are described in this thesis, involve the phenomenon of channeling and the radiation emitted during channeling. The experiments presented in chapter 3 and chapter 8 involve radiation emission by an electron/positron interacting with the crystal and therefore a short introduction of the phenomenon of channeling in crystals and classical and quantum radiation emission is appropriate. The aim of this chapter is to introduce concepts which are well established in the field, but which are essential for the understanding of the rest of the thesis which builds upon and extends what is introduced here.

A crystal is a type of solid where the atoms are arranged in a specific repeating pattern. This repeating pattern is described by the unit cell. Of particular importance here, is the diamond cubic lattice which is the crystal structure of Carbon but can also be attained by other elements in the same group, such as silicon and germanium and an alloy containing any proportion of Si-Ge. This structure is the same as two intertwined

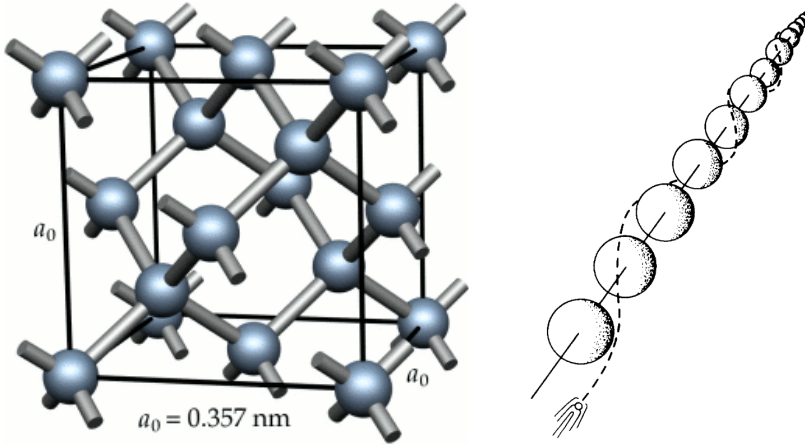


Figure 2.1.1: A figure of the diamond cubic structure for Carbon (left) and a depiction of the channeling of an electron around a string of nuclei (right). Figures borrowed from [12, 13]

FCC (face centered cubic) lattices where one is displaced $\left(\frac{1}{4}, \frac{1}{4}, \frac{1}{4}\right)$ in units of the lattice constant a_0 with respect to the other.

In crystals there are axes and planes of high symmetry. The axes will be denoted by pointy brackets, for instance the $\langle 100 \rangle$ and $\langle 010 \rangle$ axes. A plane is denoted by round parentheses such that the plane orthogonal to the $\langle 100 \rangle$ axis is denoted as the (100) plane. The motion of a high energy particle in a crystalline medium is highly affected if the angle between the initial particle momentum and either a crystalline plane or axis is below some critical value, termed the critical angle and denoted θ_c . Lindhard [14] gives this angle for planar channeling as

$$\theta_c = \sqrt{\frac{4\sqrt{3}Z_1Z_2\alpha Nd_p a_{TF}}{p\beta}}, \quad (2.1.1)$$

where Z_1 and Z_2 are the charge numbers of the target and projectile, d_p is the inter planar distance, p the projectile momentum, α the fine-structure constant, N the number density of atoms and β the particle velocity compared to the speed of light c . $a_{TF} = 0.8853a_0(Z_1^{\frac{2}{3}} + Z_2^{\frac{2}{3}})^{-\frac{1}{2}}$ is a screening length. Below this angle the particle motion in the direction transverse to

the plane/axis can become bound (see figure 2.1.1). This is in principle a tedious problem involving the interaction of the incident particle with an incredible number of atoms. Fortunately, one can often employ the continuum approximation in which the potential from the atoms along an axis or a plane is averaged along the axis/plane. In this case the motion is governed by a relatively simple potential which depends only on the coordinates transverse to the plane/axis. To gain an understanding of this phenomenon, consider an electron or positron of charge q in an electromagnetic field with energy

$$E = \sqrt{(\mathbf{p} - q\mathbf{A})^2 + m^2} + q\varphi, \quad (2.1.2)$$

where \mathbf{p} is the relativistic momentum, \mathbf{A} the vector potential, m the electron mass and φ the electric potential. A continuum potential only depends on 1 or 2 of the 3 spatial coordinates, and one can exploit symmetry to obtain the approximately conserved quantity

$$E_{\perp} = \frac{\mathbf{p}_{\perp}^2}{2\gamma m} + U(\mathbf{x}_{\perp}). \quad (2.1.3)$$

This quantity will be denoted the transverse mechanical energy. If the potential is chosen to be 0 when far away one has the usual condition that the sign of the mechanical energy determines whether the motion is bound or free corresponding to the particle being “channeled” or not. From equation (2.1.3) one sees that the largest angle a particle can have with the z-axis while channeling, in the ultrarelativistic limit is given by

$$\theta_c = \sqrt{\frac{2U_0}{\varepsilon}}. \quad (2.1.4)$$

This is in essence the Lindhard critical angle of equation (2.1.1), where the Lindhard critical angle is obtained using a specific model of the potential, and thus U_0 . Whether one can use a classical theory or if one should use quantum theory when describing the particle motion turns out to be determined by the particle energy. The decisive quantity in answering this question is the quantum number. Bohrs correspondence principle states that in the limit of large quantum numbers and energies, a quantum calculation should reproduce the classical result. If we consider the example of an electron in a magnetic field, we can solve the Dirac equation to obtain

the so-called Landau levels [15]. If the magnetic field \mathbf{B} is along z then the energy is given by

$$E^2 = m^2 + p_z^2 + |q|B(2n + 1) - qB\sigma, \quad (2.1.5)$$

where $\sigma = \pm 1$ the spin quantum number and n the principal quantum number. For motion in a plane perpendicular to the magnetic field, and for large energies we have that $E^2 \simeq 2neB$ such that the quantum number n is

$$n = \gamma^2 \frac{B_c}{2B}, \quad (2.1.6)$$

where γ is the relativistic Lorentz factor and $B_c = \frac{m_e^2}{e}$ is the Schwinger critical magnetic field strength or the ‘‘Schwinger limit’’.

Bohrs correspondence principle then gives us the condition for the motion to be considered classical as

$$\gamma^2 \frac{B_c}{B} \gg 1. \quad (2.1.7)$$

The same condition is found by Baier et. al. [16] but from a more general approach. One can also consider a model closer to what happens in a crystal. A crude model of e.g. the Si (110) planar potential for positrons is that of the harmonic oscillator but with a finite depth, i.e. a cutoff above some energy $U_0 \sim 20\text{eV}$.

$$U(x) = \frac{1}{2}m\omega_p^2 x^2, \quad (2.1.8)$$

where $\omega_p \sim 15\text{eV}$. Considering the problem starting from the Dirac equation (and neglecting spin) one arrives at a Hamiltonian describing the transverse motion very much alike equation (2.1.3)

$$\hat{H} = -\frac{1}{2\gamma m} \frac{d^2}{dx^2} + U(x). \quad (2.1.9)$$

One must then solve the eigenvalue problem $\hat{H}\psi_n = E_n\psi_n$. Inserting equation (2.1.8) and multiplying by γ on both sides reveals that the eigen energies are given by

$$\gamma E_n = \sqrt{\gamma}\omega_p \left(n + \frac{1}{2}\right).$$

This means the level spacing is $\frac{\omega_p}{\sqrt{\gamma}}$ and the number of states is thus approximately $\sqrt{\gamma} \frac{U_0}{\omega_p} \sim \sqrt{\gamma}$. So to apply the classical theory one should have $\sqrt{\gamma} \gg 1$ in this case. Another important aspect of the channeling motion is the phenomenon of dechanneling. In this simple picture of a continuum potential, we have conservation of the transverse mechanical energy and a particle initially channeled stays channeled. In reality, scattering events increase the transverse mechanical energy as the particle moves through the channel, until it is no longer bound - this is dechanneling. This scattering can often be modeled using a simple model which states that particles will scatter in an amorphous material according to a Gaussian distribution with standard deviation θ_{MS} given by [17]

$$\theta_{\text{MS}} = \frac{13.6\text{MeV}}{\varepsilon} \sqrt{\frac{L}{X_0}} \left(1 + 0.038 \ln \frac{L}{X_0} \right), \quad (2.1.10)$$

where X_0 is the radiation length, the length over which a particles energy is reduced to e^{-1} of its initial energy due to Bethe-Heitler bremsstrahlung. The typical length over which dechanneling happens, the dechanneling length, is found by equating the scattering angle due to multiple scattering to the critical angle of equation (2.1.4) and the result is given by [16]

$$L_d = \frac{\alpha U_0 E}{\pi(m c^2)^2} X_0, \quad (2.1.11)$$

which is quite accurate for negative particles, but which will be investigated further in chapter 4. A simple model of dechanneling is obtained by assuming a constant probability per unit length per particle to dechannel, $\frac{1}{L_d}$, giving an exponential decay of the number of particles in the channel [18], [19],

$$N(z) = N_0 e^{-\frac{z}{L_d}}. \quad (2.1.12)$$

While $\sqrt{\gamma} \frac{U_0}{\omega_p} \gg 1$ is the condition for the motion to be considered classical, the process of radiation emission can still be of quantum character. At large energies/strong fields, this turns out to be the case in channeling. In [20] a treatment of an electron in a “strong” monochromatic plane wave field is treated exactly, yielding the well-known Volkov states. Here it is seen that quantum effects will become important when the parameter

$$\chi = \frac{e\sqrt{\langle (F_{\mu\nu}p^\nu)^2 \rangle}}{m^3}, \quad (2.1.13)$$

deviates significantly from zero. $F_{\mu\nu}$ is the electromagnetic field tensor, p^ν the electron four-momentum and m its mass. For a high energy electron in an electric field this is $\chi \sim \gamma \frac{E}{E_c}$, where $E_c = B_c$.

A different approach to the treatment of radiation emission in the quantum regime is that of the semi-classical operator method [16]. This method treats the motion classically, but the radiation emission quantum mechanically making it an ideal approach to treating channeling radiation from high energy electrons or positrons. In section §2.2 a numerical procedure for the calculation of radiation using the purely classical theory is given - but because of the similarity to the semi-classical operator method, this approach can be extended, as will be seen in section §2.3 and then further in chapter 6 where the similarity to the classical formula will be shown.

2.2 Classical emission of radiation

I have written a piece of computer code in C/C++ which can calculate the radiation emission of relativistic particles in many different circumstances. Here I will outline the theory on which this program is based when in the classical regime. Classically the radiation emission is given by the integral [21]

$$\frac{d^2 I}{d\omega d\Omega} = \frac{e^2}{4\pi^2} \left| \int_{-\infty}^{\infty} \mathbf{f}(t, \mathbf{n}) e^{i\omega(t - \mathbf{n} \cdot \mathbf{x}(t))} dt \right|^2, \quad (2.2.1)$$

$$\mathbf{f}(t, \mathbf{n}) = \frac{\mathbf{n} \times [(\mathbf{n} - \mathbf{v}) \times \dot{\mathbf{v}}]}{(1 - \mathbf{v} \cdot \mathbf{n})^2}. \quad (2.2.2)$$

Here dI is the emitted energy within the frequency and solid angle range $d\omega$ and $d\Omega$. \mathbf{n} is the direction of emission, $\mathbf{x}(t)$ is the trajectory i.e. the solution of the Lorentz-force equation and $\mathbf{v} = \dot{\mathbf{x}}$. The Lorentz-force

$$\mathbf{F} = q(\mathbf{E} + \mathbf{v} \times \mathbf{B}), \quad (2.2.3)$$

where \mathbf{E} and \mathbf{B} are the electric and magnetic fields and \mathbf{v} the velocity, along with $\dot{\gamma} = \frac{e}{m} \mathbf{E} \cdot \mathbf{v}$ gives the following coupled equations

$$\begin{pmatrix} \ddot{\mathbf{x}} \\ \dot{\gamma} \end{pmatrix} = \begin{pmatrix} \frac{1}{\gamma m} \mathbf{F}(\mathbf{x}, \mathbf{v}) - \frac{\dot{\gamma}}{\gamma} \mathbf{v} \\ \frac{e}{m} \mathbf{E} \cdot \mathbf{v} \end{pmatrix}. \quad (2.2.4)$$

When solving this numerically for an ultra relativistic particle in a continuum potential, one must take into consideration that one direction of motion is considerably different in size than the others. As z was chosen as the initial direction of the particle, we must solve for the deviation from the motion of a free particle, meaning I write $\delta z(t) = z(t) - \beta_0 t$ and $\delta v_z(t) = v_z(t) - \beta_0$ where $\beta_0 \simeq 1 - \frac{1}{2\gamma^2}$ is the initial velocity of the particle and $\gamma = \varepsilon/m$. Similar problems arise in the radiation integral - one encounters relatively small differences between large numbers. I perform a series expansion in the involved parameters in equation (2.2.2) while keeping only the leading order in the “small” quantities, θ , $\frac{1}{\gamma}$, $\mathbf{v}_\perp(t)$, $\delta v_z(t)$ where vectors with subscript \perp , denote the vectors subtracted their z -component. I have defined $\mathbf{n}_\perp = (\theta_x, \theta_y)$, $\theta^2 = \theta_x^2 + \theta_y^2$ and since these are small quantities we have $n_z = \sqrt{1 - \theta^2} \simeq 1 - \frac{\theta^2}{2}$. For the components of \mathbf{f} of equation (2.2.2) this yields

$$f_x = g \left\{ \theta_y [(\theta_x - v_x) \dot{v}_y - (\theta_y - v_y) \dot{v}_x] - \left(\frac{1}{2\gamma^2} - \frac{\theta^2}{2} - \delta v_z \right) \dot{v}_x + (\theta_x - v_x) \delta \dot{v}_z \right\} \quad (2.2.5)$$

$$f_y = g \left\{ (\theta_y - v_y) \delta \dot{v}_z - \left(\frac{1}{2\gamma^2} - \frac{\theta^2}{2} - \delta v_z \right) \dot{v}_y - \theta_x [(\theta_x - v_x) \dot{v}_y - (\theta_y - v_y) \dot{v}_x] \right\} \quad (2.2.6)$$

$$f_z = g \left\{ \theta_x \left[\left(\frac{1}{2\gamma^2} - \frac{1}{2} \theta^2 - \delta v_z \right) \dot{v}_x - (\theta_x - v_x) \delta \dot{v}_z \right], - \theta_y \left[(\theta_y - v_y) \delta \dot{v}_z - \left(\frac{1}{2\gamma^2} - \frac{1}{2} \theta^2 - \delta v_z \right) \dot{v}_y \right] \right\} \quad (2.2.7)$$

where we have defined

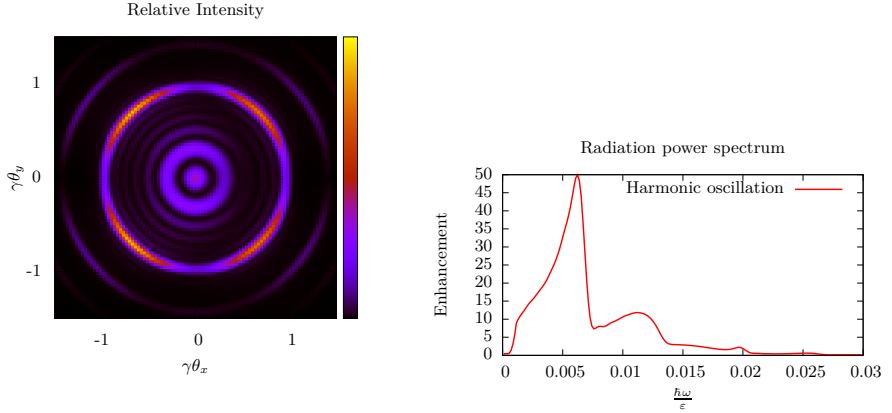


Figure 2.2.1: (Left) The angular distribution of radiation at $\omega/\varepsilon = 0.0075$. (Right) The radiation spectrum of a 10 GeV electron in a harmonic potential with $\omega_p = 15\text{eV}$ with amplitude 0.6\AA corresponding to an undulator parameter of $K \sim 0.6$. Enhancement is with respect to the Bethe-Heitler bremsstrahlung formula.

$$g = \left(\frac{1}{2\gamma^2} + \frac{\theta^2}{2} - \delta v_z - \mathbf{n}_\perp \cdot \mathbf{v}_\perp \right)^{-2}. \quad (2.2.8)$$

Similarly, the exponential phase becomes

$$\omega(t - \mathbf{n} \cdot \mathbf{x}(t)) = \omega \left(\left(\frac{1}{2\gamma^2} + \frac{\theta^2}{2} \right) t - \delta z(t) - \mathbf{n}_\perp \cdot \mathbf{x}_\perp(t) \right). \quad (2.2.9)$$

The procedure is then for each frequency ω to calculate an angular distribution as seen in figure 2.2.1, and then integrate it. A C/C++ program was written to do this. It uses the GSL library for solving the equations of motion equation (2.2.4) and a piece of code which utilizes an Nvidia GPU to calculate the radiation integral of equation (2.2.1) for each direction \mathbf{n} in parallel. It is natural to compare the channeling radiation to that of the Bethe-Heitler bremsstrahlung formula which is given by [22]

$$\frac{dI}{d\omega} = \frac{16}{3} Z_2^2 \alpha r_e^2 L \left(1 - \frac{\omega}{\varepsilon} + \frac{3}{4} \left(\frac{\omega}{\varepsilon}\right)^2\right) \ln(183 Z_2^{-\frac{1}{3}}), \quad (2.2.10)$$

where $r_e = \frac{\alpha}{m}$ is the classical electron radius and L the target thickness. 'Enhancement' will thus denote the ratio of a spectrum to the Bethe-Heitler spectrum given by equation (2.2.10).

2.3 Semi-classical method of radiation emission

In this section I will show the derivation leading to the formula for the radiated energy in the semi-classical method of Baier, Katkov & Strakhovenko. This method is at the center of many of the calculations in the following chapters and is included here for completeness, since then it is seen how the results obtained in chapter 6 follow from first principles. The derivation shown here follows almost completely that found in [15] but with a few details added to make it easier to follow.

The Dirac equation can be written as

$$i \frac{\partial \psi}{\partial t} = (\boldsymbol{\alpha} \cdot \hat{\mathbf{p}} + \beta m) \psi, \quad (2.3.1)$$

where ψ is the 4-component wave-function and $\boldsymbol{\alpha}$ and β are the Dirac matrices. It is well known that the electron solution to this equation is then

$$\psi_{e^-} = \frac{1}{\sqrt{2E}} u(\mathbf{p}) e^{-iEt} e^{i\mathbf{p}\cdot\mathbf{x}}, \quad (2.3.2)$$

where

$$u(p) = \begin{pmatrix} \sqrt{E+m} w \\ \frac{\boldsymbol{\sigma}\cdot\mathbf{p}}{\sqrt{E+m}} w \end{pmatrix}, \quad (2.3.3)$$

and where w is a two-component spinor which can be chosen freely and $\boldsymbol{\sigma}$ represents the 3 Pauli spin matrices. The semi-classical approach is then to replace the quantum numbers E and \mathbf{p} with their operator counterparts and $e^{i\mathbf{p}\cdot\mathbf{x}}$ by a semi-classical wave-function of a spinless particle, denoted $\phi(\mathbf{r})$ such that

$$\psi = \frac{1}{\sqrt{2\hat{H}}} u(\hat{\mathbf{p}}) e^{-i\hat{H}t} \phi(\mathbf{r}), \quad (2.3.4)$$

where

$$\hat{H} = \sqrt{(\hat{\mathbf{p}} - q\mathbf{A})^2 + m^2}, \quad (2.3.5)$$

and where \mathbf{A} then describes the external field. The external field is therefore included in the wave-function of the electron as opposed to using the free wave-functions and treating the external field using perturbation theory. One then calculates the probability dP of emission using the first order transition matrix element from time-dependent perturbation theory such that the differential transition probability is given by

$$dP = \sum_f \left| \int V_{fi}(t) dt \right|^2 \frac{d^3k}{(2\pi)^3}, \quad (2.3.6)$$

where the summation extends over all final states and d^3k is the volume element of the emitted photon momentum \mathbf{k} and where the matrix element $V_{fi}(t)$ is given by

$$V_{fi}(t) = -e \sqrt{\frac{2\pi}{\omega}} \int \psi_f^\dagger(t, \mathbf{r}) e^{i(\omega t - \mathbf{k} \cdot \mathbf{r})} (\mathbf{e}^* \cdot \boldsymbol{\alpha}) \psi_i(t, \mathbf{r}) d^3x, \quad (2.3.7)$$

where \mathbf{e} is the polarization vector of the emitted photon, ψ_i , ψ_f are the initial and final electron states and ω the energy of the emitted photon. This means the photon emission is treated to first order in perturbation theory, while the incoming field or 'background' field is included exactly through the wave-functions ψ . This can be rewritten as

$$V_{fi}(t) = -e \sqrt{\frac{2\pi}{\omega}} \langle f | \hat{Q}(t) | i \rangle e^{i\omega t}, \quad (2.3.8)$$

where $|i\rangle$ corresponds to the state with wave-function $\phi_i(\mathbf{r})$ and

$$\begin{aligned}\hat{Q} &= e^{i\hat{H}t} e^i \frac{u_f^\dagger(\hat{\mathbf{p}})}{\sqrt{2\hat{H}}} (\mathbf{e}^* \cdot \boldsymbol{\alpha}) e^{-i\mathbf{k} \cdot \hat{\mathbf{r}}} \frac{u_i(\hat{\mathbf{p}})}{\sqrt{2\hat{H}}} e^{-i\hat{H}t} \\ &= \frac{u_f^\dagger(\hat{\mathbf{p}}(t))}{\sqrt{2\hat{H}(t)}} (\mathbf{e}^* \cdot \boldsymbol{\alpha}) e^{-i\mathbf{k} \cdot \hat{\mathbf{r}}(t)} \frac{u_i(\hat{\mathbf{p}}(t))}{\sqrt{2\hat{H}(t)}}, \quad (2.3.9)\end{aligned}$$

where in the last equation the operators are now the Heisenberg time dependent operators due to the sandwiching between the $e^{\pm i\hat{H}t}$ operators. Using equation (2.3.6) we obtain

$$\begin{aligned}dP &= \frac{e^2 d^3 k}{4\pi^2 \omega} \sum_f \iint dt_1 dt_2 e^{i\omega(t_1-t_2)} \langle i | \hat{Q}^\dagger(t_2) | f \rangle \langle f | \hat{Q}(t_1) | i \rangle \\ &= \frac{e^2 d^3 k}{4\pi^2 \omega} \iint dt_1 dt_2 e^{i\omega(t_1-t_2)} \langle i | \hat{Q}^\dagger(t_2) \hat{Q}(t_1) | i \rangle\end{aligned}$$

where we used the completeness of the states $\phi(\mathbf{r})$. The crux of the semi-classical method is then to make use of the non-commutativity of the operators in the product $\hat{Q}^\dagger(t_2)\hat{Q}(t_1)$ and recognize that $\langle i | \dots | i \rangle$ gives the expectation value, such that when the non-commutativity has been exploited, the operators can be replaced by their classical values as functions of time. Multiplying by ω on both sides we obtain the differential energy emitted $dI = \omega dP$

$$dI = \frac{e^2 d^3 k}{4\pi^2} \iint dt_1 dt_2 e^{-i\omega(t_2-t_1)} \langle i | \hat{Q}^\dagger(t_2) \hat{Q}(t_1) | i \rangle. \quad (2.3.10)$$

Now we denote $\hat{Q}(t_1) = \hat{Q}_1$ and we would like to bring $\hat{Q}_2^\dagger \hat{Q}_1$ on the form

$$\hat{Q}_2^\dagger \hat{Q}_1 = \hat{R}_2^\dagger e^{i\mathbf{k} \cdot \hat{\mathbf{r}}_2} e^{-i\mathbf{k} \cdot \hat{\mathbf{r}}_1} \hat{R}_1. \quad (2.3.11)$$

By looking at equation (2.3.9) we see that we must consider how $e^{-i\mathbf{k} \cdot \hat{\mathbf{r}}(t)}$ commutes with the preceding operator. We recall that this is the displacement operator in momentum space such that

$$\hat{\mathbf{p}} e^{-i\mathbf{k} \cdot \hat{\mathbf{r}}} = e^{-i\mathbf{k} \cdot \hat{\mathbf{r}}} (\hat{\mathbf{p}} - \mathbf{k}), \quad (2.3.12)$$

$$\hat{H}(\hat{\mathbf{p}})e^{-i\mathbf{k}\cdot\hat{\mathbf{r}}} = e^{-i\mathbf{k}\cdot\hat{\mathbf{r}}}\hat{H}(\hat{\mathbf{p}} - \mathbf{k}). \quad (2.3.13)$$

Therefore we can write

$$\hat{Q}(t) = e^{-i\mathbf{k}\cdot\hat{\mathbf{r}}}\hat{R}(t), \quad (2.3.14)$$

where

$$\hat{R}(t) = \frac{u_f^\dagger(\hat{\mathbf{p}}')}{\sqrt{2\hat{H}'}}(e^* \cdot \boldsymbol{\alpha}) \frac{u_i(\hat{\mathbf{p}})}{\sqrt{2\hat{H}}},$$

and $\hat{\mathbf{p}}' = \hat{\mathbf{p}} - \hat{\mathbf{k}}$, $\hat{H}' = \hat{H} - \omega$. Now we must consider the commutativity of the operator between \hat{R}_2^\dagger and \hat{R}_1 in equation (2.3.11) and we therefore define

$$\hat{L}(\tau) = e^{-i\omega\tau}e^{i\mathbf{k}\cdot\hat{\mathbf{r}}_2}e^{-i\mathbf{k}\cdot\hat{\mathbf{r}}_1}, \quad (2.3.15)$$

where $\tau = t_2 - t_1$. Since $\hat{\mathbf{r}}_2$ is the $\hat{\mathbf{r}}_1$ operator at a time τ later in time we can use the time-shift operator $e^{i\mathbf{k}\cdot\hat{\mathbf{r}}_2} = e^{i\hat{H}\tau}e^{i\mathbf{k}\cdot\hat{\mathbf{r}}_1}e^{-i\hat{H}\tau}$ and therefore

$$\begin{aligned} \hat{L}(\tau) &= e^{-i\omega\tau}e^{i\hat{H}\tau}e^{i\mathbf{k}\cdot\hat{\mathbf{r}}_1}e^{-i\hat{H}\tau}e^{-i\mathbf{k}\cdot\hat{\mathbf{r}}_1} \\ &= e^{i(\hat{H}-\omega)\tau}e^{-i\hat{H}(\hat{\mathbf{p}}_1-\mathbf{k})\tau} \end{aligned} \quad (2.3.16)$$

then

$$\begin{aligned} \frac{d\hat{L}}{d\tau} &= e^{i(\hat{H}-\omega)\tau}i(\hat{H} - \omega - \hat{H}(\hat{\mathbf{p}}_1 - \mathbf{k}))e^{-i\hat{H}(\hat{\mathbf{p}}_1-\mathbf{k})\tau} \\ &= i(\hat{H} - \omega - \hat{H}(\hat{\mathbf{p}}_2 - \mathbf{k}))e^{i(\hat{H}-\omega)\tau}e^{-i\hat{H}(\hat{\mathbf{p}}_1-\mathbf{k})\tau} \\ &= i(\hat{H} - \omega - \hat{H}(\hat{\mathbf{p}}_2 - \mathbf{k}))\hat{L}(\tau). \end{aligned} \quad (2.3.17)$$

We are now in a position where we can replace the operators by their classical values such that

$$\begin{aligned}
 \varepsilon(\mathbf{p}_2 - \mathbf{k}) &= \sqrt{(\mathbf{p}_2 - \mathbf{k})^2 + m^2} \\
 &= \sqrt{\varepsilon'^2 + 2(\omega\varepsilon - \mathbf{k} \cdot \mathbf{p}_2)} \\
 &= \varepsilon' \sqrt{1 + \frac{2(\omega\varepsilon - \mathbf{k} \cdot \mathbf{p}_2)}{\varepsilon'^2}} \\
 &\simeq \varepsilon' \left(1 + \frac{(\omega\varepsilon - \mathbf{k} \cdot \mathbf{p}_2)}{\varepsilon'^2} \right) \\
 &= \varepsilon' + \frac{(\omega\varepsilon - \mathbf{k} \cdot \mathbf{p}_2)}{\varepsilon'} \\
 &= \varepsilon' + \frac{\omega\varepsilon}{\varepsilon'} (1 - \mathbf{n} \cdot \mathbf{v}_2). \quad (2.3.18)
 \end{aligned}$$

Where we defined $\varepsilon' = \varepsilon - \omega$, $\mathbf{n} = \mathbf{k}/\omega$ and therefore we can obtain

$$\frac{dL}{d\tau} = -i \frac{\omega\varepsilon}{\varepsilon'} (1 - \mathbf{n} \cdot \mathbf{v}_2) L. \quad (2.3.19)$$

This differential equation has the solution satisfying $L(0) = 1$, given by

$$\begin{aligned}
 L(\tau) &= \exp \left(\int^{\tau} -i \frac{\omega\varepsilon}{\varepsilon'} (1 - \mathbf{n} \cdot \mathbf{v}_2) dt \right) \\
 &= \exp \left(i \frac{\omega\varepsilon}{\varepsilon'} (\mathbf{n} \cdot (\mathbf{r}_2 - \mathbf{r}_1) - \tau) \right). \quad (2.3.20)
 \end{aligned}$$

We can now replace

$$e^{-i\omega\tau} \langle i | \hat{Q}_2^\dagger \hat{Q}_1 | i \rangle \rightarrow R_2^* R_1 \exp \left(i \frac{\omega\varepsilon}{\varepsilon'} (\mathbf{n} \cdot (\mathbf{r}_2 - \mathbf{r}_1) - \tau) \right). \quad (2.3.21)$$

We will now rewrite $R(t)$ as

$$\begin{aligned}
 R(t) &= \frac{1}{2} \frac{1}{\sqrt{\varepsilon'\varepsilon}} u_f^\dagger(\mathbf{p}') (\mathbf{e}^* \cdot \boldsymbol{\alpha}) u_i(\mathbf{p}) \\
 &= \frac{1}{2\sqrt{\varepsilon'\varepsilon}} \begin{pmatrix} \sqrt{\varepsilon'+m} w_f^\dagger & w_f^\dagger \frac{\boldsymbol{\sigma} \cdot \mathbf{p}'}{\sqrt{\varepsilon'+m}} \end{pmatrix} \begin{pmatrix} 0 & \mathbf{e}^* \cdot \boldsymbol{\sigma} \\ \mathbf{e}^* \cdot \boldsymbol{\sigma} & 0 \end{pmatrix} \begin{pmatrix} \sqrt{\varepsilon+m} w_i \\ \frac{\boldsymbol{\sigma} \cdot \mathbf{p}}{\sqrt{\varepsilon+m}} w_i \end{pmatrix} \\
 &= \frac{1}{2\sqrt{\varepsilon'\varepsilon}} \begin{pmatrix} \sqrt{\varepsilon'+m} w_f^\dagger & w_f^\dagger \frac{\boldsymbol{\sigma} \cdot \mathbf{p}'}{\sqrt{\varepsilon'+m}} \end{pmatrix} \begin{pmatrix} \frac{(\mathbf{e}^* \cdot \boldsymbol{\sigma})(\boldsymbol{\sigma} \cdot \mathbf{p})}{\sqrt{\varepsilon+m}} w_i \\ (\mathbf{e}^* \cdot \boldsymbol{\sigma}) \sqrt{\varepsilon+m} w_i \end{pmatrix} \\
 &= \frac{1}{2\sqrt{\varepsilon'\varepsilon}} \left(\sqrt{\frac{\varepsilon'+m}{\varepsilon+m}} w_f^\dagger (\mathbf{e}^* \cdot \boldsymbol{\sigma}) (\boldsymbol{\sigma} \cdot \mathbf{p}) w_i + \sqrt{\frac{\varepsilon+m}{\varepsilon'+m}} w_f^\dagger (\boldsymbol{\sigma} \cdot \mathbf{p}') (\mathbf{e}^* \cdot \boldsymbol{\sigma}) w_i \right). \tag{2.3.22}
 \end{aligned}$$

Now we can use the identity $(\boldsymbol{\sigma} \cdot \mathbf{a})(\boldsymbol{\sigma} \cdot \mathbf{b}) = \mathbf{a} \cdot \mathbf{b} \cdot I + i(\mathbf{a} \times \mathbf{b}) \cdot \boldsymbol{\sigma}$ where I is the 2×2 identity matrix, to obtain

$$\begin{aligned}
 R(t) &= \frac{1}{2\sqrt{\varepsilon'\varepsilon}} \left(\sqrt{\frac{\varepsilon'+m}{\varepsilon+m}} w_f^\dagger (\mathbf{e}^* \cdot \mathbf{p} \cdot I + i[\mathbf{e}^* \times \mathbf{p}] \cdot \boldsymbol{\sigma}) w_i \right. \\
 &\quad \left. + \sqrt{\frac{\varepsilon+m}{\varepsilon'+m}} w_f^\dagger (\mathbf{e}^* \cdot \mathbf{p}' \cdot I + i[\mathbf{p}' \times \mathbf{e}^*] \cdot \boldsymbol{\sigma}) w_i \right) \\
 &= w_f^\dagger (A(t) \cdot I + i\boldsymbol{\sigma} \cdot \mathbf{B}(t)) w_i
 \end{aligned}$$

where we defined

$$A(t) = \frac{\mathbf{e}^* \cdot \mathbf{p}(t)}{2\sqrt{\varepsilon'\varepsilon}} \left(\sqrt{\frac{\varepsilon'+m}{\varepsilon+m}} + \sqrt{\frac{\varepsilon+m}{\varepsilon'+m}} \right), \tag{2.3.23}$$

$$\mathbf{B}(t) = \frac{1}{2\sqrt{\varepsilon'\varepsilon}} \left(\sqrt{\frac{\varepsilon'+m}{\varepsilon+m}} [\mathbf{e}^* \times \mathbf{p}(t)] - \sqrt{\frac{\varepsilon+m}{\varepsilon'+m}} [\mathbf{e}^* \times (\mathbf{p}(t) - \mathbf{k})] \right). \tag{2.3.24}$$

Finally we will consider the combination $R_2^* R_1$

$$\begin{aligned}
 R_2^* R_1 &= w_i^\dagger (A_2 \cdot I + i\boldsymbol{\sigma} \cdot \mathbf{B}_2) w_f w_f^\dagger (A_1 \cdot I + i\boldsymbol{\sigma} \cdot \mathbf{B}_1) w_i \\
 &= \text{Tr} \left[w_i^\dagger (A_2 \cdot I + i\boldsymbol{\sigma} \cdot \mathbf{B}_2) w_f w_f^\dagger (A_1 \cdot I + i\boldsymbol{\sigma} \cdot \mathbf{B}_1) w_i \right] \\
 &= \text{Tr} \left[w_i w_i^\dagger (A_2 \cdot I + i\boldsymbol{\sigma} \cdot \mathbf{B}_2) w_f w_f^\dagger (A_1 \cdot I + i\boldsymbol{\sigma} \cdot \mathbf{B}_1) \right] \\
 &= \text{Tr} [\rho_i (A_2 \cdot I + i\boldsymbol{\sigma} \cdot \mathbf{B}_2) \rho_f (A_1 \cdot I + i\boldsymbol{\sigma} \cdot \mathbf{B}_1)], \quad (2.3.25)
 \end{aligned}$$

where ρ_i and ρ_f are the density matrices of the initial and final electron state respectively. Here we exploited some tricks involving the trace. In the first line, it is obvious that the trace of a number is the number itself, and in the second line we exploited the fact that the trace is invariant under cyclic permutations of a product of matrices. By writing $d^3k = \omega^2 d\omega d\Omega$ we can write the differential emitted energy as

$$\frac{d^2I}{d\omega d\Omega} = \frac{e^2 \omega^2}{4\pi^2} \iint dt_1 dt_2 R_2^* R_1 e^{ik'_\mu (x^\mu(t_1) - x^\mu(t_2))} \quad (2.3.26)$$

where we changed to 4-vector notation such that $k'_\mu = \frac{\varepsilon}{c} k_\mu$ and k_μ is the photon 4-momentum and $x^\mu(t) = (t, \mathbf{r})$. This is the final result as given in [16] before any specific field is considered and is general. No spin or polarization has yet been chosen. It is important to notice that equation (2.3.26) requires a double integration in time to evaluate while equation (2.2.1) only requires a single time integration, making the semi-classical method much heavier numerically if it was to be used in this form. In chapter 6 I will show how equation (2.3.26) can be brought to a form with only a single time integration as well, which makes it numerically applicable.

Chapter 3

Crystalline undulator - The Kostyuk undulator

This chapter is identical to the paper [3] except for the introduction.

I present here a measurement carried out on a new type of crystalline undulator which shows promise as a source of high energy, sharp spectral distribution, tunable source of incoherent radiation. I present also different theoretical models of varying complexity to describe the measurements, and use these models to suggest improvements for future experiments. The inspiration for doing this experiment was provided by the theoretical proof of feasibility as shown in [23]. The usual schemes of making crystalline undulators involve some method of bending the planes or axes of the crystal, altering the usual channeling motion. See [24] for a review of channeling and related phenomena. One scheme, the Large Amplitude, Large Period (LALP), bends the planes such that the bending amplitude and period of the planes is significantly larger than the amplitude and period of the channeling motion. The 'new scheme' consists of having a Short Amplitude, Short Period (SASP) configuration, meaning the predominant motion is still channeling motion, in contrast to the LALP regime. In the SASP regime, the bending of the planes only slightly perturbs the channeling motion trajectory, leading to increased radiation emission at higher photon energies than the usual channeling radiation. Here the bending of the planes is achieved by adding a varying concentration of germanium to a silicon crystal along its direction of growth.

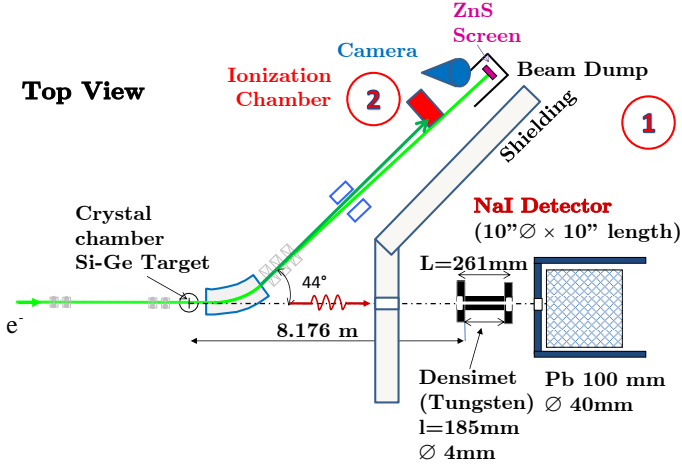


Figure 3.0.1: The experimental setup. The electron beam enters the crystalline target before being bent away by the first magnet. The emitted radiation travels through the collimator and is detected by a NaI detector.

3.1 The crystal and experimental setup

The specially manufactured crystal was grown in the $\langle 001 \rangle$ direction by the method of molecular beam epitaxy at Aarhus University. This method makes it possible to grow a crystal with a varying concentration of different elements as a function of time. This crystal was grown with a mixture of Si and Ge with a concentration of Ge following a triangle function. The crystal has a thickness of $3\mu\text{m}$ of which the last $0.1\mu\text{m}$ is pure Si. The following relation [25] can be found between the amplitude of the bending of the (110) plane a_u , the undulator wavelength λ_u and the average germanium concentration $\bar{\chi}$. Here the concentration is the ratio of number of Ge atoms per volume to the total number of atoms per volume.

$$\bar{\chi} \simeq 170 \frac{a_u}{\lambda_u} \quad (3.1.1)$$

The crystal was made with roughly 10 periods along the (110) -plane, which results in $\lambda_u = 0.41\mu\text{m}$. This value was later measured using

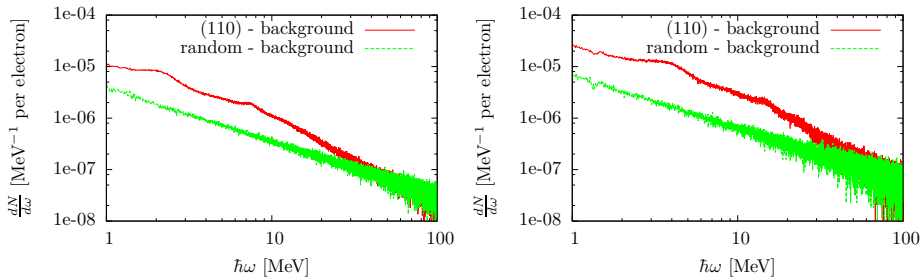


Figure 3.1.1: The photon number spectra for channeling along the (110) plane and particle penetration in a random orientation, subtracted the background for the 600MeV (left) and 855MeV (right) data.

a Rutherford back-scattering method on the sample giving a value of $\lambda_u = 0.43 \pm 0.004 \mu\text{m}$. The minimum and maximum values of the Ge concentration were $(0.3 \pm 0.1)\%$ and $(1.3 \pm 0.1)\%$ respectively. Equation (3.1.1) is for the case when the lower concentration is 0%. In our case we should use $\bar{\chi} = (0.50 \pm 0.14)\%$ giving an amplitude of $a_u = 0.12 \pm 0.034 \text{\AA}$.

The experiment was conducted at the Mainzer Microtron (MAMI). Figure (3.0.1) shows the experimental setup. A well collimated electron beam enters the crystalline target and is afterwards deflected by the first magnet. The emitted radiation travels through the collimation system and is detected by a NaI detector. The beam entered the crystal along the (110) plane but avoiding any direction of axial symmetry. An off-plane measurement was made by turning the crystal to avoid any crystal symmetry directions, as well as a measurement of the background. A linear energy calibration was made based on the known peaks in the background from radioactive decays, and by using radioactive sources. Measurements were performed at beam electron energies of 600MeV and 855MeV, as illustrated in figure (3.1.1). The case of 600MeV electron energy consists of a 3000s measurement, while the 855MeV electron energy is 1000s. At 600MeV, the largest r.m.s. beam spot size was measured to be $138 \mu\text{m}$, and the largest r.m.s. divergence to be $176 \mu\text{rad}$. At this energy the Lindhard critical angle is $\theta_c = 340 \mu\text{rad}$. The beam current was $3 \pm 0.6 \text{pA}$.

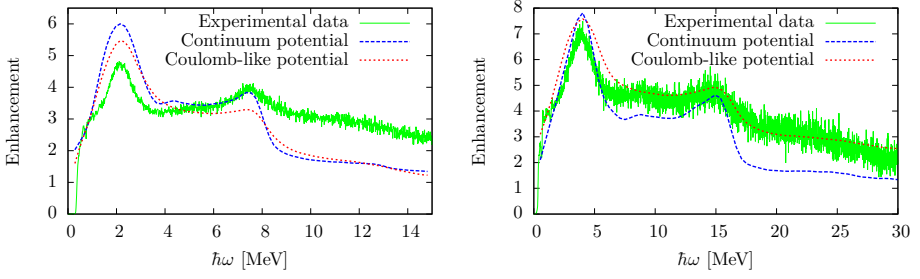


Figure 3.2.1: Comparison of theoretical and experimental radiation yield for the 600MeV (left) and 855MeV (right) data.

3.2 Theoretical modeling, simulations and experimental results

For theoretical comparison and predictions for future experiments, I have developed theoretical models based on numerical solution of the classical equations of motion and radiation emission as shown in section §2.2. I performed the calculation for two potentials, one of which was a continuum planar potential given by [16]

$$U(x) = V[\cosh(\delta(\sqrt{1 + \eta^2} - \sqrt{y^2 + \eta^2})) - 1], \quad (3.2.1)$$

with $V = 3.5$ eV, $\delta = 2.9$, $\eta^2 = 0.0045$ and $y = \frac{2x}{d_{pl}}$ with $d_{pl} = 1.92$ Å. The other potential used was a sum over the potential from each individual atom in the crystal lattice.

$$U(\vec{r}) = \sum_i U_a(\vec{r} - \vec{r}_i), \quad (3.2.2)$$

where the summation is over a diamond cubic lattice. The atomic potential used is:

$$U_a(r) = \frac{Z\alpha}{r} \varphi\left(\frac{r}{a}\right), \quad (3.2.3)$$

where $\varphi\left(\frac{r}{a}\right)$ is a Thomas-Fermi screening function and $a = 0.8853a_0Z^{-\frac{1}{3}}$ is a screening length. The screening function is approximated by the Molière formula [26]

$$\varphi\left(\frac{r}{a}\right) = \sum_{i=1}^3 \alpha_i e^{-\frac{\beta_i r}{a}}, \quad (3.2.4)$$

with coefficients $\{\alpha_i\} = \{0.1, 0.55, 0.35\}$ and $\{\beta_i\} = \{6.0, 1.2, 0.3\}$. Furthermore the atomic positions were displaced in a random direction by sampling a 3d-gaussian distribution to simulate thermal vibrations with r.m.s. amplitude $u = 0.062\text{\AA}$ [27]. The model used to describe the potential of the periodically bent plane due to the periodic addition of germanium is given by

$$U_{\text{bent}}(x, y, z) = U(x, y - a_u \sin(k_u z + \varphi), z) \quad (3.2.5)$$

The beam direction is chosen to be the z -direction and the direction of channeling oscillation as the y -direction. I.e. the potential center follows the path $a_u \sin(k_u z + \varphi)$.

In order to get accurate values for comparison with the experiment, equation (2.2.1) must be integrated over the relevant angular region, depending on the collimation setting in the experiment. Only calculating the emission in the exactly forward direction as is done in [25] does not suffice for experimental comparison. The radiation was calculated on an angular (Cartesian) grid of 20×20 points as this was adequate to achieve convergence.

The two potentials described both have their advantages and disadvantages. The continuum potential model allows for a fast numerical calculation which gives good results in reasonable agreement with the experiment, but it is well known that this does not account for the Bethe-Heitler bremsstrahlung which is usually added to the radiation from the channeling motion. The calculation using the 'full' potential of equation (3.2.2) is considerably slower because the step size when solving the system of differential equations for the trajectory cannot be larger than the typical scale of the variation of the potential - which is less than the size of the atom. It is non-trivial to determine the exact amount of Bethe-Heitler radiation which should be added with this type of undulator crystal. Furthermore

the continuum potential does not take into account the dechanneling process. The more elaborate potential was chosen to deal with these issues, where both Bethe-Heitler bremsstrahlung and dechanneling are inherently included. For the continuum potential, I have added the Bethe-Heitler bremsstrahlung as measured in the 'random' crystal orientation to the calculated result.

A direct fit of the data in the 'random' direction with the Bethe-Heitler formula (see e.g. [24]) shows experimental values that are too low by factors of 15.5 and 8.5 at 600MeV and 855MeV respectively. This is mainly due to an angular collimation performed in the experiment where the opening angle was 0.49mrad corresponding to angles less than $\frac{0.28}{\gamma}$ and $\frac{0.40}{\gamma}$ from the central axis for 600MeV and 855MeV respectively. Classical works (such as [21]) show that at relativistic electron energies and low photon energies $\omega \ll E$, the angular distribution of the intensity of bremsstrahlung is independent of the photon energy ω - barring small corrections. The normalized angular distribution is given as

$$\frac{dP}{d\Omega} = \frac{3\gamma^2}{2\pi} \frac{1 + \gamma^4\theta^4}{(1 + \gamma^2\theta^2)^4}. \quad (3.2.6)$$

Here dP is the differential probability of emission within the solid angle $d\Omega$. Integrating this up to the two angular regions stated gives an expected reduction of 9.85 and 5.53 for 600MeV and 855MeV, respectively. In both cases this means a factor of about ~ 1.5 is unaccounted for. This error is reasonable considering the uncertainty on the beam current and the fact that a slight misalignment of the collimator would further decrease the solid angle of the detected radiation. Considering the size of the multiple scattering angle of 0.134 mrad at 600MeV after traversing the target suggests that this might also have a small effect. The normalization procedure for the theoretical curves is to multiply with the same factor as is necessary for the fit with the Bethe-Heitler formula. I also note that in the simulations a value of $a_u = 0.13 \text{ \AA}$ was used which is well within the experimental uncertainty. It is seen in simulations (see figure (3.2.2)) that the position of the channeling peak in energy moves with varying bending amplitude.

This value of a_u was therefore chosen for good agreement of the channeling peak position - although it makes only a minor difference in comparison

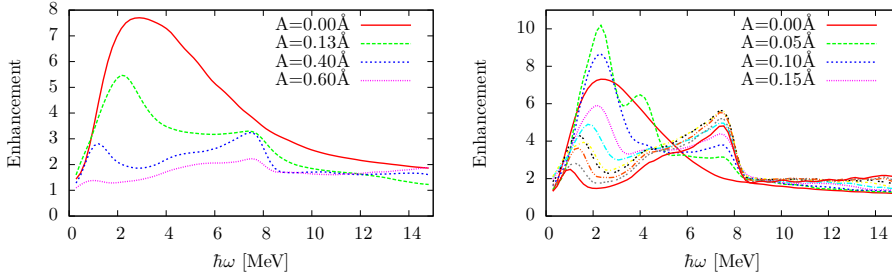


Figure 3.2.2: Calculated radiation spectra for different values of the bending amplitude a_u at 600MeV electron energy using the screened Coulomb potential (left) and using the continuum potential (right). For the continuum potential, the bending amplitude goes from 0\AA to 0.45\AA in steps of 0.05\AA .

to using $a_u = 0.12\text{\AA}$. See figure (3.2.1) for a comparison of theory to the experiment. 'Enhancement' is the ratio of the total radiation spectrum to the Bethe-Heitler spectrum. The leftmost peaks stem from channeling and the rightmost from the undulator motion. The position of the undulator peak considering just forward emission of radiation should be at $2\gamma^2 k_u$, with $k_u = \frac{2\pi}{\lambda_u}$, which agrees well with the experiment. The size of the peaks, however, does disagree significantly. Attributing the factor of ~ 1.5 of deviation in the bremsstrahlung yield to a slight misalignment of the collimator could explain the deviation of the radiation in the 'aligned' case as well. As the collimation angle becomes very narrow in units of $\frac{1}{\gamma}$, the spectral distribution can change significantly, and a misalignment will be more pronounced. For 855MeV the collimation is not quite as narrow in units of $\frac{1}{\gamma}$, and therefore we have better agreement.

In conclusion we remark that the overall agreement between experiment and theory, is good. There is a definite crystalline undulator effect caused by the bending of the planes as can be seen by comparing with the regular channeling spectrum as seen in figure (3.2.2).

Nevertheless this crystal has a relatively low value of a_u , compared with those considered in [25]. This, along with the fact that the calculations in [25] are for the exactly on-axis emission, means that the undulator peak seen in the experiment is not as pronounced. The simulations I have

performed for other values of the bending amplitude a_u as seen in figure (3.2.2) are integrated over a collimation angle of $\frac{1}{\gamma}$, but otherwise with the same parameters as in the experiment. Here it is seen that it is unlikely that the undulator peak will become larger in absolute size by increasing the bending amplitude of the planes but a relative increase to the rest of the spectrum can be achieved which would be desirable. It should also be noted that for larger values of a_u the continuum potential exaggerates the undulator effect in comparison to using the screened Coulomb potential as can be seen by comparing figure (3.2.2). A surprising result is the effect on the shape of the channeling peak. For electrons the channeling radiation spectrum is usually very broad in contrast to the narrow spectral distribution seen here in both the experiment and simulations. These experiments and our simulations therefore show that if the goal is to achieve a narrow spectral distribution it might also be worthwhile to investigate small values of a_u , like 0.05 Å or 0.1 Å at 600MeV, such that these oscillations serve only to disturb the formation of channeling radiation, making it spectrally more narrow as seen in figure (3.2.2).

Chapter 4

Channeling of electrons in bent crystals - SLAC experiment

This chapter is identical to the paper [6] except for the introduction which has been modified and the simulations shown in [6] have been removed since they are not my work and they are not of central importance in what is mainly an experimental paper.

In this chapter I describe experiments, of which some were carried out during my 6-month stay at SLAC, involving electrons channeling in a silicon crystal bent along a circular arc. Unlike the last chapter, radiation emission was not measured in this experiment where we instead measured the angular distribution of the outgoing electrons. In chapter 3 the modification of the electron motion could be inferred from the radiation emission spectrum while not much information would be gained by looking at the electrons leaving the crystal. Since the crystal in the experiment which will be described here is bent along a circular arc, some electrons will follow the bend to the end of the crystal while some will follow the bend for some fraction of the full length of the crystal and yet some will not follow the bend at all. For this reason much information can be gained by “just” measuring the angular distribution of the outgoing electrons.

Channeling in bent crystals has been thoroughly studied for protons with the purpose of e.g. proton extraction at accelerator facilities [28, 29, 30]

and for collimation [31, 32, 33]. Much less is known about the efficiency of channeling of electrons in bent crystals. Here I present a quantitative investigation of channeling and related phenomena in a strongly bent silicon crystal. The ordered structure of the crystal lattice gives unique access to electromagnetic field strengths otherwise experimentally inaccessible [24] which can be manipulated by e.g. bending of the crystal, as in this experiment, or otherwise inducing a strain in the crystal as exploited in certain new types of crystalline undulators as studied in chapter 3 and [3, 34, 35, 36, 37, 38]. Understanding the dynamics of the electron motion in a bent crystal is important both for the application of bent crystals, but also in order to obtain a better understanding of the dynamics in e.g. crystalline undulators. This chapter deals with a more detailed analysis of an experiment and data first published in [9], and examines data taken after the publication of that letter at different beam-energies.

4.1 Theory

An often employed model of the planar (111) continuum potential is the thermally averaged Doyle-Turner potential of the form [39]

$$U(x) = 2\sqrt{\pi}Z_1 \frac{e^2}{a_0} a_0^2 N d_p \sum_{i=1}^4 \frac{a_i}{\sqrt{B_i + \rho^2}} e^{-\frac{x^2}{B_i + \rho^2}}, \quad (4.1.1)$$

where Z_1 is the charge number of the projectile, $\rho = 0.062 \text{ \AA}$ is the r.m.s. thermal vibrational amplitude at room temperature for Si, $a_0 = 0.53 \text{ \AA}$ is the Bohr radius, $B_i = b_i/4\pi^2$ and x is the coordinate transverse to the plane. See table 4.1 for the values of a_i and b_i . A plot of this potential versus transverse position is shown in figure 4.1.1. For Si (111) there are two planar distances given by $d_1 = \frac{a}{4\sqrt{3}}$ and $d_2 = \frac{a\sqrt{3}}{4}$ with $a = 5.43 \text{ \AA}$ being the lattice constant for Si and $d_p = \frac{d_1 + d_2}{2}$.

In a bent crystal, channeling is easily described in a rotating coordinate system such that the x -coordinate is the displacement from the bent channel in the radial direction of the bending arc. This choice of coordinate system gives rise to a centrifugal force. For a relativistic particle this is equivalent to a centrifugal barrier potential of the form

i	1	2	3	4
$a_i[\text{\AA}]$	2.1293	2.533	0.8349	0.3216
$b_i[\text{\AA}^2]$	57.7748	16.4756	2.8796	0.3860

Table 4.1: A table of parameters for the Doyle-Turner potential for the Si potential of equation (4.1.1) found in [39].

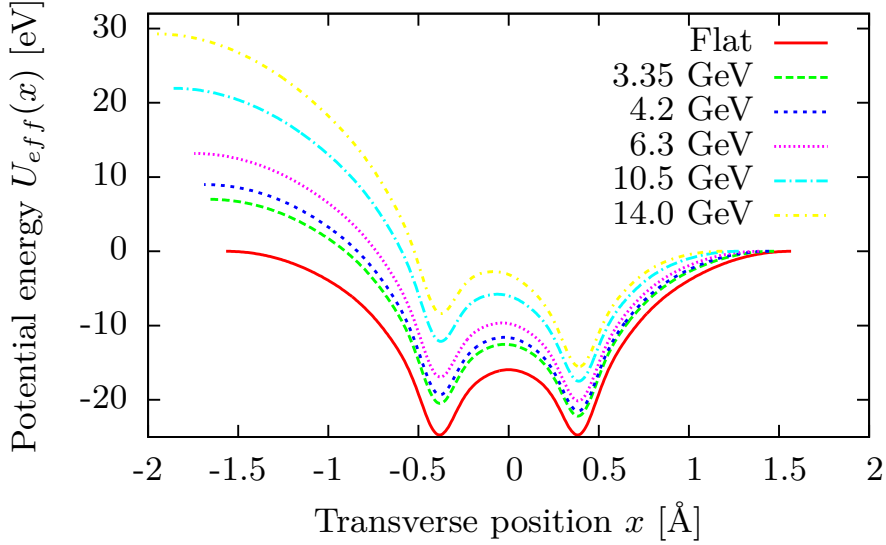


Figure 4.1.1: A plot of the effective potential of equation (4.1.3) for a flat crystal and for the relevant electron energies with bending radius $R = 0.15\text{m}$.

$$U_{\text{CF}}(x) = \frac{Ex}{R}, \quad (4.1.2)$$

where R is the bending radius of the crystal. The motion of the channeled particle is therefore described by an effective potential

$$U_{\text{eff}}(x) = U(x) + \frac{Ex}{R}. \quad (4.1.3)$$

See figure 4.1.1 for plots of the potential for the relevant energies. It is evident that the bending of the crystal reduces the potential depth and thus the effective critical angle in equation (2.1.4). If the centrifugal potential barrier of equation (4.1.2) changes by a significant amount compared to the potential depth of the unbent crystal over an inter planar distance one approaches criticality, and the bending of the crystal can not be treated as a small perturbation to the unbent case. This is closely related to the critical radius, defined as the radius of curvature where the largest value of the field compensates the centrifugal force. In the case of the (111) plane, there are 2 planar distances, and the critical radius of the largest plane is then given by

$$R_c = \frac{Ed_2}{4U_0}. \quad (4.1.4)$$

Typically the critical radius is calculated based on the more precise Moliere or Doyle-Turner potential see e.g. [40], but in analytical formulas for the dependence of e.g. dechanneling length and surface acceptance on the curvature R , the parabolic approximation is used and this is the critical radius in this approximation. From equation (4.1.4) it is seen that the critical radius for 14.0 GeV is 3.3 cm which is comparable in magnitude to the 15 cm radius of curvature of the crystal in this experiment.

Dechanneling

equation (2.1.12) is for the dechanneling length in a straight crystal. This simple model can easily be modified to the case of a bent crystal. From equation (4.1.3) it is seen that the potential depth from the case of a straight crystal is, to first order in $\frac{1}{R}$, reduced by $\frac{Ed_2}{2R} = \frac{2R_{\text{crit}}}{R}U_0$ such that the dechanneling length is instead given by

$$L_{d,b} = \frac{\alpha U_0 E}{\pi m^2} X_0 \left(1 - \frac{2R_{\text{crit}}}{R} \right), \quad (4.1.5)$$

which is applicable while $R \gg 2R_{\text{crit}}$. By comparing this formula obtained by using the parabolic approximation of the transverse potential, to the exact result obtained numerically using the Doyle-Turner potential, there is a discrepancy of at most 13% at the highest energy.

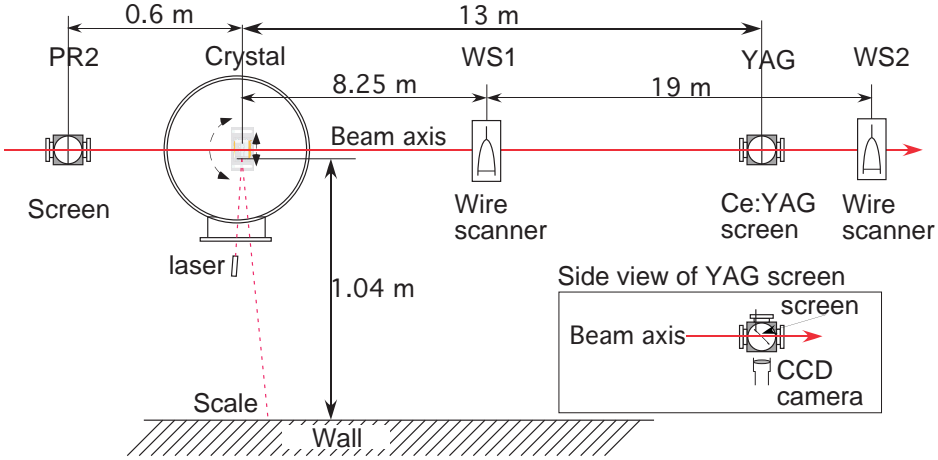


Figure 4.1.2: A sketch of the experimental setup.

Volume capture and volume reflection

The phenomenon of volume capture in a bent crystal is the process where a particle, initially unbound, scatters and loses transverse mechanical energy to become bound - 'captured' in the channel. As such it is closely related to the dechanneling phenomenon [14, 41]. Volume capture occurs when the particle is not aimed directly into the acceptance angle of the channel, but at an angle less than the total bending of the crystal and such that the beam at some point forms a tangent to the bent plane. A rudimentary model of the volume capture efficiency can be obtained in the following manner. An incoming particle is close to the barrier over a distance on the order of $\theta_c R$ and since multiple scattering will randomly increase or decrease the transverse mechanical energy, the probability per unit length per particle to become captured is also $\frac{1}{L_d}$. Therefore the volume capture efficiency should scale as $\frac{\theta_c R}{L_d}$ which gives an energy dependence of $E^{-\frac{3}{2}}$, assuming equation (2.1.11) to be correct [42, 40]. Particles not captured in this manner will remain unbound, but will be deflected with respect to the incoming beam in a direction opposite to the captured particles. This effect is known as volume reflection [43, 44]. In equation (4.1.3) there is an additional linear term in the potential as compared to the

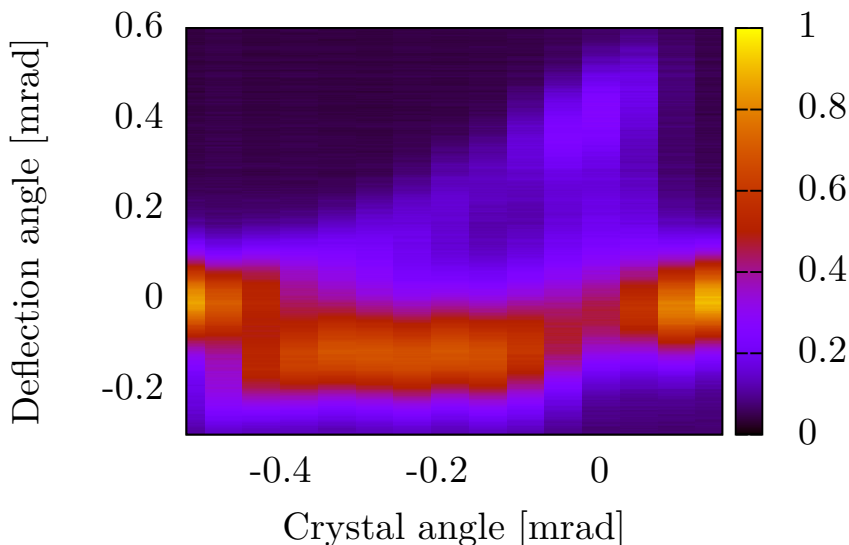


Figure 4.1.3: The probability density relative to the maximum probability density of the deflected particles as a function of the crystal angle for the case of 3.35 GeV electrons.

case of a straight crystal which means a volume reflected particle initially starts with transverse mechanical energy far above the potential barrier until reaching the turning point at which the crystal potential causes an additional deflection of at most the critical angle. Therefore one expects the angle of volume reflection to be similar to the critical angle i.e. with an energy dependence of $E^{-\frac{1}{2}}$.

Surface transmission

For a beam with no angular divergence, the surface transmission can be determined analytically. The surface transmission is defined as the fraction of particles that become transversely bound upon entry into the crystal to the total number of incoming particles. Over a single channel the distribution of incoming particles is uniform, therefore the surface transmission is the ratio of the length over which the potential seen in figure 4.1.1 is

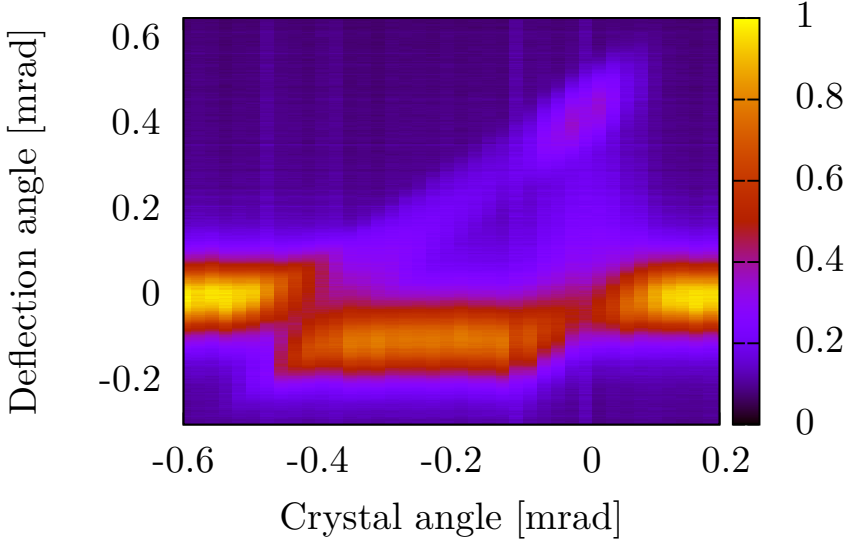


Figure 4.1.4: The probability density relative to the maximum probability density of the deflected particles as a function of the crystal angle for the case of 4.2 GeV electrons.

negative, compared to the length over which the force is periodic which is $2d_p$. By approximating the potential in figure 4.1.1 by parabolas around the point $-d_p$ and d_p one can determine the surface transmission. I write

$$U(x) = -\frac{U_0}{d_p^2}(x + d_p)^2 \text{rect}\left(\frac{x + d_p}{2d_p}\right) - \frac{U_0}{d_p^2}(x - d_p)^2 \text{rect}\left(\frac{x - d_p}{2d_p}\right) + \frac{Ex}{R}, \quad (4.1.6)$$

where $\text{rect}(x)$ is the rectangular function which is 1 if $|x| < \frac{1}{2}$ and 0 otherwise. The leftmost limit of acceptance is determined by the leftmost point a where $U'(a) = 0$ and the rightmost limit b by the condition that $U(b) = U(a)$. The acceptance factor is then $\frac{b-a}{2d_p} = 1 - \sqrt{\frac{R_c}{R}}$. Including the constant fraction that dechannel due to thermal vibration of the nuclei as seen in [40] I obtain

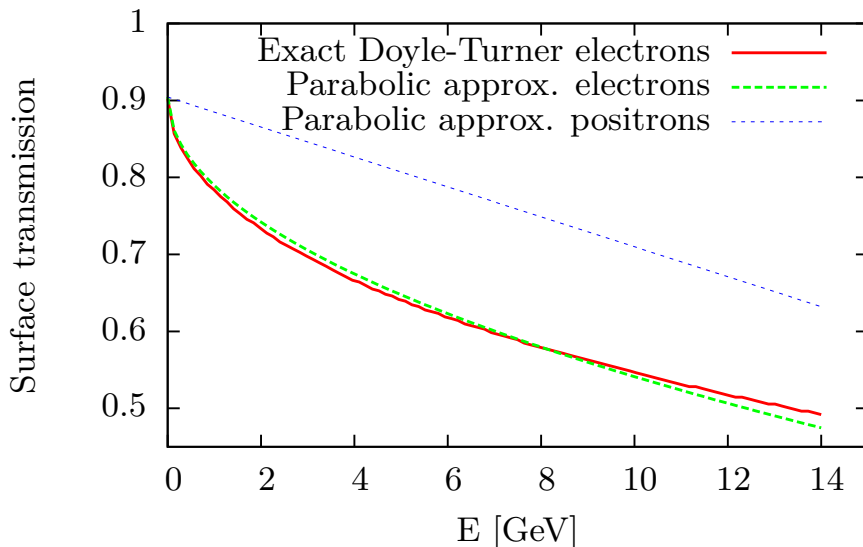


Figure 4.1.5: A figure comparing the surface transmission for electrons using the exact Doyle-Turner potential and the parabolic approximation. I have also plotted the parabolic approximation for positrons to show the difference between positive and negative particles.

$$A = \left(1 - \frac{2u}{d_p}\right) \left(1 - \sqrt{\frac{R_c}{R}}\right), \quad (4.1.7)$$

where $u = 0.062\text{\AA}$ is the thermal vibrational amplitude for Si at room temperature. In figure 4.1.5 I show this formula compared with the exact result obtained numerically using the Doyle-Turner potential.

In table 4.2 I have calculated the values of some of the important parameters for the energies of the experiment.

4.2 Experimental setup and procedure

The silicon (Si) crystal used in this experiment was fabricated [45] at the Sensors and Semiconductor Laboratory at the University of Ferrara with

E [GeV]	3.35	4.2	6.3	10.5	14.0
$L_{d,b}$ [μm]	77	92	124	157	155
A [%]	68	65	59	49	42
θ_c	122	109	89.1	69.0	59.8
R_c [cm]	0.79	0.99	1.48	2.47	3.29

Table 4.2: A table of the theoretical values for the energies of the experiment.

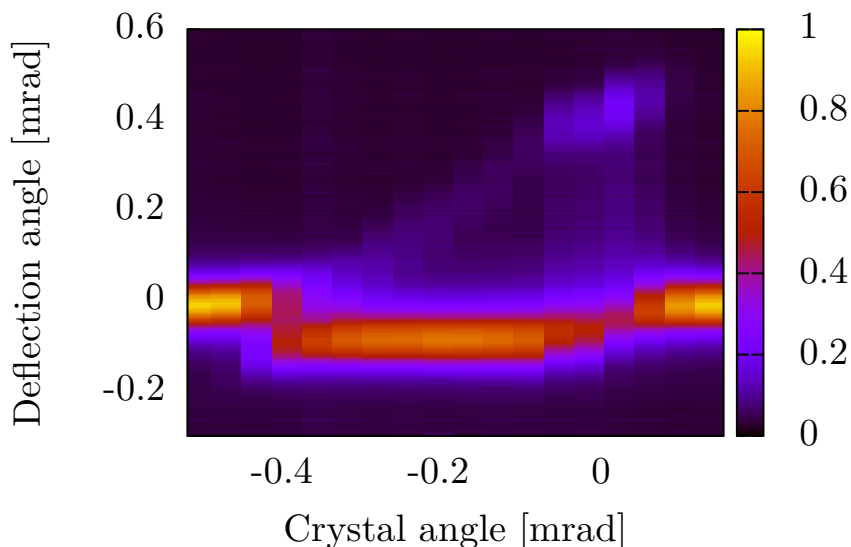


Figure 4.1.6: The probability density relative to the maximum probability density of the deflected particles as a function of the crystal angle for the case of 6.3 GeV electrons.

crystallographic orientation chosen to produce quasi-mosaic bending of the (111) plane [46]. Its thickness was measured interferometrically to be $60 \pm 1 \mu\text{m}$. The (111) plane has a bending radius of 0.15 m giving a total bending angle of the crystal of $\theta_b = 402 \pm 9 \mu\text{rad}$ in the horizontal direction. The crystal was mounted in a scattering chamber in the End Station Test Beam A (ESTB A) at SLAC, see figure 4.1.2. A rotational

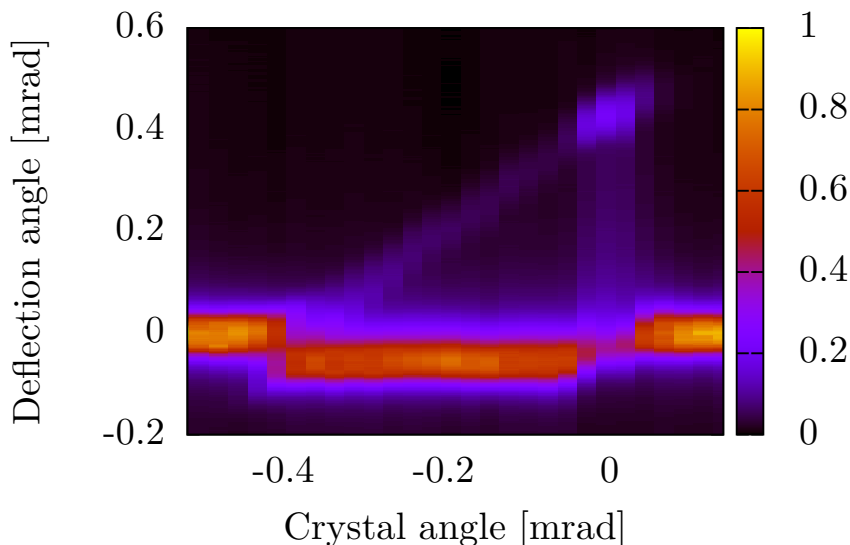


Figure 4.2.1: The probability density relative to the maximum probability density of the deflected particles as a function of the crystal angle for the case of 10.5 GeV electrons.

stage allows rotation of the crystal with step sizes of approximately 5 μrad . A translational stage moves the crystal to its optimal position. The rotation angle of the crystal is determined by reflecting a laser beam off a flat mirror mounted on the side of the crystal holder. The reflected laser beam hits a screen approximately 1m from the mirror. When the crystal is rotated, the laser beam on the screen provides a read-out of the rotation angle of the crystal with a resolution better than 5 μrad . A Cerium doped Yttrium Aluminum Garnet (YAG for short) screen of 500 μm thickness with a CCD camera 13 m down stream of the crystal provides the means of data acquisition in this experiment. Saturation of the YAG screen is negligible at the bunch charge 10^8 particles per bunch that was provided for this experiment [47]. The beam divergence was measured to be less than 10 μrad rms by the wire scanners. The spot-size was less than 150 μm and the momentum spread reduced to about 0.15%.

4.3 Data analysis and results

The experimental measurements were performed by rotating the crystal in small angular steps and recording an image of the circular YAG screen. The camera was mounted at an angle with respect to the screen which distorted the image. An ellipse was fitted along the edge of the screen, for this was known to be circular. This allows one to revert this image distortion due to the positioning of the camera. A region of the screen is chosen such that the edge of the screen is avoided. The crystal deflects particles in the horizontal plane and we sum the intensity in the vertical plane and normalize the probability distribution as seen in e.g. figure 4.3.1. For each crystal angle several images were taken. Images with low or high (camera saturated) light intensities were ignored. Plotting the distribution along the y-axis with the crystal angle along the x-axis one obtains the so called 'triangle plots', (figure 4.1.3 to figure 4.2.1 represent the raw data). A crystal angle of 0 was chosen to be the orientation of closest direct entry of the beam into the channel as could be experimentally realized. This orientation, along with the halfway of the full bending of $\theta_b = 402 \mu\text{rad}$, (roughly $\frac{\theta_b}{2}$) termed the volume reflection orientation, will be investigated in detail. In the triangle plots of figure 4.1.3 to figure 4.2.1 some features should be noted. When the beam has a tangent along the curved crystal plane, volume reflection takes place giving rise to the downshifted horizontal island in these figures. The skewed line shows the particles not reflected at the tangent between the bent plane and beam, but captured and following the curvature until the end of the crystal. The small island at the end of the skewed line arises due to particles entering directly into the crystal channel acceptance at the crystal face, and which travel along the whole curvature of the crystal plane. The vertical line connecting this island and the lower horizontal island are the particles that were captured at the crystal face, but then dechannel along the way.

In figure 4.3.1 and figure 4.3.2 the probability density of the deflected particles is plotted for the two different cases described above. In figure 4.3.1, some general tendencies can be identified. The width of the large leftmost peak, becomes narrower as does the channeled peak due to the decreasing critical angle. In figure 4.3.2 the large leftmost peak due to volume reflection moves closer to the undeflected position and the width decreases as energy increases. To extract quantitative information from these distribu-

tions I consider a fitting procedure consisting of two Gaussian probability distributions for the two peaks and a function for the dechanneled particles in between to be specified. For $i = 1, 2$ I have two Gaussian distributions

$$\frac{dP}{d\theta}(\theta) = \frac{P_i}{\sigma_i\sqrt{2\pi}} e^{-\frac{(\theta-\mu_i)^2}{2\sigma_i^2}}, \quad (4.3.1)$$

where P_i is the fraction of particles in this peak, σ_i the standard deviation of the distribution and μ_i the center. The undeflected/volume reflected particles are denoted by $i = 1$ and either the channeled or volume captured particles are denoted by $i = 2$. The probability to dechannel per angle in the exponential decay model of equation (2.1.12) is $\frac{dP}{d\theta} = e^{-\frac{\theta}{\theta_d}}/\theta_d$. Therefore the probability distribution of the dechanneled particles becomes

$$\frac{dP_d}{d\theta}(\theta) = \int_{\mu_1}^{\mu_2} \frac{1 - P_1}{\sigma_2\sqrt{2\pi}} e^{-\frac{(\theta-\theta')^2}{2\sigma_2^2}} \frac{1}{\theta_d} e^{-\frac{\theta'}{\theta_d}} d\theta', \quad (4.3.2)$$

where $\theta_d = \frac{L_d}{L}\theta_b$. This formula can be understood as follows: The probability to find a particle at an angle θ is the probability weighted sum over the possible ways this can happen. A fraction of the particles dechanneling at angle θ' can end up at the angle θ due to the distribution of particles in the channel. The above can also be rewritten as

$$\frac{dP_d}{d\theta}(\theta) = \frac{1 - P_1}{2\theta_d} e^{\frac{\sigma_2^2}{2\theta_d^2} + \frac{\mu_1}{\theta_d} - \frac{\theta}{\theta_d}} \times \left(\operatorname{erf}\left(\frac{\mu_2 - \Delta\theta}{\sqrt{2}\sigma_2}\right) - \operatorname{erf}\left(\frac{\mu_1 - \Delta\theta}{\sqrt{2}\sigma_2}\right) \right), \quad (4.3.3)$$

where $\Delta\theta = \theta - \frac{\sigma_2^2}{\theta_d}$. The exponential dechanneling model means that P_2 is given by $P_2 = (1 - P_1)e^{-\frac{L}{L_d}}$. This model therefore contains six free parameters: $P_1, \sigma_1, \mu_1, \sigma_2, \mu_2, L_d$. It turns out that the non-Gaussian tail of the undeflected peak has a large influence on the fit between the two peak functions which is important when trying to determine the dechanneling length. A sum of two Gaussians fits the peak in the 'amorphous' orientation very well which I write in the form

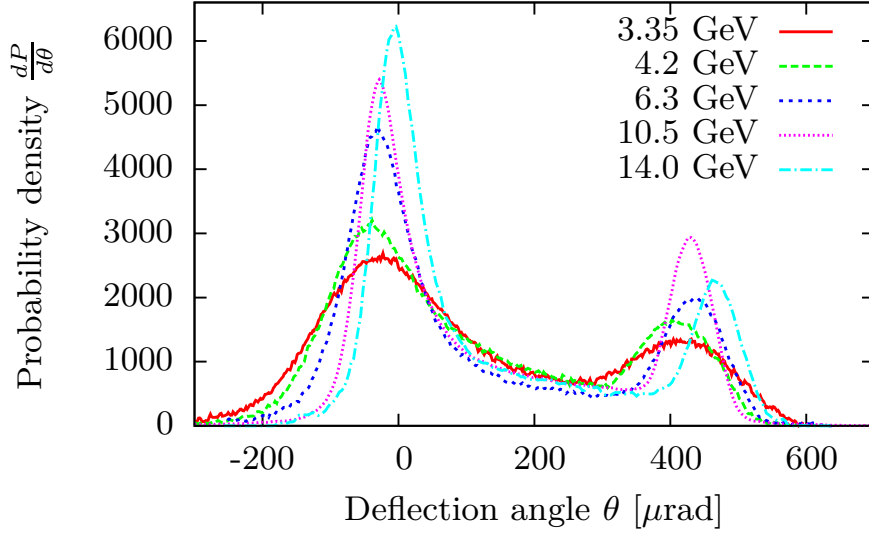


Figure 4.3.1: The probability density of the deflected particles when the crystal is in the channeling orientation for the different energies in the experiment.

E [GeV]	3.35	4.2	6.3	10.5	14.0
A	0.571	0.776	0.872	0.696	0.77
r	1.52	2.19	2.04	2.27	3.10

Table 4.3: A table of the fitting parameters used to describe the distribution in the 'amorphous' orientation.

$$\frac{dP}{d\theta}(\theta) = P_1 \left(\frac{A}{\sigma_1 \sqrt{2\pi}} e^{-\frac{(\theta-\mu_1)^2}{2\sigma_1^2}} + \frac{1-A}{r\sigma_1 \sqrt{2\pi}} e^{-\frac{(\theta-\mu_1)^2}{2r^2\sigma_1^2}} \right), \quad (4.3.4)$$

where the standard deviation of the second Gaussian is $r\sigma_1$. The values of A and r were then found by performing a fit in the 'amorphous' orientation and the values obtained are shown in table 4.3.

In figure 4.3.3 and figure 4.3.4 the data in the 'channeling' orientation for

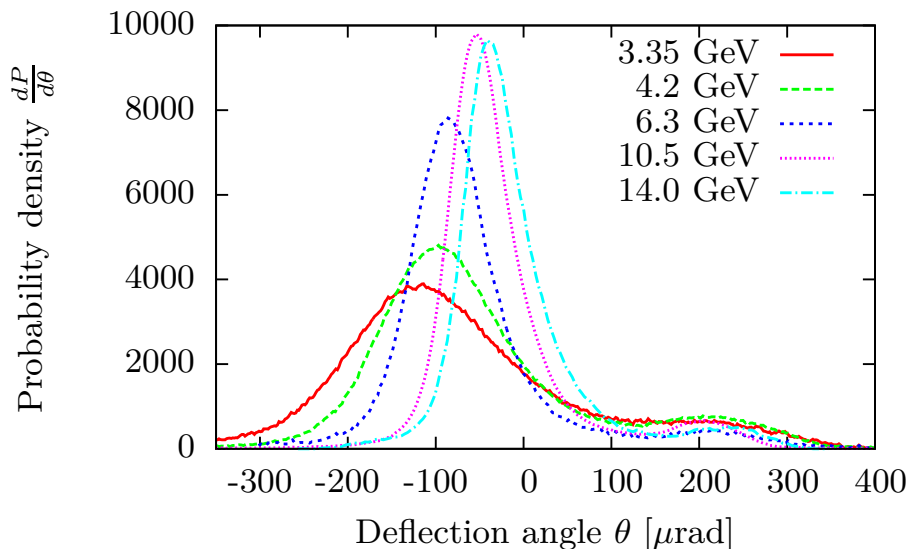


Figure 4.3.2: The probability density of the deflected particles when the crystal is at half of the full bending angle. The large leftmost peaks are the volume reflected portions and the small rightmost peaks are the volume captured particles.

the lowest and a high energy are fitted according to the model described here. The results are shown in table 4.4. The errors given here are only statistical.

Similarly in figure 4.3.5 and figure 4.3.6, the same fit is applied to the case where the crystal is roughly at the angle of $\frac{\theta_b}{2}$ and the results are shown in table 4.5.

It is important to note that the model presented here is different from the one used for the analysis of the 3.35 and 6.3 GeV data seen in [9]. Therefore different numbers for e.g. the dechanneling length are obtained. In particular the approach using a double Gaussian for the amorphous/VR peak and that I in the model used here have one less fitting parameter, are differences. This model is thus more constrained. In [9] it was noted that the dechanneling length could be determined in two ways. One based on the shape of the distribution (e.g. figure 4.3.4) between the two peaks, and

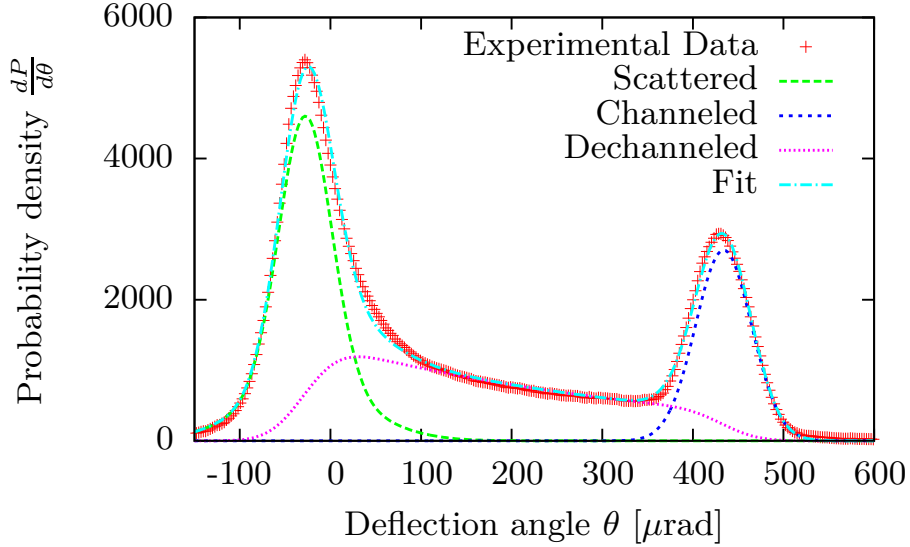


Figure 4.3.3: A fit to the 10.5GeV experimental data in the channeling orientation.

E [GeV]	3.35	4.2	6.3	10.5	14.0
L_d [μm]	55.4 ± 1.8	45.2 ± 1.2	65.3 ± 1.9	57.5 ± 1.2	55.8 ± 1.2
P_1 [%]	43 ± 1.3	33 ± 1.5	50 ± 0.8	41 ± 0.7	49 ± 0.7
μ_1 [μrad]	-49.9 ± 2.3	-62.4 ± 2.3	-33.8 ± 1.0	-28.4 ± 0.8	0.29 ± 0.5
μ_2 [μrad]	428.8 ± 1.45	419.8 ± 1.5	439.2 ± 1.2	433.9 ± 0.8	470.3 ± 0.9
σ_1 [μrad]	76.1 ± 0.92	53.9 ± 1.1	49.2 ± 0.8	29.0 ± 0.5	29.0 ± 0.5
σ_2 [μrad]	67.0 ± 1.1	48.5 ± 1.0	42.6 ± 0.9	30.9 ± 0.6	34.1 ± 0.7

Table 4.4: A table of the fitting parameters for the crystal in 'channeling' orientation using the described model.

another based on the relative sizes of the two peaks. In [9] this gave rise to two different dechanneling lengths. The model used here is constrained such that this is not a possibility. Using one less fitting parameter it is expected that the fit could be worse. However, generally the fits are good, but worse at higher energies than at low energies (the 10.5 and 14GeV

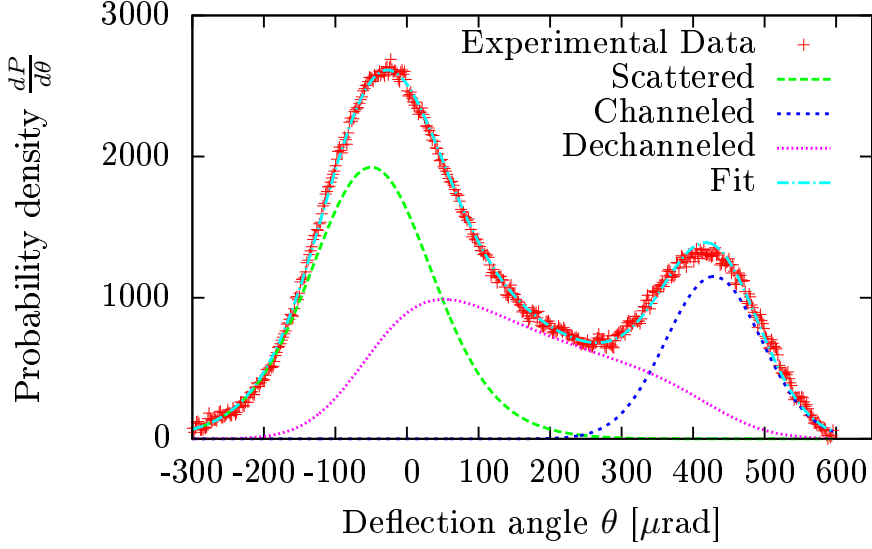


Figure 4.3.4: A fit to the 3.5GeV experimental data in the channeling orientation.

E [GeV]	3.35	4.2	6.3	10.5	14.0
L_d [μm]	35.5 ± 3.9	45.6 ± 3.1	36.4 ± 3.8	40.9 ± 3.4	25.6 ± 3.7
P_1 [%]	67 ± 3.8	73 ± 1.3	84 ± 1.1	84 ± 0.9	80.7 ± 2.3
μ_1 [μrad]	-128.8 ± 4.1	-100.7 ± 1.2	-84.0 ± 0.9	-50.3 ± 0.6	-35.6 ± 1.4
μ_2 [μrad]	242.1 ± 5.3	239.9 ± 3.6	243.3 ± 8.1	219.8 ± 3.7	258.0 ± 9.5
σ_1 [μrad]	73.5 ± 1.2	58.1 ± 0.7	42.8 ± 0.7	28.5 ± 0.4	28.2 ± 0.9
σ_2 [μrad]	57.9 ± 3.0	55.8 ± 2.3	55.0 ± 5.6	32.9 ± 2.6	27.0 ± 6.1

Table 4.5: A table of the fitting parameters for the crystal in 'volume capture' orientation using the described model.

cases are about equally good). Only in the case of the VR orientation at 14GeV is the fit worse than the example shown by figure 4.3.5 but this also to a considerable degree.

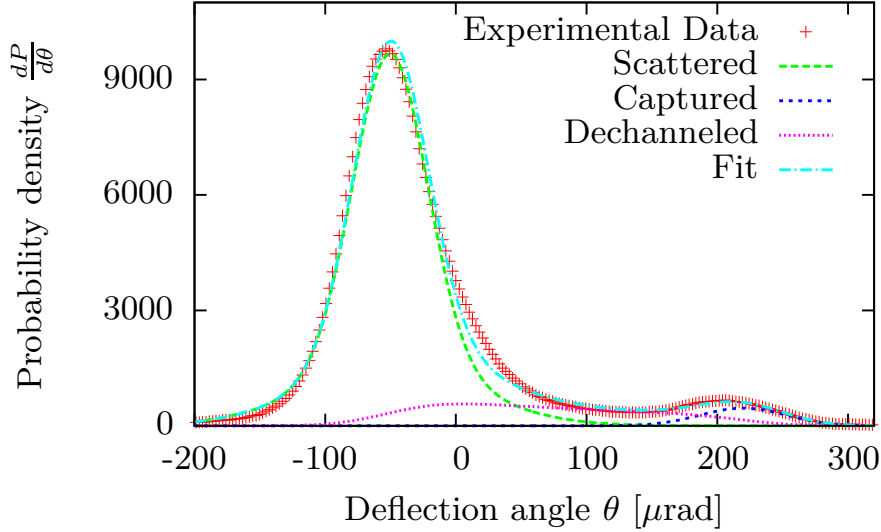


Figure 4.3.5: A fit to the 10.5 GeV experimental data at half the crystal bending angle.

4.3.1 Multiple scattering of channeled particles parallel to the plane

In figure 4.3.7 we have plotted the r.m.s. standard deviation, σ_{\parallel} , of the Gaussian function fitted to the distribution of channeled particles in the direction parallel to the plane i.e. in the 'free' direction in the continuum potential approximation. It is therefore expected that multiple scattering determines the width in this case. The multiple scattering width scales as $1/E$ and performing a fit I obtain the best fit to be given by

$$\sigma_{\text{MS}} = \frac{520 \mu\text{rad} \times \text{GeV}}{E}. \quad (4.3.5)$$

The usual formula for multiple scattering equation (2.1.10) would predict the factor to be $302 \mu\text{rad} \times \text{GeV}$, thus an increased scattering is observed. This is likely due to negative particles crossing the plane during channeling oscillations and thus more often encounter hard scattering with the nuclei [48], [18], [49]. We are not aware of a derived theoretical formula

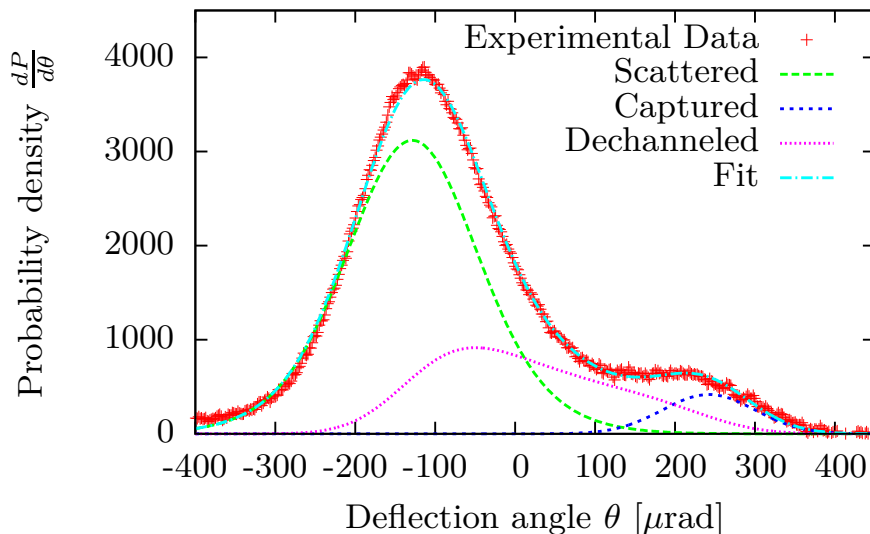


Figure 4.3.6: A fit to the 3.5 GeV experimental data at half the crystal bending angle.

which predicts the size of this effect and it seems difficult to do so since channeling is usually described by the continuum potential which neglects incoherent scattering. This effect is an interplay between the incoherent scattering and the channeling motion which are usually described separately. Simulation of the effect should, however, be possible.

4.3.2 Angular distribution of channeled particle orthogonal to the plane

In figure 4.3.8 we have plotted the r.m.s. standard deviations σ_2 from table 4.4 and a fit to a power function that yields

$$\sigma_2 = 117\mu\text{rad} \times E[\text{GeV}]^{-0.53}. \quad (4.3.6)$$

Since the critical angle scales as $1/\sqrt{E}$ we have also performed such a fit to obtain

$$\sigma_2 = 111\mu\text{rad} \times E[\text{GeV}]^{-0.5}. \quad (4.3.7)$$

The scatter of the points around these curves indicates a systematic error which is likely due to the limited resolution of the rotational stage, i.e. it is not guaranteed that the crystal is at exactly the same angle to the beam for each energy.

4.3.3 Deflection angle of volume reflected particles

In figure 4.3.9 we have plotted the deflection angle in volume capture orientation ($-\mu_1$ from table 4.5) versus the beam energy and fit the data to two different functions. Fitting the data to a power function we obtain

$$|\mu_1| = 338\mu\text{rad} \times E[\text{GeV}]^{-0.81}. \quad (4.3.8)$$

Again, we would expect there to be a $1/\sqrt{E}$ scaling. With such a fit we obtain

$$|\mu_1| = 207\mu\text{rad} \times E[\text{GeV}]^{-0.5}. \quad (4.3.9)$$

4.3.4 Efficiency of volume capture

In the case of 'volume reflection orientation', P_1 gives the fraction of reflected particles and the rest will have been captured, such that $1 - P_1$ is the fraction of particles captured. From section §4.1, we expect the volume reflection to scale with energy as $E^{-3/2}$ [41]. We have therefore performed such a fit along with a fit to a power function, see figure 4.3.10, and obtained

$$\varepsilon_{\text{VR}} = 2.3 \times E[\text{GeV}]^{-1.5}, \quad (4.3.10)$$

and

$$\varepsilon_{\text{VR}} = 0.57 \times E[\text{GeV}]^{-0.52}. \quad (4.3.11)$$

It is seen that the fitted power function is close to a $1/\sqrt{E}$ scaling. If one assumes an energy independent dechanneling length L_D as is indicated experimentally, one would also expect the volume capture efficiency to

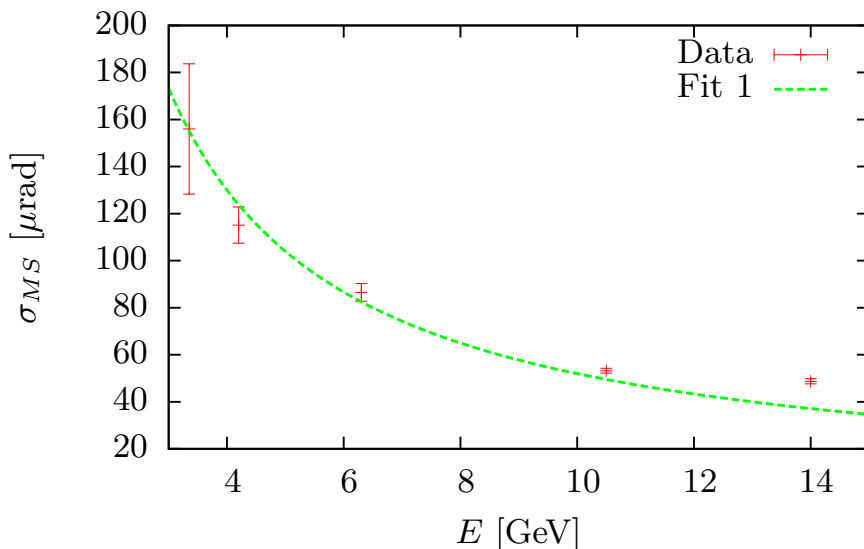


Figure 4.3.7: The width of the channeling peak in the direction parallel to the plane is fitted to obtain equation (4.3.5).

instead scale as $1/\sqrt{E}$. Although this observation may be surprising, the data set thus consistently shows a dechanneling length that is largely independent on energy.

4.3.5 Discussion of the dechanneling length and surface transmission

In figure 4.3.11, supported by the fit in figure 4.3.10, as discussed, it is evident that the dechanneling lengths obtained from the experiment has a dependence on energy which is not directly proportional as the simple formula of equation (2.1.11) prescribes. The formula which has been corrected for the crystal bending equation (4.1.5) however, has a qualitative agreement. Based on this we performed a fit where we allowed for a constant scaling front factor, and a variable scale factor on R_c , determined by the fit. This yields

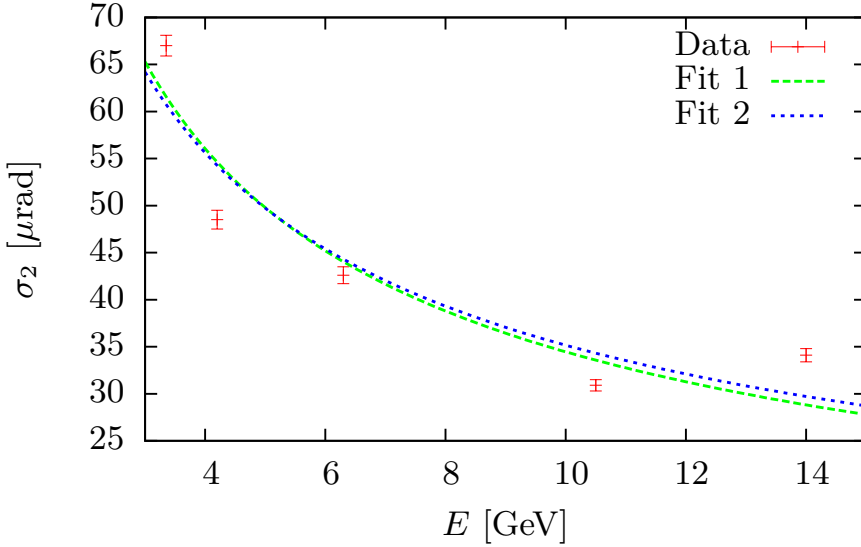


Figure 4.3.8: The width of the channeling peak in the direction orthogonal to the plane is fitted with a power function (Fit 1), see equation (4.3.6) and to a function of the type a/\sqrt{E} (Fit 2), see equation (4.3.7).

$$L_D = 15.3 \frac{\mu\text{m}}{\text{GeV}} \cdot E \left(1 - 1.76 \frac{2R_c}{R} \right). \quad (4.3.12)$$

In equation (4.1.5) the front factor is $20.3 \frac{\mu\text{m}}{\text{GeV}}$. Keeping in mind the simple derivation leading to equation (2.1.11), an accuracy higher than a factor of 2 cannot be expected, but it should give the correct scaling and order of magnitude. Equation (4.3.12) should thus be usable as a predictive formula for other energies and bending radii of the Si (111) plane.

The measured and calculated (from equation (4.1.7)) values of the surface transmission are in good agreement and are plotted in figure 4.3.12. In this case the fluctuation of the data points around this curve we also attribute to the uncertainty on the beam entry angle.

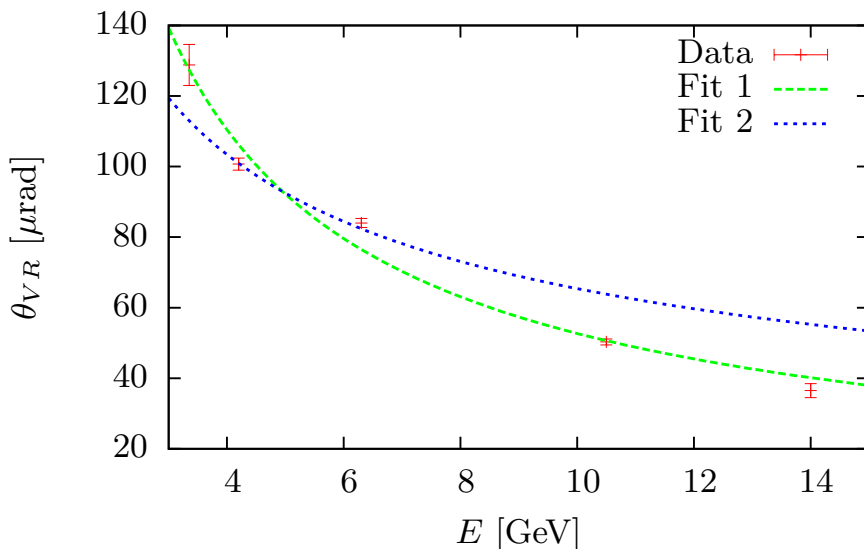


Figure 4.3.9: The angle of volume reflection is fitted with a power function (Fit 1) and to a function of the type a/\sqrt{E} (Fit 2).

4.4 Conclusion

We have shown that a fitting procedure based on 1) a simple exponential decay model of channeled particles and 2) that these particles are distributed according to a Gaussian distribution within the channel, fit the data with good agreement. Based on the parameters of the fitting functions we have extracted important parameters describing the channeling process, such as the dechanneling length, the angle of volume reflection, the surface transmission and the widths of the distribution of channeled particles parallel and orthogonal to the plane. The scattering parallel to the plane fits well with the usual functional dependence of multiple scattering on energy but is larger than amorphous/random by a factor of 1.7. For the distribution of channeled particles, the mean of the angle of volume reflection and the efficiency of volume capture, were fit to power functions with a free exponent and to a exponent fixed by that predicted by 'simple' theory. In these cases, a significant deviation is seen in the

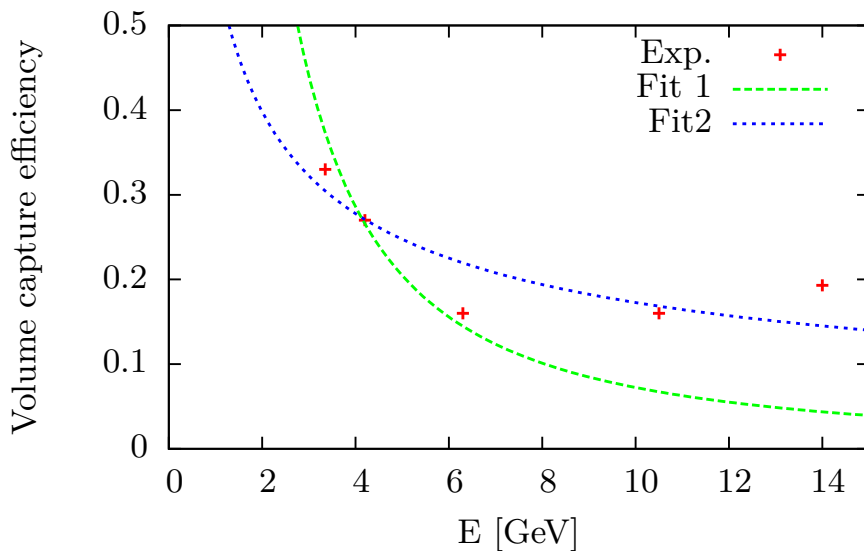


Figure 4.3.10: The volume capture efficiency as given by $1 - P_1$ from table 4.5. 'Fit 1' is a fit to a function of the type $aE^{-3/2}$ and 'Fit 2' is a fit to a power function (aE^b).

exponent which indicates that the 'simple' theory may be too simple to describe the results of this experiment. The 'simple' formula for surface transmission, however, works out well. The dechanneling lengths observed in these experiments are significantly shorter than predicted by the 'simple' theory and the dechanneling length in 'VR orientation' is seen to be consistently smaller than in 'channeling orientation' indicating preferential population of high-lying transverse energy states in VR mode.

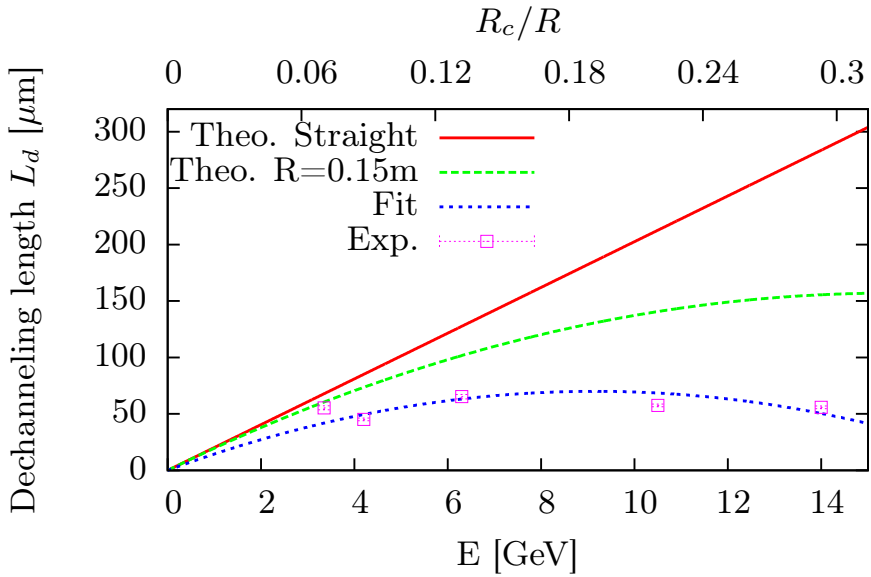


Figure 4.3.11: A plot of the 'simple' dechanneling formulas of equation (2.1.11), equation (4.1.5), equation (4.3.12) and of the experimental values.

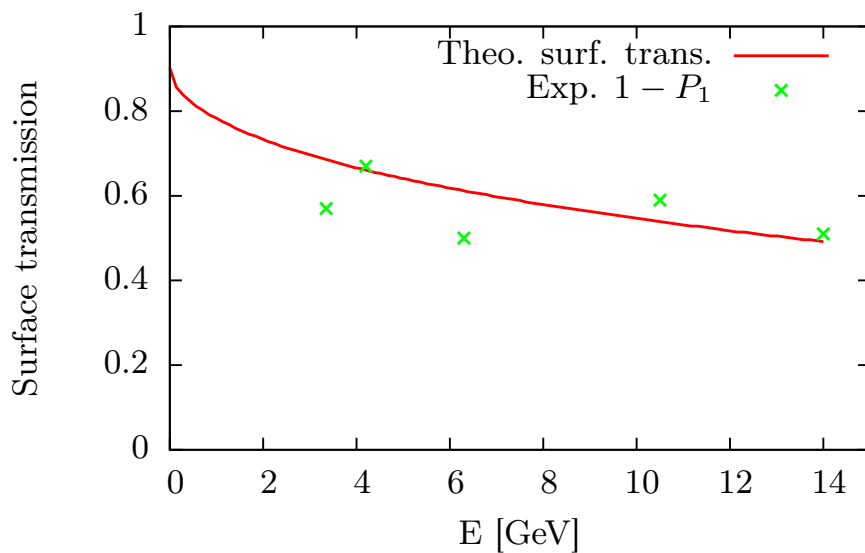


Figure 4.3.12: The experimental values of the surface transmission given by $1 - P_1$ are compared with the model of equation (4.1.7).

Chapter 5

The Heisenberg-Euler-Schwinger effective Lagrangian and vacuum birefringence

This chapter is to a large extent identical to the paper[2]. In this chapter I leave out some of the calculational details for which I refer to [2], and focus on the interesting physics and the results obtained. We now, momentarily, leave the topic of channeling and radiation emission behind. We will here look at effects related to what is called polarization of the vacuum. A material containing dipole moments, is said to have a polarization and while the material is electrically neutral, an external field affects these dipoles which in turn affect the field. In a popular picture of QED the vacuum is seen to be populated by electron/positron pairs whizzing in and out of existence justified by the uncertainty principle. When speaking of vacuum polarization, it is this 'material' of the vacuum with virtual pairs which can then be polarized by an external field. As we will see in this chapter, the precise calculation yields a result where, to leading order in the external fields, the vacuum will behave exactly like a polarizable medium. This polarization of the vacuum is an effect which has several consequences. One is the running of the QED coupling constant α which is an experimentally well-established fact seen in the

processes investigated in high-energy particle accelerators, but also in the atomic spectra - an effect most noticeable in high-Z or muonic atoms. Another effect of vacuum polarization is the process of elastic scattering of light by an external field, the so-called Delbrück scattering (see [50] for instance). Another prediction is the decay of this vacuum, meaning an electric field can induce spontaneous production of real electron/positrons pairs, reducing the field strength [51][52][53]. In this chapter we argue that it should be possible to directly measure the change of polarization of highly energetic radiation as it passes through a long, high-field dipole magnet, for instance an LHC dipole magnet. This is the so-called vacuum birefringence [54][55][56][57][2]. There are several experiments currently being conducted that attempt to measure the vacuum birefringence by using optical, or near-optical photons. See, for instance, [58], [59] for the latest status on the PVLAS and BMV experiments. Other suggested experiments to measure this effect include using a high-powered free electron laser to provide the strong background field, to be probed by another weak laser field. See for instance [56].

5.1 The Heisenberg-Euler-Schwinger effective Lagrangian

The Heisenberg-Euler-Schwinger effective Lagrangian describes the electromagnetic fields while keeping only the QED corrections to lowest order in the fine structure constant, but including any (even) number of photons. The result was first derived by W. Heisenberg and H. Euler. [60]. We use the expression of J. Schwinger [51]

$$\mathcal{L} = \mathcal{F} - \frac{1}{8\pi^2} \int_0^\infty ds s^{-3} \exp(-m^2 s) \left[(es)^2 \mathcal{G} \frac{\text{Re} \cosh esX}{\text{Im} \cosh esX} - 1 - \frac{2}{3} (es)^2 \mathcal{F} \right], \quad (5.1.1)$$

with $\mathcal{F} = \frac{1}{2}(\mathbf{E}^2 - \mathbf{B}^2)$, $\mathcal{G} = \mathbf{E} \cdot \mathbf{B}$, $X = \sqrt{2(\mathcal{F} + i\mathcal{G})}$ and m the electron mass. Of interest to us is the asymptotic expansion of this Lagrangian:

$$\mathcal{L} = \mathcal{F} + \frac{\alpha^2}{90\pi m^4} [4\mathcal{F}^2 + 7\mathcal{G}^2] + \dots, \quad (5.1.2)$$

If one considers the situation with two fields, a strong static “background” field, and a weak perturbing radiation field, one can from the above Lagrangian derive the field equations for the radiation field. To the leading order in the “background” fields this manifests itself, as if the radiation was propagating in a dielectric medium, with the permittivity and permeability depending on the strong background fields

$$\epsilon_{ik} = \delta_{ik} + \frac{\alpha^2}{45\pi m^4} \left[2(\mathbf{E}^2 - \mathbf{B}^2)\delta_{ik} + 7B_i B_k \right], \quad (5.1.3)$$

$$\mu_{ik} = \delta_{ik} + \frac{\alpha^2}{45\pi m^4} \left[2(\mathbf{B}^2 - \mathbf{E}^2)\delta_{ik} + 7E_i E_k \right], \quad (5.1.4)$$

as seen in [21] or [61] (there is a missing factor of π in the denominator in [61]). The field quantities in these dielectric tensors are the ones from the strong background field. Solutions are readily obtained which yield a difference in the refractive index, depending on whether the polarization of the radiation is in the same direction as the magnetic field, or perpendicular to it. The results are

$$n_{\perp} = 1 + \frac{7\alpha}{90\pi} \frac{\mathbf{B}^2}{B_c^2}, \quad (5.1.5)$$

$$n_{\parallel} = 1 + \frac{2\alpha}{45\pi} \frac{\mathbf{B}^2}{B_c^2}, \quad (5.1.6)$$

where $B_c = \frac{m^2}{e}$ is the Schwinger critical field ($4.4 \cdot 10^9 \text{T}$). The first to analyze the QED vacuum birefringence as a consequence of the effective Lagrangian of equation (5.1.1), although unpublished, was Toll in his thesis of 1951 [62]. He derived not just equation (5.1.5) and equation (5.1.6), but the frequency dependence in the low-field limit $|\mathbf{B}| \ll B_c$. See for instance [63] for a modern calculation that confirms his findings. Formulas equation (5.1.5) and equation (5.1.6) are the low frequency limit of the general result, valid as long as [61],[63] $\omega \ll m \frac{B_c}{B}$, where B is the strength of the static magnetic background field. We will be well below this limit. This difference of refractive index induces a phase shift of the radiation between the two polarization directions given by:

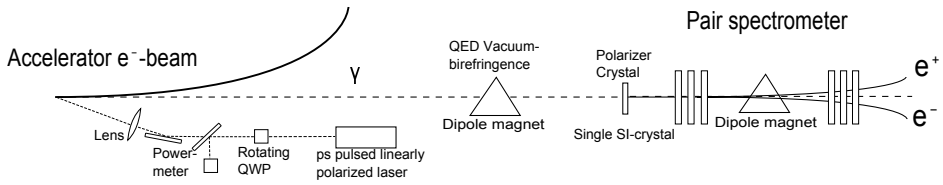


Figure 5.1.1: Experimental setup. Linearly polarized laser light passes through a rotating quarter wave-plate, the power is measured and then undergoes Compton back scattering. The scattered photons pass through the high field dipole magnet, and the resulting radiation is analyzed using a single Si-crystal and a pair spectrometer.

$$\Delta = \omega L_B \frac{3\alpha}{90\pi} \frac{\mathbf{B}^2}{B_c^2}, \quad (5.1.7)$$

With L_B being the length of the dipole magnet and ω the photon energy.

5.2 The proposed experiment

The experimental setup proposed to measure this effect can be seen in figure 5.1.1. To calculate the resulting pair creation rate at the tracking detectors we use the formalism of Müller calculus [64] which facilitates the calculation of the polarization and intensity of radiation through an optical system. The radiation is described by a Stokes vector and the optical elements with a Müller matrix. The Stokes vector has the form $I \begin{pmatrix} 1, & \xi_1, & \xi_2, & \xi_3 \end{pmatrix}^T$ where I is the intensity. The numbers ξ_i are between -1 and +1 and are the degree of linear polarization in the directions 0° , 45° with respect to some arbitrary, predetermined axis, and the last is the degree of circular polarization. The final Stokes vector is determined by acting on this initial Stokes vector by the Müller matrix of each component of the setup. In our setup, I will have 4 Müller matrices. One for a rotating quarter-wave-plate, one for the Compton back scattering process, one for the QED process and one for the crystal polarizer.

The laser light is linearly polarized and the initial Stokes vector is then $S_i = I(1, 1, 0, 0)^T$. To overcome drifting in the parameters of the setup, we

wish to make the state of polarization time dependent, with a short period relative to the period of such drifting. This is achieved by rotating the quarter-wave-plate by an angle $\theta = \omega_0 t$, where ω_0 is a constant angular frequency of rotation. For the details of this calculation, see [2]. When setting the degree of circular polarization of the electron beam to zero $\lambda = 0$, the final result for the pair production rate is given by

$$\begin{aligned} \frac{d^3 N_{\text{pairs}}}{dt dz dy} = \mathcal{L}_{e\gamma} \frac{d\sigma_c^{np}}{dy} \frac{I_i}{2\omega_i} & \left[\left(1 + \frac{2r^2}{f_1(y)} \cos^2 \theta - \frac{f_3(y)}{f_1(y)} \Delta \sin \theta \right) \frac{1 - q(y)}{\sigma_{\perp}(y)} \frac{d\sigma_{\perp}(y)}{dz} + \right. \\ & \left. + \left(1 - \frac{2r^2}{f_1(y)} \cos^2 \theta + \frac{f_3(y)}{f_1(y)} \Delta \sin \theta \right) \frac{1 - r(y)}{\sigma_{\parallel}(y)} \frac{d\sigma_{\parallel}(y)}{dz} \right] \quad (5.2.1) \end{aligned}$$

with $\sigma_{\perp}(y)$, $\sigma_{\parallel}(y)$ being the total number of pairs created per distance, which depend on the photon energy parametrized by $y = \frac{\omega_f}{E}$. Note that $\sigma_{\perp}(y)$, $\sigma_{\parallel}(y)$ are not cross-sections in the traditional sense, but the cross-section multiplied by the number density of the target material (σn) - they are the inverse of the mean free path. To calculate the pair production cross-sections we use the theory of coherent pair production as stated by Ter-Mikaelian in [27]. The differential pair production cross section depends on the asymmetry between the energies of the two particles: $z = \frac{\varepsilon_-}{yE}$, with ε_- being the energy of the pair-produced electron. A typical plot of $\frac{d\sigma_{\perp}}{dz}$ and $\frac{d\sigma_{\parallel}}{dz}$, for 31GeV incoming photons, can be seen in figure 5.2.1. The angles were chosen to optimize the asymmetry $\frac{d\sigma_{\parallel} - d\sigma_{\perp}}{d\sigma_{\parallel} + d\sigma_{\perp}}$ over the interval $0.3 < z < 0.7$ at a photon energy of 31GeV. Additionally I have $q(y) = e^{-\sigma_{\perp}(y) \cdot L}$, $r(y) = e^{-\sigma_{\parallel}(y) \cdot L}$, ω_f and ω_i are the photon energies after and before the Compton scattering process, E is the total electron energy and I have

$$f_1(y) = \frac{1}{1-y} + 1 - y - 4r(1-r), \quad (5.2.2)$$

$$f_2(y) = 2\lambda r x [1 + (1-y)(2r-1)^2], \quad (5.2.3)$$

$$f_3(y) = (1-2r) \left(\frac{1}{1-y} + 1 - y \right), \quad (5.2.4)$$

$$\mathcal{L}_{e\gamma} = 2N_e \iint \rho_{\gamma}(\vec{x}, t) \rho_e(\vec{x}, t) d^3 \vec{x} dt, \quad (5.2.5)$$

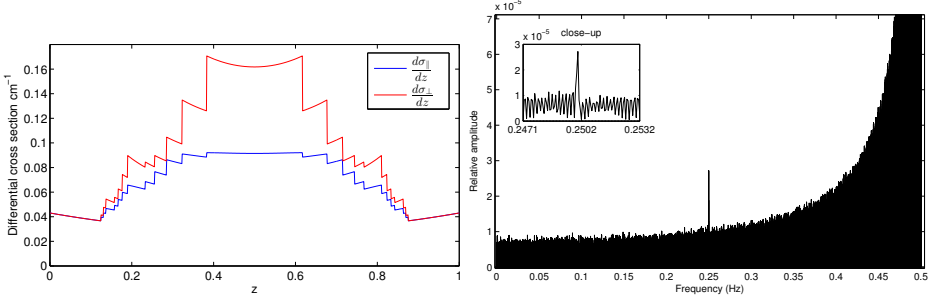


Figure 5.2.1: (Left) Differential pair production inverse mean free path for Si at 31GeV photon energy. $\theta = 1.4\text{mrad}$, $\alpha = 0.16$. Where θ is the angle between the momentum of the incoming particle \mathbf{p}_1 and the $\langle 110 \rangle$ axis, and α is the angle between the plane containing \mathbf{p}_1 and the $\langle 110 \rangle$ axis with the plane containing the axes $\langle 001 \rangle$ and $\langle 1\bar{1}0 \rangle$, see [27]. (Right) The Fourier transform of the relative signal subtracted its average. The wave plate rotation frequency was here chosen as 0.25Hz. At the end of the spectrum the large component at the double frequency can be seen. This is for a 3 hour measurement.

where $\rho_e(\vec{x}, t)$ and $\rho_\gamma(\vec{x}, t)$ are the unity normalized density profiles of the electron bunch and laser pulse, N_e is the number of electrons in the bunch, $r = \frac{y}{x(1-y)}$ with $x = \frac{4E\omega_i}{m^2}$, λ is the degree of circular polarization of the electron beam while

$$\frac{d\sigma_c^{np}}{dy} = \frac{2\pi\alpha^2}{xm^2} f_1(y), \quad (5.2.6)$$

$$\frac{d\sigma_1}{dy} = \frac{2\pi\alpha^2}{xm^2} rx(1-2r)(2-y), \quad (5.2.7)$$

as seen in [65].

If we now consider $\theta = \omega_0 t$ and integrate over the whole energy interval $0 < y < y_m$ and integrate over a suitably chosen interval for z we get a pair-production rate. The Fourier transform of this rate has components at frequencies $\omega = 0$, $\omega = \omega_0$ and $\omega = 2\omega_0$. The component at $\omega = \omega_0$ is the one of interest. It is only present when the magnet is turned on, and thus signifies the effect of vacuum birefringence. The component at

the double frequency is due to the fact that the polarization state of the Compton back scattered radiation depends on the initial polarization, and the polarizer crystal turns this into a difference in pair production rate.

In the setup seen in figure 5.1.1 the accelerator delivering the electron bunches is the LHeC, as an example. Any sufficiently energetic and luminous accelerator-laser setup can be considered [11]. We have used the parameters from the conceptual design report (CDR) of the LHeC. That means an electron energy of 60GeV, bunch spacing of 25ns, a bunch length of 6mm and a r.m.s. beam spot size of $\sigma_x = 30\mu\text{m}$, $\sigma_y = 16\mu\text{m}$. The pulsed laser is chosen with matching repetition rate of 40MHz and pulse duration of 20ps to overlap with the length of the bunch. There exists commercial systems of mode-locked lasers in this parameter range, with a wavelength of 1064nm and average power of up to 10W, that can be locked to an external RF-signal. The magnet considered is an LHC dipole magnet with a field strength of 9.5T and a length of 9.26m. I consider a silicon polarizer crystal with a length of 10% of the amorphous radiation length, about 1 cm, to avoid cascade processes. The tracking detectors to be used in the pair spectrometer must have a very high read-out rate. We propose using the tracking detectors used in the LHC ATLAS and CMS detectors or others with similar performance.

The expected relative variation of the signal at the frequency ω_0 is thus $2.5 \cdot 10^{-5}$ of the average pair production rate of $6.2 \cdot 10^8 \text{s}^{-1}$. A simulation of a 3 hour measurement, with simulated count uncertainty and relative measurement uncertainty of the intensity after the quarter wave-plate of $2 \cdot 10^{-5} \frac{1}{\sqrt{\text{Hz}}}$ can be seen in figure 5.2.1. Repeating the simulation gives us an uncertainty of the peak of interest of 3%, scaling as $\frac{1}{\sqrt{t}}$, where t is the measurement time.

5.3 Vacuum birefringence due to the interaction with an axion

We finally consider the influence of a possible axion, i.e. a different interaction given by

$$\mathcal{L} = \frac{1}{M} \phi \mathcal{G}, \quad (5.3.1)$$

as given in [66]. M is here a measure of the coupling constant given by $g = \frac{1}{M}$ and ϕ is the axion scalar field. This gives rise to a similar effect. The equations of motion are derived from equation (5.3.1) while keeping only linear terms in the radiation field \mathbf{A} and scalar field ϕ . This gives rise to a nontrivial dispersion relation. The phase difference between the two components of polarization of the radiation, parallel and orthogonal to the magnetic field are given by [66]

$$\varphi = \frac{\mathbf{B}^2 \omega^2}{M^2 m_a^4} \left[\frac{m_a^2 L}{2\omega} - \sin \frac{m_a^2 L}{2\omega} \right], \quad (5.3.2)$$

where m_a is the mass of the axion. The experiment will be designed to be able to detect a phase shift on the size of the one predicted by QED. If the result of the experiment is just the phase shift predicted by QED, we can thus rule out certain areas of the axion parameter space (mass and coupling constant). However by using equation (5.3.1) we see that this region is not within the ranges of what is predicted by grand unified theories such as DFSZ or KSVZ, which serve as the typical benchmark of such experiments. Here the coupling constant is given by [17]

$$g = \frac{\alpha}{2\pi} \left(\frac{E}{N} - \frac{2}{3} \frac{4+z}{1+z} \right) \frac{1+z}{\sqrt{z}} \frac{m_a}{m_\pi f_\pi}, \quad (5.3.3)$$

with $z = \frac{m_u}{m_d} \simeq 0.56$ being the ratio of the masses of the up and down quark, $\frac{E}{N}$ a model dependent ratio - $\frac{8}{3}$ for DFSZ and 0 for KSVZ, $m_\pi \approx 135\text{MeV}$ the pion mass and $f_\pi \approx 92\text{MeV}$ the decay constant of the pion. Should the experiment yield just the QED result, we see that we can exclude $g \geq 8 \cdot 10^{-4} \text{GeV}^{-1}$ for axion masses around $m_a = 60\text{eV}$, whereas the above model predicts $g \simeq 2.3 \cdot 10^{-8} \text{GeV}^{-1}$ for this mass. Of course, in the case of an anomalous result, one should carry out a careful analysis, considering the equations of motion resulting from the sum of lagrangians equation (5.1.2) and equation (5.3.1). The figures obtained here serve only to estimate the conditions where the existence of an axion would affect the result of the experiment.

In summary, we have shown that it is possible to measure the vacuum birefringence induced by a static magnetic field with good precision, within a reasonable time frame, using a similar experimental setup as the one proposed here. Any outcome of such an experiment would be interesting.

Either we would measure the QED vacuum birefringence for the first time or, in the case of an anomalous result, would point towards new physics, for instance the existence of the axion.

Chapter 6

An interference phenomenon in nonlinear Compton scattering

The content of this chapter is identical to that of my paper [4] except for the introduction and corrected according to the erratum [67]. In addition a small change in equation (6.1.3) such that we adhere to the units and conventions used in this thesis.

In this chapter we will return to the problem of radiation emission of relativistic electrons/positrons, but as opposed to chapter 3 we will now enter the quantum regime. In the area of strong field QED, nonlinear Compton scattering where a high energy electron collides nearly head-on with a laser wave, absorbing several laser photons to emit a single high energy photon is highly interesting. This is due to the fact that this effect is one of the only effects that have been put to an experimental test while many of the other effects predicted in this area of research have been difficult to put to any experimental test due to the incredible field strengths required. In [68] multiphoton Compton back scattering was thus observed for the first time. See e.g. [69] for a useful review in preparation of this experiment. It should be mentioned that several such similar effects had been observed previously in crystals such as radiation emission in a strong field [70] and pair production in the strong field [13, 71, 24]. There is interest in finding out how Compton scattering is modified in more advanced laser fields

than the monochromatic plane wave or constant field case and recently the cases of pulsed laser fields have been investigated [72][73] and the influence of finite laser beam-shape [74]. An investigation of the classical limit of nonlinear Compton scattering, nonlinear Thomson scattering can be seen in e.g. [75]. All of these mentioned papers of solutions in more advanced fields employ the method of the Volkov solution [20] which enables analytical solution when the 4-potential only depends on $\varphi = k^\mu x_\mu$, i.e. it can be written $A^\mu(\varphi)$. A strength of the semi-classical operator method, however, is that it allows for numerical solution in an arbitrary electromagnetic field, which is not easily the case using the traditional approach of the Volkov solution. Here I derive a formula suitable for numerical solution which is based on the semi-classical operator method [16], i.e. the formula derived in section §2.3. I show how this method is in agreement with the results obtained by using the analytical Volkov solutions in the plane wave case, and apply the procedure to investigate Compton scattering in the superposition of two strong plane wave fields revealing a, perhaps unexpected, interference effect. The problem of Compton scattering in a plane wave of arbitrary field strength has been solved [20] treating the strong field exactly using the Volkov states, and the appearance of an increased effective mass of the electron as predicted there has only recently been seen in terms of perturbation theory, although only in scalar QED [76], an effect however not yet experimentally verified (see [68] and also [77] for a recent general discussion of this mass shift). This chapter therefore goes through the essentials of the method and results using the Volkov solutions in section §6.1. I then discuss the semi-classical operator method and derive formulas based on this approach in section §6.2. In section §6.3 I discuss the results from numerical calculations based on these formulas, including the interference phenomenon. In section §6.4 I discuss some of the general consequences of these formulas, how numerical calculations are performed and how the mass shift arises in this approach.

6.1 Compton scattering as transitions between Volkov states

We start our discussion by reminding the reader of the results obtained using the traditional approach to nonlinear Compton scattering, see e.g.

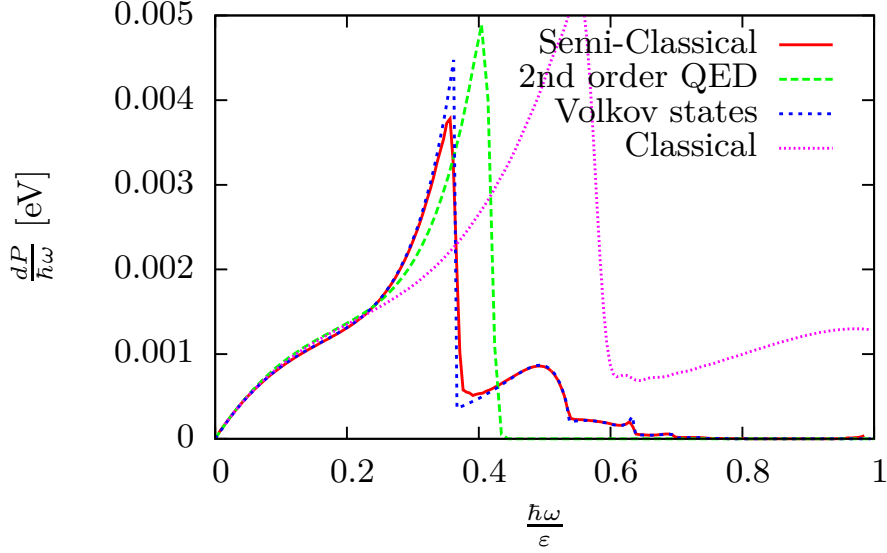


Figure 6.1.1: A comparison of the radiation power spectra of an electron moving in a plane wave characterized by $\omega = 2.35eV$, $\eta = 0.5$ and $\chi = 0.25$ obtained by using the semi-classical operator method, Compton scattering as prescribed by 2nd order perturbative QED (Klein-Nishina), nonlinear Compton scattering by using transitions between Volkov states and finally the classical result.

[20] or [78], [79] for more recent reviews of the subject. The Dirac equation with an electromagnetic interaction reads

$$(\not{\partial} + e\mathcal{A} - m)\psi = 0, \quad (6.1.1)$$

where A_μ is the vector potential of the electromagnetic field and m the electron mass. This is split up into a “strong” external field \mathcal{A}_{ext} , and an interaction field \mathcal{A}_{int} which governs the radiation emission, meaning

$$\mathcal{A} = \mathcal{A}_{\text{ext}} + \mathcal{A}_{\text{int}}. \quad (6.1.2)$$

The Dirac equation containing only the external field can then be solved analytically in the case where the external field depends only on the phase

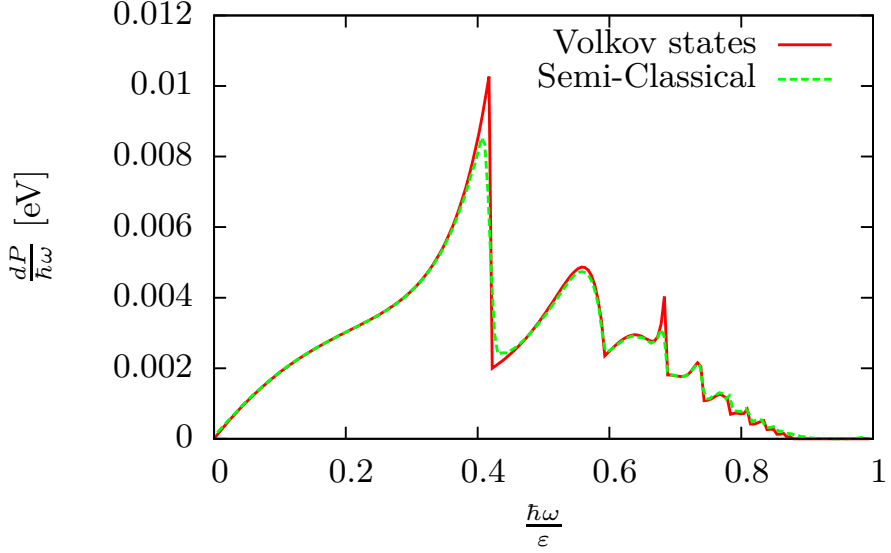


Figure 6.1.2: A figure similar to figure 6.1.1, but in a stronger field, characterized by the parameters $\omega = 2.35eV$, $\eta = 1.0$, $\chi = 1.0$.

$\varphi = k \cdot x$, with k being the 4-momentum of the photons of the external field, yielding the celebrated Volkov states

$$\begin{aligned} \psi(x) = & \left[1 - \frac{ek \cdot A_{\text{ext}}(\varphi)}{2k \cdot p} \right] u(p) \\ & \times \exp \left[i \int_0^\varphi \left(\frac{ep \cdot A_{\text{ext}}(\varphi')}{k \cdot p} + \frac{e^2 A_{\text{ext}}(\varphi')^2}{2k \cdot p} \right) d\varphi' - ip \cdot x \right], \end{aligned} \quad (6.1.3)$$

The interaction leading to emission of radiation is then treated to first order in perturbation theory which means we have a transition matrix element

$$M = ie \int \bar{\psi}_{p'r'} \not{\epsilon}'^* \psi_{pr} \frac{e^{-ik'x}}{\sqrt{2k'_0}} d^4x, \quad (6.1.4)$$

where k' is the 4-momentum of the emitted photon and e' its polarization. Looking at equation (6.1.1) it is seen that a transition takes place in the cases when $eA_\mu \ll m$ and $eA_\mu \gg m$ or, introducing the parameter

$$\eta = \frac{eE_{\text{rms}}}{m\omega}, \quad (6.1.5)$$

where E_{rms} is the r.m.s. value of the electric field of the plane wave given by A_μ and ω the angular frequency, this translates to $\eta \ll 1$ and $\eta \gg 1$. For $\eta \ll 1$ the interaction term is small compared to the rest, and the traditional perturbation theory expansion in the coupling e e.g. using Feynman diagrams is applicable. As η increases, higher orders of such diagrams become important, e.g. multiphoton absorption is seen. This parameter is, however, a classical quantity as it does not contain \hbar and describes the transition to relativistic motion of the electron in its 'average' rest-frame. It is encountered in for instance undulator radiation where η is in essence the undulator parameter. Using this formalism, the transition rate of photon emission in a strong linearly polarized plane wave is given by [20]

$$\frac{dW}{du}(x, \chi) = \sum_{s=1}^{\infty} \frac{dW_s}{du}, \quad (6.1.6)$$

where each term in the sum corresponds to absorption of s photons from the strong field, and are given by

$$\begin{aligned} \frac{dW_s}{du} = \frac{e^2 m^2 n}{2\pi q_0} \int_0^{2\pi} d\varphi \frac{1}{(1+u)^2} \\ \times \left\{ -A_0^2 + x^2 \left[1 + \frac{u^2}{2(1+u)} \right] (A_1^2 - A_0 A_2) \right\}, \quad (6.1.7) \end{aligned}$$

where $u = \frac{k \cdot k'}{k \cdot p'} \simeq \frac{\omega}{\varepsilon - \omega}$, ω being the energy of the emitted photon and ε the electron energy. The last equality holds in the limit where the two emitted particles are relativistic. $x = \sqrt{2}\eta$, $\frac{n}{q_0}$ is the invariant ratio of the density of the incoming electrons to their average quasi-energy $q_0 = \varepsilon + \frac{x^2 m^2}{8\varepsilon}$, $u_s = \frac{2s\chi}{x(1+\frac{x^2}{2})}$, is the largest value the variable u can take on, $\chi = \frac{e\sqrt{\langle (F_{\mu\nu} p^\nu)^2 \rangle}}{m^3}$, $A_n(s, \alpha, \beta) = \frac{1}{2\pi} \int_{-\pi}^{\pi} d\varphi \cos^n \varphi e^{f(\varphi)}$, $f(\varphi) =$

$i(\alpha \sin \varphi - \beta \sin 2\varphi - s\varphi)$, $\alpha = z \cos \varphi$, $z = \frac{x^2 \sqrt{1+x^2/2}}{\chi} \sqrt{u(u_s - u)}$, $\beta = \frac{x^3 u}{8\chi}$ and $F_{\mu\nu}$ is the electromagnetic field tensor. The invariant parameter χ describes the quantum non linearity of the process and does not emerge classically. Thus once χ deviates substantially from 0, quantum effects become apparent, and a classical treatment will fail. In [20] it is shown that for small η the terms in equation (6.1.6) become proportional to η^{2s} , meaning proportional to the intensity to the power of s that is, the process becomes nonlinear in the intensity of the strong field. In figure 6.1.1 and figure 6.1.2 plots of the power spectra ($dP = \omega dW$) are shown for different parameters, and compared with the results of other methods of calculation. From figure 6.1.1 the effects of for instance harmonic generation and electron recoil can be seen. The curve '2nd order QED' is the regular result of Compton Scattering e.g. the Klein-Nishina formula and a sharp cutoff is observed at the proverbial 'Compton edge'. The 'Classical' curve shows the presence of higher harmonics but the position of these peaks in energy are wrong due to the neglect of quantum effects such as the photon recoil. Furthermore it is seen that the curves 'Volkov states' and 'Semi-Classical' also differ in the position of the first harmonic peak compared to '2nd order QED'. This is due to the Klein-Nishina formula not including the increased effective mass of the electron in the strong field. In figure 6.1.1 it is seen that already at $\chi = 0.25$ it is clear that a classical treatment is insufficient. The position of the kinematic edges when using the Volkov states are given by

$$\omega_s = \frac{4s\omega\varepsilon^2}{\bar{m}^2 + 4s\omega\varepsilon + \varepsilon^2\theta^2}, \quad (6.1.8)$$

where s is the number of absorbed photons and $\bar{m}^2 = m^2(1 + \eta^2)$ is the increased effective mass, an effect absent in the perturbative treatment (expansion in e) where $\bar{m} = m$.

6.2 The Semi-classical Operator Method

It is well known that some radiation phenomena are well described using classical electrodynamics such as synchrotron and undulator/wiggler radiation, while others, such as radiation from atomic transitions, is not. In chapter 2 we discussed the conditions under which the motion can

be considered classical and when the radiation process becomes quantum mechanical. Quantum effects become important in the radiation process when the emitted photon energy can no longer be neglected in comparison to the particle energy, meaning a condition for a classical treatment is $\omega \ll \varepsilon$, or in other words that the particle recoil due to radiation emission is negligible. Analytical applications of the semi-classical operator method show that this is equivalent with $\chi \ll 1$. We refer to [16] for a more thorough discussion of this subject. The essence of the semi-classical operator method [16][80] is the neglect of quantum effects in the motion of the energetic particle, while treating the radiation emission quantum mechanically.

The basic result of the semi-classical operator method [16] was discussed in section §2.3 and here we also noted that having to perform the double integral in time of equation (2.3.26) is numerically unfeasible, which is why we seek a form in line with the classical result of equation (2.2.1). Performing the sum over the final states and carrying out the trace of equation (2.3.25), i.e. $\rho_i = \begin{pmatrix} h & 0 \\ 0 & 1-h \end{pmatrix}$ and $\rho_f = I$, $0 \leq h \leq 1$, meaning h is the probability of a particle in the ensemble to be in the state “spin-up” with respect to the axis ζ , we obtain

$$\sum_{s_f} R_2^* R_1 = A_2^* A_1 + \mathbf{B}_2^* \cdot \mathbf{B}_1 + i(A_2^* \mathbf{B}_1 - A_1 \mathbf{B}_2^* + \mathbf{B}_2^* \times \mathbf{B}_1) \cdot \zeta, \quad (6.2.1)$$

where ζ now has a magnitude of $2h - 1$, meaning it is the degree of polarization along this axis. We denote

$$\int A_1 e^{ik'_\mu x^\mu(t_1)} dt_1 = A, \quad (6.2.2)$$

$$\int \mathbf{B}_1 e^{ik'_\mu x^\mu(t_1)} dt_1 = \mathbf{B}, \quad (6.2.3)$$

and we can thus rewrite the relevant quantity from equation (2.3.26) as

$$\begin{aligned} \iint dt_1 dt_2 \sum_{s_f} R_2^* R_1 e^{ik'_\mu(x^\mu(t_1) - x^\mu(t_2))} \\ = |A|^2 + |\mathbf{B}|^2 + i(A^* \mathbf{B} - A \mathbf{B}^* + \mathbf{B}^* \times \mathbf{B}) \cdot \boldsymbol{\zeta}. \end{aligned}$$

The structure of equation (2.3.23) and equation (2.3.24) allows us to write

$$A = C e^* \cdot \mathbf{V},$$

$$\mathbf{B} = e^* \times (D \mathbf{V} + E \mathbf{N})$$

where

$$C = \frac{1}{2} \sqrt{\frac{\varepsilon}{\varepsilon'}} \left[\sqrt{\frac{\varepsilon' + m}{\varepsilon + m}} + \sqrt{\frac{\varepsilon + m}{\varepsilon' + m}} \right], \quad (6.2.4)$$

$$D = \frac{1}{2} \sqrt{\frac{\varepsilon}{\varepsilon'}} \left(\sqrt{\frac{\varepsilon' + m}{\varepsilon + m}} - \sqrt{\frac{\varepsilon + m}{\varepsilon' + m}} \right), \quad (6.2.5)$$

$$E = \frac{1}{2} \sqrt{\frac{\varepsilon}{\varepsilon'}} \frac{\omega}{\varepsilon} \sqrt{\frac{\varepsilon + m}{\varepsilon' + m}}, \quad (6.2.6)$$

$$\mathbf{V} = \int \mathbf{v}(t) e^{ik'_\mu x^\mu(t)} dt, \quad (6.2.7)$$

$$\mathbf{N} = \int \mathbf{n} e^{ik'_\mu x^\mu(t)} dt \quad (6.2.8)$$

and $\mathbf{v}(t)$ is the particle velocity. We are currently interested in the radiation summed over the polarizations of the emitted photons and we therefore need the following identities:

$$\begin{aligned} \sum_e (\mathbf{e}^* \cdot \mathbf{a})(\mathbf{e}^* \cdot \mathbf{b}) &= \mathbf{a} \cdot \mathbf{b} - (\mathbf{n} \cdot \mathbf{a})(\mathbf{n} \cdot \mathbf{b}) \\ &= [\mathbf{n} \times (\mathbf{n} \times \mathbf{a})] \cdot [\mathbf{n} \times (\mathbf{n} \times \mathbf{b})], \quad (6.2.9) \end{aligned}$$

$$\begin{aligned} \sum_e (\mathbf{e}^* \times \mathbf{a}) \cdot (\mathbf{e} \times \mathbf{a}^*) &= \mathbf{a} \cdot \mathbf{a} + (\mathbf{n} \cdot \mathbf{a})(\mathbf{n} \cdot \mathbf{a}^*) \\ &= |\mathbf{n} \times (\mathbf{n} \times \mathbf{a})|^2 + 2|\mathbf{n} \cdot \mathbf{a}|^2, \quad (6.2.10) \end{aligned}$$

$$\begin{aligned} \sum_e (\mathbf{e}^* \times \mathbf{a}) \cdot \boldsymbol{\zeta}(\mathbf{e} \cdot \mathbf{b}) \\ &= [\mathbf{n} \times (\mathbf{n} \times [\mathbf{a} \times \boldsymbol{\zeta}])] \cdot [\mathbf{n} \times (\mathbf{n} \times \mathbf{b})], \quad (6.2.11) \end{aligned}$$

$$\begin{aligned} \sum_e \boldsymbol{\zeta} \cdot (\mathbf{e} \times \mathbf{a}^*) \times (\mathbf{e}^* \times \mathbf{a}) \\ &= [\mathbf{n} \times (\mathbf{n} \times \boldsymbol{\zeta})] \cdot [\mathbf{n} \times (\mathbf{n} \times (\mathbf{a}^* \times \mathbf{a}))]. \quad (6.2.12) \end{aligned}$$

We then obtain

$$\begin{aligned} \iint dt_1 dt_2 \sum_{s_f, e} R_2^* R_1 e^{ik'_\mu(x^\mu(t_1) - x^\mu(t_2))} &= (C^2 + D^2) |\mathbf{n} \times (\mathbf{n} \times \mathbf{V})|^2 + 2|\mathbf{n} \cdot (D\mathbf{V} + E\mathbf{N})|^2 \\ &+ i \{2iC \text{Im}([\mathbf{n} \times (\mathbf{n} \times \mathbf{V}^*)] \cdot [\mathbf{n} \times (\mathbf{n} \times (D\mathbf{V} + E\mathbf{N}) \times \boldsymbol{\zeta}))]) \\ &+ [\mathbf{n} \times (\mathbf{n} \times \boldsymbol{\zeta})] \cdot [\mathbf{n} \times (\mathbf{n} \times (D\mathbf{V} + E\mathbf{N})^* \times [D\mathbf{V} + E\mathbf{N}])]\}. \quad (6.2.13) \end{aligned}$$

One must then expand the values of the coefficients, C , D and E in orders of $\frac{1}{\gamma}$ and insert these into equation (6.2.13) and keep only the leading order in $\frac{1}{\gamma}$. In addition we use

$$\begin{aligned} \mathbf{N} - \mathbf{V} &= \int (\mathbf{n} - \mathbf{v}) e^{ik'x} dt \\ &= \int \mathbf{n} \times (\mathbf{n} \times \mathbf{v}) e^{ik'x} dt \\ &= -\frac{1}{i\omega'} \int \mathbf{f}(t, \mathbf{n}) e^{ik'x} dt = \frac{i}{\omega'} \mathbf{I}, \quad (6.2.14) \end{aligned}$$

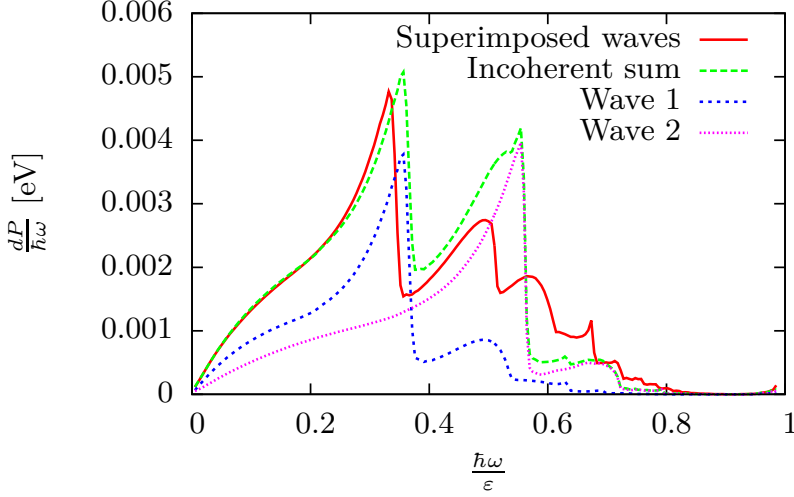


Figure 6.2.1: A figure of the power spectra using the semi-classical operator method for the electron in each wave separately, 'Wave 1' and 'Wave 2', and in the superposition of the two waves 'Superimposed waves'. The latter is noticeably different than 'Incoherent sum' which is the sum of the spectra of 'Wave 1' and 'Wave 2'. The fields are characterized by $\omega_1 = 2.35\text{eV}$, $\eta_1 = \frac{1}{2}$, $\chi_1 = \frac{1}{4}$ and $\omega_2 = 2\omega_1$, $\eta_2 = \frac{1}{2\sqrt{2}}$, $\chi_2 = \frac{1}{2\sqrt{2}}$.

and

$$\begin{aligned}
 \int e^{ik'x} dt &= \int \mathbf{n} \cdot \mathbf{v} e^{ik'x} dt \\
 &= \int \frac{\mathbf{n} \cdot \mathbf{v}}{1 - \mathbf{n} \cdot \mathbf{v}} \frac{1}{i\omega'} \frac{d}{dt} (e^{ik'x}) dt \\
 &= -\frac{1}{i\omega'} \int \frac{\mathbf{n} \cdot \dot{\mathbf{v}}}{(1 - \mathbf{n} \cdot \mathbf{v})^2} e^{ik'x} dt = \frac{i}{\omega'} J, \quad (6.2.15)
 \end{aligned}$$

where we have defined

$$\mathbf{I} = \int \mathbf{f}(t, \mathbf{n}) e^{ik'x} dt, \quad (6.2.16)$$

$$J = \int \frac{\mathbf{n} \cdot \dot{\mathbf{v}}}{(1 - \mathbf{n} \cdot \mathbf{v})^2} e^{ik'x} dt. \quad (6.2.17)$$

In this calculation we performed integration by parts and the fact that $\mathbf{n} \cdot \mathbf{v} e^{ik'x(t)} = \left(1 - \frac{1}{i\omega'} \frac{d}{dt}\right) e^{ik'x(t)}$ where the second term will vanish. These integration tricks can be seen used in [16]. The term $D\mathbf{V} + E\mathbf{N}$ can be written as

$$D\mathbf{V} + E\mathbf{N} = \frac{\omega}{2\varepsilon'}(\mathbf{N} - \mathbf{V}) + \frac{m}{4\varepsilon} \left(\frac{\varepsilon^2}{\varepsilon'^2} - 1\right) \mathbf{V} + \frac{\omega m}{4\varepsilon'} \left(\frac{1}{\varepsilon} - \frac{1}{\varepsilon'}\right) \mathbf{N}. \quad (6.2.18)$$

Using equation (6.2.14) we have $\mathbf{V} = \mathbf{N} - \frac{i}{\omega'} \mathbf{I}$. Using this in equation (6.2.18) and the identity $\mathbf{n} \times (\mathbf{n} \times (\mathbf{n} \times \mathbf{a})) = -\mathbf{n} \times \mathbf{a}$, one can write the final expression as

$$\begin{aligned} \frac{d^2 I}{d\omega d\Omega} = \frac{e^2}{4\pi^2} & \left(\frac{\varepsilon'^2 + \varepsilon^2}{2\varepsilon^2} |\mathbf{I}|^2 + \frac{1}{2} \frac{\omega^2 m^2}{\varepsilon^4} |J|^2 \right. \\ & + \frac{\omega m}{2\varepsilon^3} \{(\varepsilon' + \varepsilon) \text{Im} [\mathbf{I}^* \cdot (\mathbf{n} \times \boldsymbol{\zeta}) J] \\ & - \omega [\mathbf{n} \times (\mathbf{n} \times \boldsymbol{\zeta})] \text{Im} [(\mathbf{n} \times \mathbf{I}^*) J]\} \\ & \left. - \frac{(\varepsilon' + \varepsilon)\omega}{2\varepsilon^2} \text{Im} \{ \mathbf{I}^* \cdot [\mathbf{n} \times (\mathbf{n} \times (\mathbf{I} \times \boldsymbol{\zeta}))] \} \right) \quad (6.2.19) \end{aligned}$$

The quantities of equation (6.2.16) and equation (6.2.17) can be calculated numerically, as will be described in section §6.4, and therefore the general result of equation (6.2.19) allows one to numerically calculate the radiation emitted from a polarized electron beam in any electromagnetic field. The general result of equation (6.2.19) could for instance be used to perform numerical calculations of strong field radiation emission during channeling in crystals with polarized electron/positron beams, or the beamstrahlung of polarized beams in future linear colliders. Setting $|\boldsymbol{\zeta}| = 0$ i.e. an unpolarized electron beam, one obtains

$$\frac{d^2 I}{d\omega d\Omega} = \frac{e^2}{4\pi^2} \left(\frac{\varepsilon'^2 + \varepsilon^2}{2\varepsilon^2} |\mathbf{I}|^2 + \frac{\omega^2 m^2}{2\varepsilon^4} |J|^2 \right). \quad (6.2.20)$$

This result can also be found in [81], but is stated without proof, and a derivation can not be found in any of the cited papers. The more general formula of equation (6.2.19) is a new result.

These formulas are valid as long as the semi-classical operator method is valid. To reiterate we must have $\gamma \gg 1$.

6.3 Compton Interference

The procedure for finding the radiation spectrum is then in principle straight forward: Find the motion of the particle $x^\mu(t)$ by solving the Lorentz force equation in the strong field and then for each photon energy ω , calculate an angular distribution from equation (6.2.20) over an appropriately chosen region, which is then integrated over angles.

The main result of this chapter is shown in figure 6.2.1. Here we use the semi-classical method to obtain a power spectrum when an electron moves in the superposition of two plane waves and compare this spectrum with that obtained if the electron moved in each wave individually. Additionally we compare with the 'Incoherent sum' which is the sum of the spectra 'Wave 1' and 'Wave 2' and would be the expected result in the linear regime, $\eta \ll 1$, which is illustrated in figure 6.4.1. In figure 6.1.2 a direct comparison of this approach for a single plane wave with that obtained using the traditional method of Volkov states is seen. The plane wave fields are characterized by $\omega_1 = 2.35\text{eV}$, $\omega_2 = 2\omega_1$, $\eta_1 = \frac{1}{2}$, $\chi_1 = 0.25$, $\eta_2 = \frac{1}{2\sqrt{2}}$, $\chi_2 = 0.36$. These parameters correspond to an electron energy $\varepsilon = 20.0\text{GeV}$ and laser r.m.s. intensities of $I_1 = 2.46 \times 10^{22} \frac{\text{W}}{\text{m}^2}$ and $I_2 = 4.91 \times 10^{22} \frac{\text{W}}{\text{m}^2}$. The field describing the 'Superimposed waves' is given by

$$E_x = E_1 e^{i(\omega_0(t+z))} + E_2 e^{i(2\omega_0(t+z))}, \quad (6.3.1)$$

$$B_y = -E_x, \quad (6.3.2)$$

and the remaining components are 0. 10TW of peak power is available with modern laser systems at this wavelength which limits the intensity at the diffraction limit to about $10^{25} \frac{\text{W}}{\text{m}^2}$. The agreement in figure 6.1.1 and figure 6.1.2 is very good. The numerical calculation uses a finite time interval corresponding to $N = 15$ electron oscillations in the laser field

for ω_1 and $N = 30$ for ω_2 , while the analytical results are in the limit of $N \rightarrow \infty$ and this is the cause of the slight disagreement near the peaks in figure 6.1.1 and figure 6.1.2. It is seen in figure 6.2.1 that the radiation emission in the superimposed waves, near the second harmonic peak, is suppressed below the result from just having 'Wave 2', and should be understood as destructive interference between the two processes involved.

6.4 General considerations and numerical implementation

While analytically solving equation (6.2.20) is difficult without making considerable approximations even in the simple case of a plane wave, one can in principle study Compton scattering in any field configuration using numerical methods. This is unfeasible in the complete quantum treatment i.e. finding numerical solutions of the Dirac equation including the strong field, equation (6.1.1), beyond the cases where the Volkov solution of equation (6.1.3) can be used. From equation (6.2.19) it is evident that the motion of the electron completely determines the spectrum of emitted radiation, as is the case classically. We can therefore immediately see that some cases of radiation emission are equivalent, for instance the case considered here with two linearly polarized plane waves colliding head on with the electron where $\omega_2 = 2\omega_1$ is equivalent with the case where two plane waves of the same photon energy, but where one collides head-on, and the other at a 90° angle (and parallel polarizations), or that the radiation from a spatially modulated laser pulse due to e.g. focusing is equivalent to the radiation from a similarly temporally modulated laser pulse, if the pulse shape is otherwise the same. One can also show how the kinematic relation equation (6.1.8) arises from the semi-classical approach. In order to calculate the quantities of equation (6.2.16) and equation (6.2.17) we rewrite the components of \mathbf{f} of equation (2.2.2) as seen in equation (2.2.5) to equation (2.2.7)

and

$$\mathbf{n} \cdot \dot{\mathbf{v}} = g \{ \theta_x \dot{v}_x + \theta_y \dot{v}_y + \delta \dot{v}_z \}, \quad (6.4.1)$$

and the exponential phase now becomes

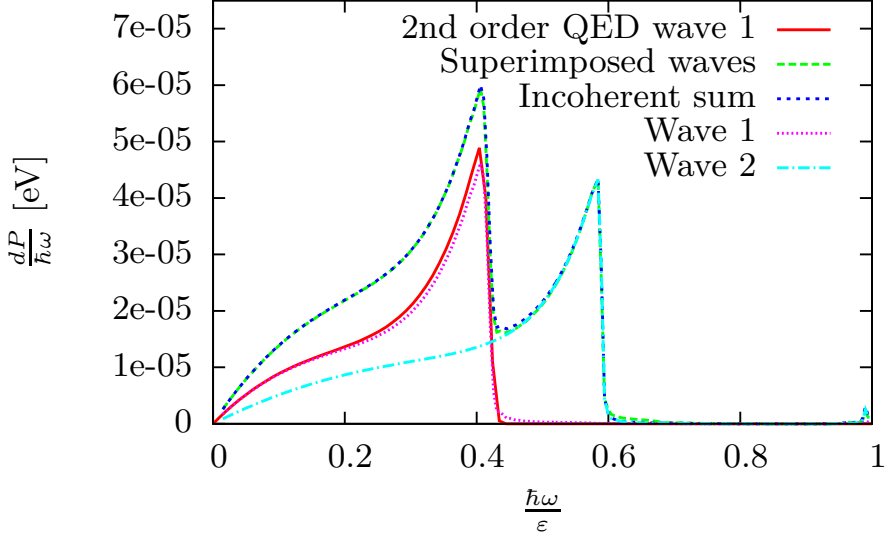


Figure 6.4.1: A figure of the radiation power spectra in a weak field, $\eta \ll 1$. The spectrum 'Superimposed waves' is seen to overlap with 'Incoherent sum' as expected. In '2nd order QED wave 1' we compare the result of 'Wave 1' to that of Compton scattering as obtained from the 2nd order of perturbation in QED (Klein-Nishina).

$$k'x = \frac{\varepsilon}{\varepsilon'}\omega \left(\left(\frac{1}{2\gamma^2} + \frac{\theta^2}{2} \right)t - \delta z(t) - \mathbf{n}_\perp \cdot \mathbf{x}_\perp(t) \right). \quad (6.4.2)$$

f_z is suppressed by $\frac{1}{\gamma}$ compared to f_x and f_y and can thus, in most cases, be neglected. The relative sizes of the quantities in equation (6.4.2) determine the nature of the radiation, dipole- or synchrotron-like, or in the language of quantum mechanics, single-photon or multiphoton absorption from the field of the plane wave. Consider the case when the phase-terms containing the motion are negligible, then one is left with

$$k'x \simeq \frac{\varepsilon}{\varepsilon'}\frac{\omega}{2\gamma^2}t \left(1 + \gamma^2\theta^2 \right), \quad (6.4.3)$$

meaning the relevant angular sizes are $\theta \sim 1/\gamma$. This approximation is therefore no longer applicable when the particle oscillation angle is $\mathbf{v}_\perp \sim \frac{1}{\gamma}$ or larger. By using the Lorentz force formula on a particle in a plane wave field, this is seen to be equivalent with the condition that the transition from single- to multiphoton absorption is $\eta \lesssim 1$ and $\eta \gtrsim 1$, as expected from the discussion in section §6.1.

Consider now the case of an electron colliding head-on with a linearly polarized plane wave with frequency ω_0 given by

$$E_x = E_1 e^{i(\omega_0(t+z))} \quad (6.4.4)$$

$$B_y = -E_x, \quad (6.4.5)$$

and the remaining components being 0. The Lorentz force along with $m\dot{\gamma} = e\mathbf{E} \cdot \mathbf{v}$ gives then the solution to leading order in $\frac{1}{\gamma^2}$ as

$$v_x = \frac{\sqrt{2}\eta}{\gamma} \text{Re}(e^{2i\omega_0 t}), \quad (6.4.6)$$

$$v_z = -\frac{1}{2}v_x^2 + \beta_0, \quad (6.4.7)$$

meaning $\delta v_z = -\frac{1}{2}v_x^2$. It is then clear that we can write \mathbf{f} as a Fourier series in the frequency $2\omega_0$, that is

$$\mathbf{f} = \sum_s \mathbf{c}_s e^{-2i\omega_0 s t}. \quad (6.4.8)$$

The integrand from equation (6.2.20) then becomes

$$\sum_s \mathbf{c}_s e^{\frac{\varepsilon}{\varepsilon'} \omega \left(\left(\frac{1}{2\gamma^2} + \frac{\theta^2}{2} \right) t - \delta z(t) - \mathbf{n}_\perp \cdot \mathbf{x}_\perp(t) \right) - 2i\omega_0 s t}. \quad (6.4.9)$$

Time averaging over the oscillating terms in the phase yields

$$\sum_s \mathbf{c}_s e^{\frac{\varepsilon}{\varepsilon'} \omega t \left(\frac{1}{2\gamma^2} + \frac{\theta^2}{2} + \frac{\eta^2}{2\gamma^2} \right) - 2i\omega_0 s t}. \quad (6.4.10)$$

The same can be done for the other term of equation (6.2.17). Using this when performing the integration over time in equation (6.2.20) gives delta

functions $\delta(\frac{\varepsilon}{\varepsilon'}\omega(\frac{1}{2\gamma^2} + \frac{\theta^2}{2} + \frac{\eta^2}{2\gamma^2}) - 2s\omega_0)$ which gives the kinematic condition of equation (6.1.8). Thus, in this picture the kinematic edge is shifted due to the fact that δv_z has a non-zero time-averaged value of $\langle \delta v_z \rangle = -\frac{\eta^2}{2\gamma^2}$, i.e. the electron is effectively slowed down in the z -direction due to the oscillation in the strong field. A mass shift is therefore expected in any oscillatory field which can be characterized as “strong” in the classical sense. It is puzzling that an investigation of Compton scattering in an ultra-short pulse reports results where this mass-shift is absent [72], although see [77] for a recent discussion of the presence of the mass-shift. As mentioned previously and seen in figure 6.4.1, the results for the superimposed waves reduces to the ‘incoherent sum’ in the dipole case, $\eta \ll 1$. This is seen most easily from equation (6.2.14). To lowest order in the “small” quantities the integrand $\mathbf{n} \times (\mathbf{n} \times \mathbf{v})$ does not depend on δv_z and is linear in \mathbf{v}_\perp . The orthogonal motion of an electron in the superimposed waves will, to leading order in $\frac{\eta^2}{\gamma^2}$, be the sum of the orthogonal motions had the electron moved in each wave individually. This means in the dipole case, $\eta \ll 1$, where the phase reduces to that of equation (6.4.3), the radiation spectrum is proportional to the norm square of the Fourier transform of the orthogonal motion. By the above arguments, this means that the differential spectrum in the superimposed waves is proportional to $|F_1(\omega, \Omega) + F_2(\omega, \Omega)|^2$ where F are the Fourier integrals of equation (6.2.20) corresponding to ‘Wave 1’ and ‘Wave 2’. This gives the spectra from each wave individually along with an interference term $2\text{Re}(F_1(\omega, \Omega)F_2(\omega, \Omega))$ but from equation (6.4.6) it is clear that the motion is harmonic, and therefore F_1 and F_2 do not overlap and thus the interference term vanishes. Therefore in weak fields, the radiation spectrum is simply the ‘incoherent sum’ of the spectra corresponding to scattering with each field individually, i.e. we have linearity and the notion of a cross-section is sensible. As η increases the terms neglected in the dipole case will contribute, introducing anharmonic content in the integrand of equation (6.2.20) and this interference term becomes significant as seen in figure 6.2.1. The numerical calculations were carried out by solving the system of ordinary differential equations resulting from the Lorentz force equation for the small quantities $\mathbf{x}_\perp(t)$, $\mathbf{v}_\perp(t)$, $\delta z(t)$ and $\delta v_z(t)$. The angular spectrum of radiation was calculated numerically based on equation (6.2.20) and equation (2.2.5) to equation (2.2.7) and equation (6.4.1) to equation (6.4.2) on a 160×160 grid of θ_x and

θ_y over an appropriate angular range aided by the kinematic condition of equation (6.1.8).

Chapter 7

Quantum synchrotron radiation in the case of a field with finite extension

The content of this chapter is identical to that of my paper [5], but without the section introducing the theoretical formalism, as this has already been shown in chapter 6.

In this chapter I will, as in chapter 6, investigate radiation emission by electrons in a nontrivial field configuration. This study was carried out during my stay in the Compact Linear Collider (CLIC) collaboration at CERN which is a conceptual future particle accelerator of electrons and positrons. My study was concerned with the radiation emitted during the collisions of the electron and positron bunches in the interaction region. During this crossing, radiation is emitted in abundance due to the strong electromagnetic field present due to the high charge density of the bunches. The radiation emitted due to this collective field of all the charges much surpasses that emitted in the individual binary collisions, i.e. the traditional bremsstrahlung. This type of radiation has been termed 'beamstrahlung' but the calculation is in principle quite simple as it is based on the formula for quantum synchrotron radiation, i.e. radiation emission by an electron in a constant magnetic field. The field encountered by a particle in one bunch colliding with the other bunch is, however, not constant - but under certain circumstances the radiation emission in a varying field

can be calculated by using the constant field formula if the field can be said to vary 'slowly'. A central concept of what can be defined as a slow variation of the field is that of the formation length of radiation which will be discussed in this chapter. I investigate the concern of using the constant field approximation by doing a detailed analysis of the radiation emission process when the field extension becomes short as in e.g. a short bunch in CLIC.

The result of quantum synchrotron radiation was first derived by N.P. Klepikov [82] and has been studied by several notable physicists in the field of QED [83], [84], [85]. The semi-classical operator method as already discussed in chapter 2 and chapter 6 provides a powerful method for the calculation of such processes. In section §7.1 I discuss the usual result of quantum synchrotron radiation and when the field should be considered 'short'. In section §7.2 I discuss the results of the numerical solution in the limit of 'short' and 'long' extensions of the field, as well as what happens in the intermediate region. In section §7.3 I derive an analytical formula for the radiation spectrum in the limit of a 'short' extension of the field. In section §7.4 I discuss the relevance of the obtained results in future colliders and how one could study these phenomena experimentally.

7.1 Synchrotron radiation

Because of the similarity of equation (6.2.20) with the classical result, one can follow a calculation completely analogous to the one found in [21] to obtain the distribution of synchrotron radiation, but valid also in the quantum case. Synchrotron radiation is obtained by using equation (6.2.20) and the motion as described by

$$v_x = v \sin\left(\frac{vt}{R}\right), \quad (7.1.1)$$

$$v_y = 0, \quad (7.1.2)$$

$$v_z = v \cos\left(\frac{vt}{R}\right), \quad (7.1.3)$$

where $R = \frac{p}{eB}$ is the radius of curvature, v the velocity and t the time coordinate. To obtain \mathbf{I} we calculate $\int (\mathbf{n} - \mathbf{v}) e^{ik'x} dt$, see equation (6.2.14). Due to the symmetry of the motion it is known a priori that the radiation spectrum must be independent of θ_x and thus we can choose our coordinate system such that $\theta_x = 0$ as done in [21]. This means $\theta = \theta_y$. Then we can calculate the phase using equation (6.4.2)

$$k'x = \omega' \left(\left(\frac{1}{2\gamma^2} + \frac{\theta^2}{2} \right) t + \frac{t^3}{6R^2} \right). \quad (7.1.4)$$

We then find

$$\begin{aligned} \int_{-\infty}^{\infty} (\mathbf{n} - \mathbf{v})_x e^{ik'x} dt &= \int_{-\infty}^{\infty} -v \sin \left(\frac{vt}{R} \right) e^{ik'x} dt \\ &= -\frac{v^2}{R} \int_{-\infty}^{\infty} t e^{ik'x} dt \\ &= -\frac{1}{R} \int_{-\infty}^{\infty} t e^{i \frac{\omega' t}{2} \left(\theta^2 + \frac{1}{\gamma^2} + \frac{v^2 t^2}{3R^2} \right)} dt \quad (7.1.5) \end{aligned}$$

Changing variable to $x = \frac{t}{R\sqrt{\frac{1}{\gamma^2} + \theta^2}}$ and introducing $\xi = \frac{\omega'R}{3} \left(\frac{1}{\gamma^2} + \theta^2 \right)^{\frac{3}{2}}$

this becomes

$$\begin{aligned} \int_{-\infty}^{\infty} (\mathbf{n} - \mathbf{v})_x e^{ik'x} dt &= -R \left(\frac{1}{\gamma^2} + \theta^2 \right) \int_{-\infty}^{\infty} x \exp \left(i \frac{3}{2} \xi \left(x + \frac{x^3}{3} \right) \right) dx \\ &= -R \left(\frac{1}{\gamma^2} + \theta^2 \right) \frac{2i}{\sqrt{3}} K_{2/3}(\xi) \quad (7.1.6) \end{aligned}$$

where K_α denotes the modified Bessel function of the second kind of order α . Similarly we calculate

$$\begin{aligned}
 \int_{-\infty}^{\infty} (\mathbf{n} - \mathbf{v})_y e^{ik'x} dt &= \theta \int_{-\infty}^{\infty} e^{i\frac{\omega'}{2}t(\theta^2 + \frac{1}{\gamma^2} + \frac{v^2 t^2}{3R^2})} dt \\
 &= R\theta \left(\frac{1}{\gamma^2} + \theta^2\right)^{\frac{1}{2}} \int_{-\infty}^{\infty} \exp(i\frac{3}{2}\xi(x + \frac{x^3}{3})) dx \\
 &= R\theta \left(\frac{1}{\gamma^2} + \theta^2\right)^{\frac{1}{2}} \frac{2}{\sqrt{3}} K_{1/3}(\xi) \quad (7.1.7)
 \end{aligned}$$

To calculate J we need to calculate (see equation (6.2.15)).

$$\begin{aligned}
 \int_{-\infty}^{\infty} e^{ik'x} dt &= \int_{-\infty}^{\infty} e^{i\frac{\omega'}{2}t(\theta^2 + \frac{1}{\gamma^2} + \frac{v^2 t^2}{3R^2})} dt \\
 &= R \left(\frac{1}{\gamma^2} + \theta^2\right)^{\frac{1}{2}} \frac{2}{\sqrt{3}} K_{1/3}(\xi) \quad (7.1.8)
 \end{aligned}$$

We therefore obtain

$$\begin{aligned}
 |\mathbf{I}|^2 &= \omega'^2 \left(R^2 \left(\frac{1}{\gamma^2} + \theta^2\right)^2 \frac{4}{3} K_{2/3}^2(\xi) \right. \\
 &\quad \left. + R^2 \theta^2 \left(\frac{1}{\gamma^2} + \theta^2\right) \frac{4}{3} K_{1/3}^2(\xi) \right) \\
 &= \frac{\varepsilon^2}{\varepsilon'^2} (\omega R)^2 \frac{4}{3} \left(\frac{1}{\gamma^2} + \theta^2\right)^2 \left(K_{2/3}^2(\xi) + \frac{\theta^2}{\frac{1}{\gamma^2} + \theta^2} K_{1/3}^2(\xi) \right) \quad (7.1.9)
 \end{aligned}$$

And

$$\begin{aligned}
 |J|^2 &= \omega'^2 \left[R \left(\frac{1}{\gamma^2} + \theta^2\right)^{\frac{1}{2}} \frac{2}{\sqrt{3}} K_{1/3}(\xi) \right]^2 \\
 &= \frac{\varepsilon^2}{\varepsilon'^2} (\omega R)^2 \left(\frac{1}{\gamma^2} + \theta^2\right) \frac{4}{3} K_{1/3}^2(\xi) \quad (7.1.10)
 \end{aligned}$$

By using equation (6.2.20) we obtain the energy spectrum of synchrotron radiation as

$$\begin{aligned} \frac{d^2 I}{d\omega d\Omega} = & \frac{e^2}{3\pi^2} (\omega R)^2 \left(\frac{\varepsilon'^2 + \varepsilon^2}{2\varepsilon'^2} \left(\frac{1}{\gamma^2} + \theta^2 \right)^2 \right. \\ & \times \left(K_{2/3}^2(\xi) + \frac{\theta^2}{\frac{1}{\gamma^2} + \theta^2} K_{1/3}^2(\xi) \right) \\ & \left. + \frac{\omega^2 m^2}{2(\varepsilon\varepsilon')^2} \left(\frac{1}{\gamma^2} + \theta^2 \right) K_{1/3}^2(\xi) \right) \quad (7.1.11) \end{aligned}$$

By writing $d\Omega = d\theta_x d\theta_y$ and integrating over θ_x from 0 to 2π and dividing by the period $2\pi R$ the differential power spectrum is obtained as

$$\begin{aligned} \frac{dP}{d\omega d\theta} = & \frac{e^2}{3\pi^2 R} (\omega R)^2 \left(\frac{\varepsilon'^2 + \varepsilon^2}{2\varepsilon'^2} \left(\frac{1}{\gamma^2} + \theta^2 \right)^2 \right. \\ & \times \left(K_{2/3}^2(\xi) + \frac{\theta^2}{\frac{1}{\gamma^2} + \theta^2} K_{1/3}^2(\xi) \right) \\ & \left. + \frac{\omega^2 m^2}{2(\varepsilon\varepsilon')^2} \left(\frac{1}{\gamma^2} + \theta^2 \right) K_{1/3}^2(\xi) \right) \quad (7.1.12) \end{aligned}$$

This formula is valid in the quantum regime as well. Integrating equation (7.1.12) over θ yields the usual result of quantum synchrotron radiation given by [16]

$$\begin{aligned} \frac{dP}{d\omega} = & \frac{e^2 m^2}{\pi\sqrt{3}} \frac{u}{(1+u)^3} \frac{du}{d\omega} \times \\ & \left(\frac{u^2}{1+u} K_{2/3}\left(\frac{2u}{3\chi}\right) + \int_{\frac{2u}{3\chi}}^{\infty} K_{5/3}(y) dy \right) \quad (7.1.13) \end{aligned}$$

where $u = \frac{\omega}{\varepsilon'}$. The integral of this spectrum wrt. the photon energy gives the total power which we denote P_0 .

In this calculation a circular motion is assumed, lasting for times $-\infty < t < \infty$, as seen in equation (7.1.1) to equation (7.1.3). In the case of a field with finite extension the motion can be characterized by that of equation (7.1.1) to equation (7.1.3) when $-\frac{L}{2} < t < \frac{L}{2}$ and that the acceleration is 0 otherwise. For this reason we employ the formulas for \mathbf{I} and J where the integrand is proportional to the acceleration such that the only difference in the numerical calculation is changing the integration limit. From equation (7.1.3) it can be shown that the condition $-\frac{L}{2} < t < \frac{L}{2}$ differs from the condition $-\frac{L}{2} < z < \frac{L}{2}$ only with a relative correction on the order of $\frac{1}{\gamma^2} + \frac{L^2}{R^2}$ which means that whether the field has a finite extension in time or in the z -direction is equivalent. The \mathbf{I} term

$$\mathbf{I} = \int_{-\infty}^{\infty} \mathbf{f}(t, \mathbf{n}) e^{ik'x} dt, \quad (7.1.14)$$

becomes

$$\mathbf{I} = \int_{-\frac{L}{2}}^{\frac{L}{2}} \mathbf{f}(t, \mathbf{n}) e^{ik'x} dt, \quad (7.1.15)$$

and similarly for the J term. The angular distribution is then no longer known to be independent of θ_x and the integration limits means an analytical expression is no longer easily obtained. We can argue how small L should be for the difference between these two integrals to be significant. The formation length is the length over which the contributions from different parts of the trajectory add coherently and by setting $\phi \sim 1$ from equation (6.4.2). The corresponding length is given by

$$l_f = \frac{2\gamma^2}{\omega'} = \frac{2\gamma^2(\varepsilon - \omega)}{\omega\varepsilon}. \quad (7.1.16)$$

We can therefore recognize two cases. When $L \gg l_f$ we are in the usual regime of synchrotron radiation, while if $L \ll l_f$ the extension of the field can no longer be neglected. We therefore obtain the condition

$$\frac{\omega}{\varepsilon} \ll \frac{1}{1 + \frac{\varepsilon L}{2\gamma^2}} \quad (7.1.17)$$

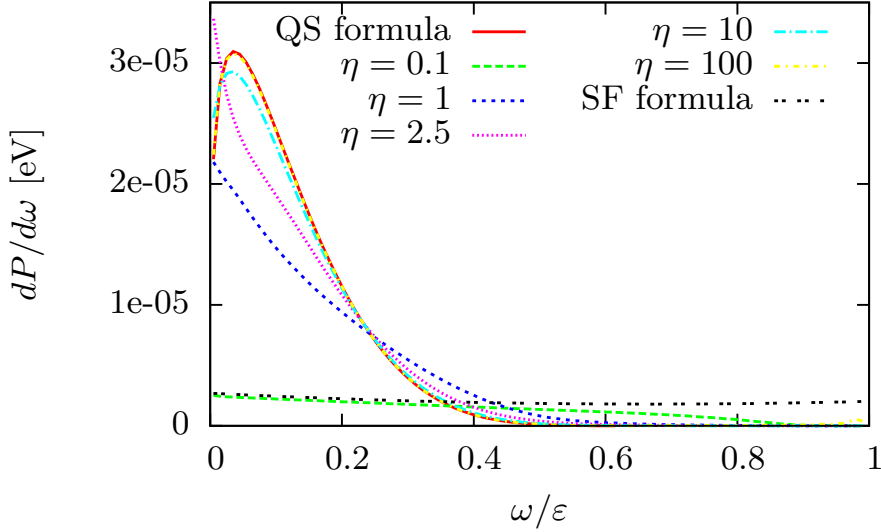


Figure 7.1.1: A plot of the power spectra for the case $\chi = 0.1$, $\varepsilon = 1.5\text{TeV}$ and different values of η . 'QS formula' is the formula of quantum synchrotron radiation seen in equation (7.1.13). 'SF formula' is the 'short field' formula of equation (7.3.11) for the case of $\eta = 0.1$.

If I define $\eta = \gamma \frac{L}{R}$, meaning η is the deflection angle in units of $1/\gamma$, we can express the length as

$$L = \frac{\eta\gamma}{m\chi} \quad (7.1.18)$$

and so the condition becomes

$$\frac{\omega}{\varepsilon} \ll \frac{1}{1 + \frac{\eta}{2\chi}} \quad (7.1.19)$$

We can thus consider the four cases

Case 1: $\eta \leq 1$ and $\eta \leq \chi$, the limit of short field extension

$\eta \leq 1$ is also commonly referred to as the dipole case and from equation (7.1.19) we see that the spectrum is modified for all photon energies

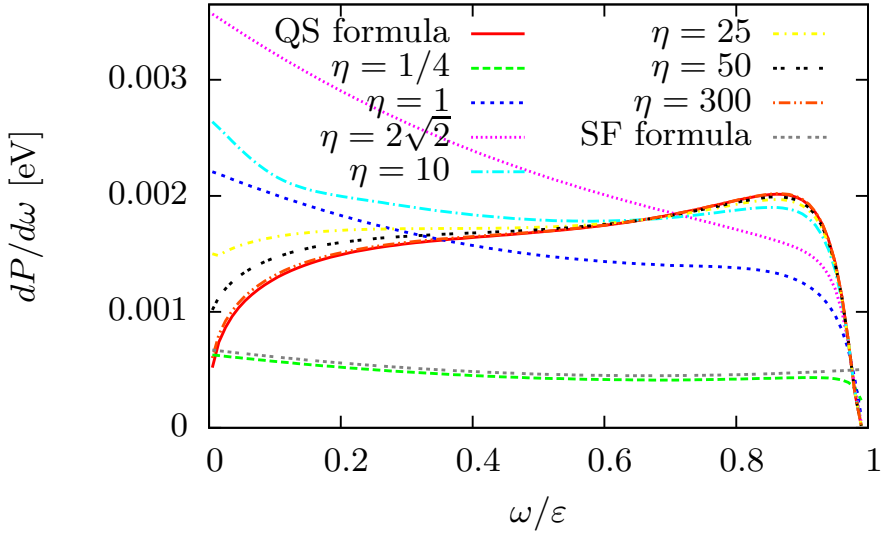


Figure 7.1.2: A plot of the power spectra for the case $\chi = 10$, $\varepsilon = 1.5\text{TeV}$ and different values of η . 'QS formula' is the formula of quantum synchrotron radiation seen in equation (7.1.13). 'SF formula' is the 'short field' formula of equation (7.3.11) for the case of $\eta = 1/4$.

up to the initial electron energy. In section §7.3 we will derive an analytical result applicable in this case.

Case 2: $\eta \leq 1$ and $\eta \geq \chi$, the intermediate classical case

In this case we are still in the dipole case and the spectrum is modified when $\frac{\omega}{\varepsilon} \lesssim \frac{2\chi}{\eta}$ this means the spectrum is modified below frequencies of $\frac{1}{\eta}$ times the critical synchrotron frequency ω_c and is here given approximately by the dipole formula as shown in section §7.3. Since $\eta \leq 1$ this means the spectrum will always be modified at the critical synchrotron frequency or above. At photon energies above those corresponding to $\frac{\omega}{\varepsilon} \simeq \frac{2\chi}{\eta}$ the spectrum will transition to that of synchrotron radiation, which is vanishing above the critical frequency. This means that one has a dipole spectrum up to this limit and then the spectrum will die out. An accurate spectrum

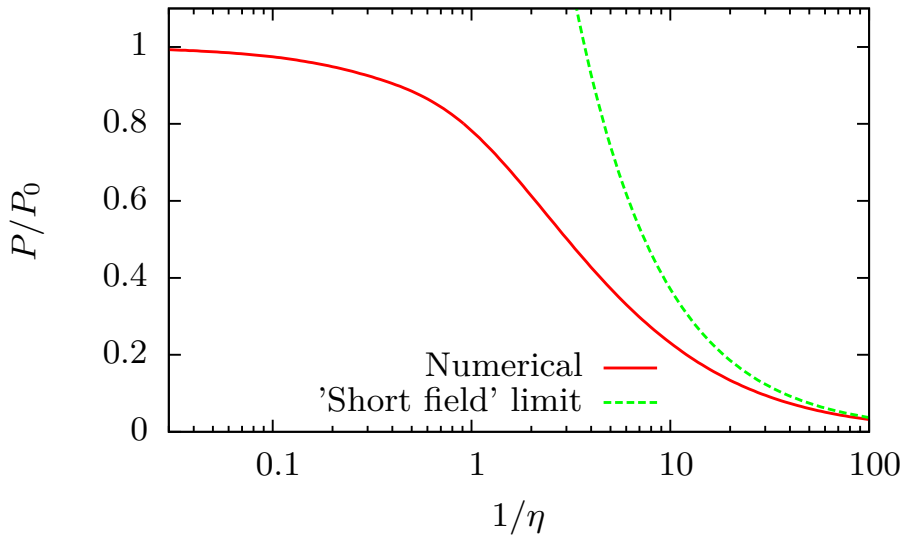


Figure 7.1.3: A plot of the total power emitted in units of P_0 as function of $1/\eta$. In this case $\chi = 0.1$. The red curve is obtained by the numerical procedure described in the text and the green dashed curve is a plot of equation (7.3.12).

can in this case only be obtained numerically.

Case 3: $\eta \geq 1$ and $\eta \leq \chi$, the intermediate quantum case

In this case the radiation spectrum is modified at roughly all photon energies and must also be calculated numerically.

Case 4: $\eta \geq 1$ and $\eta \geq \chi$, the limit of large field extension

In this case the spectrum is modified when $\frac{\omega}{\varepsilon} \lesssim \frac{2\chi}{\eta}$ which means the spectrum is modified below frequencies of $\frac{1}{\eta}$ times the critical synchrotron frequency ω_c . Since $\eta \geq 1$ this means the spectrum will always be modified only below the critical frequency, and thus for higher frequencies the

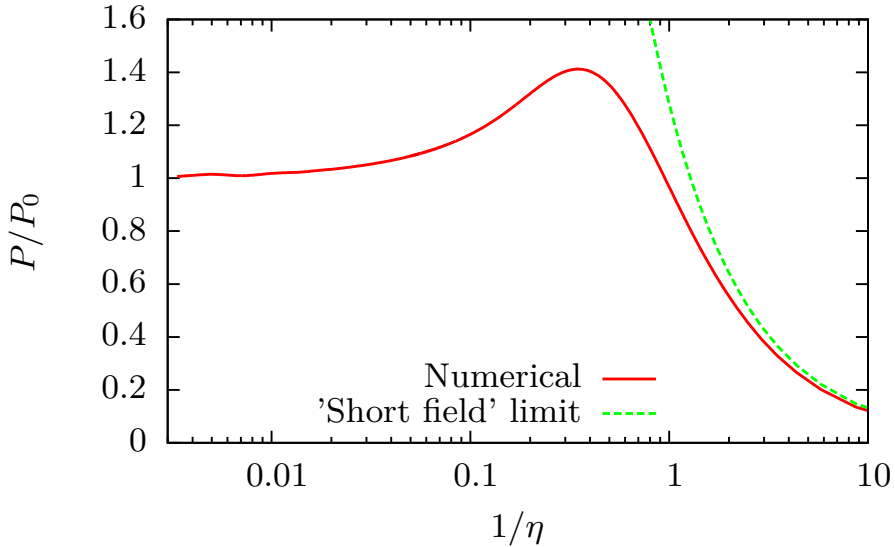


Figure 7.1.4: A plot of the total power emitted in units of P_0 as function of $1/\eta$. In this case $\chi = 10$. The red curve is obtained by the numerical procedure described in the text and the green dashed curve is a plot of equation (7.3.12).

spectrum is that of the usual synchrotron radiation. In the limit $\eta \gg \chi$ one obtains the usual result of equation (7.1.13).

From these 4 cases it is seen that whether one is in the classical case, $\chi \lesssim 1$ or the quantum case $\chi \gtrsim 1$ makes an important difference. In the classical case, as one transitions from larger to smaller values of η one goes from case 4 to case 2 and then to case 1. In the quantum case one goes from case 4 to case 3 and then to case 1. We can therefore define two characteristic lengths which determine the extension of the field where deviation from the usual synchrotron result is seen. In the classical case the transition from the usual result happens when one transitions from case 4 to case 2 i.e. $\eta \sim 1$, using equation (7.1.18) we thus define the characteristic classical length as

$$l_c = \frac{\gamma}{m\chi}. \quad (7.1.20)$$

In conventional units this does not contain \hbar and is indeed a classical quantity. In the quantum case the transition takes place when between case 4 and 3 i.e. when $\eta \sim \chi$ and thus we define the characteristic quantum length of this problem as

$$l_q = \frac{\gamma}{m}, \quad (7.1.21)$$

which is a factor of γ times the reduced Compton wavelength - a quantum length scale. This case thus corresponds to the extension of the field in the rest frame of the electron being the reduced Compton wavelength.

7.2 Discussion of numerical results

We employed a numerical method like the one used in chapter 6. In essence one performs a numerical calculation of the classical trajectory by solving the classical equations of motion in the given field. Here the field is a constant magnetic field in the region $-L/2 \leq z \leq L/2$ and no field otherwise. Then the integrals of equation (6.2.16) and equation (6.2.17) are evaluated numerically by using the formulas equation (2.2.5) to equation (2.2.7) and equation (6.4.2). This allows one to calculate the intensity distribution using equation (6.2.20) for a given photon energy ω and angle (θ_x, θ_y) . Therefore for each photon energy these integrals must be calculated on an angular grid, and then integrated numerically over this grid to obtain the intensity distribution in photon energy $dI/d\omega$. This grid should be chosen large enough such that essentially all radiation falls within this grid. In equation (7.1.12) the variable of the Bessel function is $\xi = \frac{\omega'R}{3} \left(\frac{1}{\gamma^2} + \theta^2 \right)^{\frac{3}{2}}$, and for large arguments the Bessel function decreases rapidly, thus the typical angle of the radiation is $\theta \lesssim \left(\frac{3}{\omega'R} \right)^{\frac{1}{3}}$. If the deflection is along x as in equation (7.1.1) one can use the total deflection angle in x as a guide for the grid size in the x -direction and $\theta_y \lesssim \left(\frac{3}{\omega'R} \right)^{\frac{1}{3}}$ for the y -direction. By plotting the angular distributions one can determine if a slightly larger grid is necessary.

In figure 7.1.1 and figure 7.1.2 plots of the power spectra calculated using this numerical procedure are shown for $\chi = 0.1$ and $\chi = 10$ for various values of η . In addition I have plotted the usual result of equation (7.1.13) where the field has infinite extension. For large values of η it is seen that the numerical result approaches this spectrum as is expected from the discussion in section 7.1. As η becomes smaller i.e. the field extension L becomes smaller, the power spectrum becomes modified at the low end of the spectrum. Since the formation length becomes longer for low photon energies this effect can be understood in the sense that these will be more susceptible to the finite extension of the field. In the case of $\chi = 0.1$ seen in figure 7.1.1, as η becomes close to and below 1 a transition is observed where the spectrum is radically different. For $\eta = 0.1$ we are at the border of transition from 'case 2' to 'case 1'. For comparison I have plotted equation (7.3.11), which is seen to be in good agreement for the low end of the spectrum. For even smaller values of η this agreement extends to the harder photons as well. In the case of $\chi = 10$ as seen in figure 7.1.2 the spectrum is seen to be modified for larger values of η than the case of $\chi = 0.1$. This is due to the fact that in the quantum regime the first transition is instead from 'case 4' to 'case 3', meaning at $\eta \sim \chi = 10$. Here I have also plotted the result of equation (7.3.11) for comparison, which is seen to be in good agreement.

In these plots a remarkable overall decrease in the power spectrum is seen when $\eta \lesssim 1$. In figure 7.1.3 and figure 7.1.4 I have plotted the total power P as a function of $1/\eta$ for the case of $\chi = 0.1$ and $\chi = 10$, respectively. P_0 is the total power as obtained by equation (7.1.13). For small values of $1/\eta$ the spectrum approaches that of equation (7.1.13), and therefore the total power approaches P_0 . The difference between the classical and quantum case is clear in these two figures. In the classical case the intermediate regime of 'case 2' for $0.1 \leq \eta \leq 1$ shows a decrease in the total power emitted while the case of the intermediate quantum regime of 'case 3' shows an increase in the total power emitted. This maximum in the emitted power is found to be at $\eta = 2\sqrt{2}$ independently of χ for large values of χ . In figure 7.2.1 I show how this maximum emitted power scales with the value of χ . It is found that the numerical calculation agrees very well with the expression

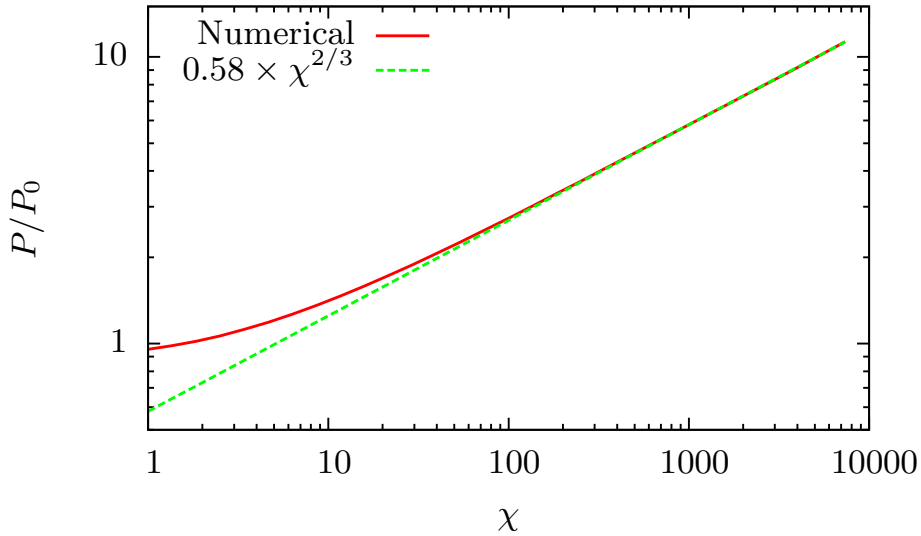


Figure 7.2.1: A plot of the numerical values obtained for the power in the case of $\eta = 2\sqrt{2}$ where the power is at a maximum as function of χ and a plot of an analytical fit valid for large values of χ .

$$\frac{P}{P_0} = 0.58\chi^{\frac{2}{3}} \tag{7.2.1}$$

for large values of χ .

7.3 The spectrum in the limit of a short extension of the field

In section 7.1 and section 7.1 we found that for all photon energies where there should be radiation, the formation length is much larger than the extension of the field, and thus the variation of the phase of equation (7.1.4) was negligible. Thus we can approximate

$$\mathbf{I} = \int_{-\frac{L}{2}}^{\frac{L}{2}} \mathbf{f}(t, \mathbf{n}) e^{ik'x} dt \simeq \int_{-\frac{L}{2}}^{\frac{L}{2}} \mathbf{f}(t, \mathbf{n}) dt.$$

We take the force to act in the x direction and thus only keep terms proportional to \dot{v}_x in equation (2.2.5) and equation (2.2.6). In these terms only the y -component of the velocity enters which is 0 and so we obtain

$$I_x = -g_0 |\Delta \mathbf{v}| \left\{ \theta_y^2 + \left(\frac{1}{2\gamma^2} - \frac{\theta^2}{2} \right) \right\}, \quad (7.3.1)$$

$$I_y = g_0 |\Delta \mathbf{v}| \theta_x \theta_y, \quad (7.3.2)$$

where we have only kept the first order in the transverse velocity change $|\Delta \mathbf{v}|$ and

$$g_0 = \left(\frac{1}{2\gamma^2} + \frac{\theta^2}{2} \right)^{-2}$$

For the J term we thus obtain

$$J = \int \frac{\mathbf{n} \cdot \dot{\mathbf{v}}}{(1 - \mathbf{n} \cdot \mathbf{v})^2} e^{ik'x} dt \simeq g_0 \theta_x |\Delta \mathbf{v}|$$

Then we obtain

$$|\mathbf{I}|^2 = |\Delta \mathbf{v}|^2 g_0^2 \times \left(\theta_y^4 + \frac{1}{4\gamma^4} + \frac{\theta^4}{4} - \frac{\theta^2}{2\gamma^2} + \theta_y^2 \left(\frac{1}{\gamma^2} - \theta^2 \right) + \theta_x^2 \theta_y^2 \right)$$

Performing the integration over φ we obtain

$$\int |\mathbf{I}|^2 d\varphi = |\Delta \mathbf{v}|^2 g_0^2 \frac{\pi}{2} \frac{1}{\gamma^4} (1 + \nu^4) \quad (7.3.3)$$

where $\nu = \gamma\theta$. Inserting g_0 this becomes

$$\int |\mathbf{I}|^2 d\varphi = |\Delta \mathbf{v}|^2 \frac{8\pi\gamma^4}{(1 + \nu^2)^4} (1 + \nu^4) \quad (7.3.4)$$

carrying out the integration $\int \theta d\theta = \frac{1}{\gamma^2} \int \nu d\nu$ we obtain

$$\int |\mathbf{I}|^2 d\Omega = \frac{8\pi}{3} \gamma^2 |\Delta \mathbf{v}|^2 \quad (7.3.5)$$

for the J term we obtain

$$|J|^2 = \frac{16\gamma^8}{(1+\nu^2)^4} \theta_x^2 |\Delta \mathbf{v}|^2 \quad (7.3.6)$$

integrating over φ we obtain

$$\int |J|^2 d\varphi = \frac{16\gamma^8}{(1+\nu^2)^4} \pi \theta^2 |\Delta \mathbf{v}|^2 \quad (7.3.7)$$

and integrating over $\theta d\theta$ we obtain

$$\int |J|^2 d\Omega = \frac{4}{3} \pi \gamma^4 |\Delta \mathbf{v}|^2 \quad (7.3.8)$$

we can therefore write the emitted energy differential in photon energy and angle variable ν by using equation (6.2.20) as

$$\frac{d^2 I}{d\omega d\nu} = \frac{2\alpha}{\pi} \gamma^2 |\Delta \mathbf{v}|^2 \times \left(\frac{\varepsilon'^2 + \varepsilon^2}{2\varepsilon^2} \frac{\nu(1+\nu^4)}{(1+\nu^2)^4} + \frac{\omega^2}{\varepsilon^2} \frac{\nu^3}{(1+\nu^2)^4} \right). \quad (7.3.9)$$

Integrating over ν one obtains the emitted energy differential in photon energy

$$\frac{dI}{d\omega} = \frac{2\alpha}{3\pi} \gamma^2 |\Delta \mathbf{v}|^2 \left(1 - \frac{\omega}{\varepsilon} + \frac{3\omega^2}{4\varepsilon^2} \right). \quad (7.3.10)$$

Formulas equation (7.3.9) and equation (7.3.10) are general for the dipole regime and reduce to the classical formulas as found in e.g. [21] in the limit of $\omega \ll \varepsilon$. Inserting $\Delta v = \frac{eBL}{\varepsilon}$ and dividing by the duration L one obtains the power spectrum differential in photon energy in the case of the 'short' magnetic field as

$$\frac{dP}{d\omega} = \frac{2\alpha}{3\pi\gamma^2} \chi^2 m^2 L \left(1 - \frac{\omega}{\varepsilon} + \frac{3\omega^2}{4\varepsilon^2} \right). \quad (7.3.11)$$

The shape of this spectrum is the same of that of Bethe-Heitler bremsstrahlung in matter and thus in this limit synchrotron radiation becomes 'bremsstrahlung-like'. In addition the power is now proportional to the length L in contrast to the usual synchrotron radiation power which is independent of the duration. Integrating this, one obtains the total power P as

$$P = \frac{\alpha}{2\pi} \frac{\chi^2 m^4 L}{\varepsilon} = \frac{\alpha}{2\pi} \chi \eta m^2 \quad (7.3.12)$$

7.4 Discussion of experimental investigation and relevance in future colliders

From equation (7.1.20) it is seen that if γ is large while χ is small, the length at which this effect becomes important can become long. Consider as an example a 1GeV synchrotron producing visible light of photon energy $\omega = 1\text{eV}$, thus $\chi \sim 10^{-9}$ and the characteristic classical length is $l_c \sim 75\text{cm}$. Thus in the classical case this should be an easily measurable effect under the right circumstances. In the quantum case when χ approaches or becomes larger than 1 it becomes experimentally challenging. In this case the characteristic length of equation (7.1.21) can only be made large by increasing the particle energy. The highest experimentally accessible electron energies are around 285GeV found in secondary beams at the SPS North Area of CERN. At this energy the characteristic quantum length is $0.2\mu\text{m}$. Single crystals of Silicon can be purchased with lengths down to $0.1\mu\text{m}$, and by aligning the incoming beam along the $\langle 110 \rangle$ axis one can obtain $\chi \sim 1$, meaning one is in the quantum regime. At large energies the constant field approximation becomes applicable for the case of channeling radiation in such a crystal, meaning the results presented here are applicable in this case.

In future e^+/e^- colliders such as CLIC, designed for the maximum energy per beam of $\varepsilon = 1.5\text{TeV}$ one achieves a quantum non-linearity parameter of $\chi \sim 10$ [86] and with the current design parameters one has a bunch length of $\sigma_z = 44\mu\text{m}$. In this case $l_q = 1.1\mu\text{m}$. Often bunch shapes are

modeled by a Gaussian distribution and I have numerically calculated spectra in the case when the electron is subject to a Gaussian shaped field pulse of varying length to verify that the effects seen here are not an artefact present only in the case of a constant field with a sharp cutoff. Here the same effects are seen when the typical length scale of the bunch σ_z becomes comparable to the formation length. See e.g. [87] for recent experimental investigations of the significance of the formation length in the case of bremsstrahlung. From figure 7.1.4 and figure 7.1.2 it is seen that in the case of CLIC the effect is small - on the order of 1%. However such design parameters could change during development and thus this effect should be kept in mind.

Chapter 8

Classical and quantum radiation reaction

The calculation of radiation reaction for electrons which will briefly be shown in this chapter has been presented in our arxiv paper [88] and the introductory remarks in this chapter are inspired by this as well.

The Lorentz force equation is central to the theory of classical electrodynamics, allowing to find the motion of a charged particle, given the external electromagnetic field [89]. It is, however, an incomplete picture as it fails to take into account the fact that as a charged particle is accelerated, it radiates which should alter the motion. One approach to this problem is that of the Lorentz-Abraham-Dirac (LAD) equation [90, 91, 92, 89, 93, 94, 95, 96], where an additional damping term proportional to the time derivative of the acceleration is present. This means that the equations of motion become non-Newtonian, i.e. no longer a second order differential equation which leads to problems such as runaway solutions where a charged particle can accelerate exponentially even if there is no external field present [89, 93, 94, 95, 96, 97, 98, 99]. One solution to this problem is a classical perturbation calculation. If the damping term is considered small compared to the Lorentz force, the time derivative of the acceleration is replaced by that of the Lorentz force. This leads to the Landau & Lifshitz (LL) equation of radiation damping, which is once again a second order differential equation. Landau and Lifshitz show that as long as one is within the classical regime of radiation emission, the LL

equation holds.

The rapid progress of laser technology has renewed the interest in the problem of classical radiation reaction and a large number of setups and schemes have been proposed recently to measure classical RR effects in electron-laser interactions [100, 101, 102, 103, 104] (see [98] for previous proposals). However with current technology, RR effects remain small in a laser field and have not yet been experimentally detected. In this chapter we investigate if this can be tested using crystal channeling as a source of the strong field, instead of that from a laser and report on experiments performed in the group NA63 at CERN which have been dedicated to investigating this.

Classical radiation reaction

The description of classical radiation emission discussed in section §2.2 neglects the fact that the emitted radiation carries away energy, when finding the trajectory. This is most easily seen in the case of a constant magnetic field. In this case the trajectory obtained from equation (2.2.3) is an indefinite circular motion where the particle energy is conserved, and yet we know that using equation (2.2.1) for this motion leads to the classical formula of synchrotron radiation. Currently the Landau Lifshitz equation is seen as the solution to this problem. The Landau Lifshitz equation introduces additional terms in the force on a charged particle such that

$$\frac{d\mathbf{p}}{dt} = \mathbf{F} + \mathbf{F}_{LL}. \quad (8.0.1)$$

To get an idea of how \mathbf{F}_{LAD} (Lorentz-Abraham-Dirac force) and subsequently \mathbf{F}_{LL} is obtained let us consider the non-relativistic case. In [89] Jackson starts from the Larmor formula for the instantaneously emitted power

$$P(t) = \frac{2}{3} e^2 (\dot{\mathbf{v}})^2 \quad (8.0.2)$$

and then considers a time integral over the power emitted

$$E_{\text{emit}} = \int_{t_1}^{t_2} \mathbf{F}_{\text{LAD}} \cdot \mathbf{v} dt = - \int_{t_1}^{t_2} \frac{2}{3} e^2 (\dot{\mathbf{v}})^2 dt = \int_{t_1}^{t_2} \frac{2}{3} e^2 \mathbf{v} \cdot \ddot{\mathbf{v}} dt - \frac{2}{3} e^2 (\dot{\mathbf{v}} \cdot \mathbf{v}) \Big|_{t_1}^{t_2}. \quad (8.0.3)$$

Since the last term does not seem to be proportional to the integration interval length (as the emitted energy should be) it must be related to the initial and final conditions and is neglected. One then obtains

$$\int_{t_1}^{t_2} \left(\mathbf{F}_{\text{LAD}} - \frac{2}{3} e^2 \ddot{\mathbf{v}} \right) \cdot \mathbf{v} dt = 0, \quad (8.0.4)$$

and since this should hold for an arbitrary interval we must have

$$\mathbf{F}_{\text{LAD}} = \frac{2}{3} e^2 \ddot{\mathbf{v}}. \quad (8.0.5)$$

Suppose then the external forces vanish in equation (8.0.1) and we are left with

$$m\dot{\mathbf{v}} = \frac{2}{3} e^2 \ddot{\mathbf{v}}, \quad (8.0.6)$$

which has the solution $\dot{\mathbf{v}} = a \cdot \exp(\frac{3m}{2e^2}t)$ where a is an arbitrary constant. This is the problematic runaway solution. To obtain the LL equation as shown in [93], one replaces $\ddot{\mathbf{v}}$ with that obtained from using the Lorentz force

$$m\dot{\mathbf{v}} = q(\mathbf{E} + \mathbf{v} \times \mathbf{B}), \quad (8.0.7)$$

such that

$$\ddot{\mathbf{v}} = \frac{q}{m} \left(\dot{\mathbf{E}} + \dot{\mathbf{v}} \times \mathbf{B} \right), \quad (8.0.8)$$

where the term proportional to \mathbf{v} has been neglected since we are in the non-relativistic limit, and then by replacing $\dot{\mathbf{v}} = \frac{q}{m} \mathbf{E}$ one obtains

$$\mathbf{F}_{\text{LL}} = \frac{2q^3}{3m} \dot{\mathbf{E}} + \frac{2q^4}{3m^2} \mathbf{E} \times \mathbf{B}. \quad (8.0.9)$$

This brings us back to a second order system of differential equations and such runaway solutions are no longer present. The conditions for the

damping force to be small is then found to be that the wavelength of the radiation fulfills

$$\lambda \gg \frac{e^2}{m}, \quad (8.0.10)$$

and that

$$|\mathbf{B}| \ll B_c/\alpha \simeq 137 \cdot B_c. \quad (8.0.11)$$

The condition of equation (8.0.10) is seen to be a factor of α shorter than the Compton wavelength $\lambda_C = 1/m$ and therefore it is seen that the approach would break down much sooner than this due to quantum effects coming into play. The same is seen in equation (8.0.11). The LL equation can therefore be accepted as the classical solution to the problem. The fully relativistic equation can then be found to be [93]

$$\begin{aligned} \mathbf{F}_{\text{LL}} = & \frac{2q^3}{3m} \gamma \left\{ \left(\frac{\partial}{\partial t} + \mathbf{v} \cdot \nabla \right) \mathbf{E} + \mathbf{v} \times \left(\frac{\partial}{\partial t} + \mathbf{v} \cdot \nabla \right) \mathbf{H} \right\} \\ & + \frac{2q^4}{3m^2} \{ \mathbf{E} \times \mathbf{H} + \mathbf{H} \times (\mathbf{H} \times \mathbf{v}) + \mathbf{E}(\mathbf{v} \cdot \mathbf{E}) \} \\ & - \frac{2q^4}{3m^2} \gamma^2 \mathbf{v} \{ (\mathbf{E} + \mathbf{v} \times \mathbf{H})^2 - (\mathbf{E} \cdot \mathbf{v})^2 \} \end{aligned} \quad (8.0.12)$$

In the case of a time-independent electric field as found in a crystal this reduces to

$$\mathbf{F}_{\text{LL}} = \frac{2q^3}{3m} \gamma \{ (\mathbf{v} \cdot \nabla) \mathbf{E} \} + \frac{2q^4}{3m^2} \{ \mathbf{E}(\mathbf{v} \cdot \mathbf{E}) \} - \frac{2q^4}{3m^2} \gamma^2 \mathbf{v} \{ (\mathbf{E})^2 - (\mathbf{E} \cdot \mathbf{v})^2 \}, \quad (8.0.13)$$

where q is the particle charge. The first term in this equation involving the spatial derivative of the electric field is often called the ‘‘Schott’’ or ‘‘derivative’’ term and is of special interest since it is addition to the damping expected from the synchrotron case (the last term). A model is used for the potential, and therefore also for the electric field in a single crystal and based on equation (8.0.13) the radiation spectrum can be calculated numerically using equation (2.2.1), once the motion has been found. In

the 2015 and 2016 experiment, electrons and positrons, respectively were used and the model for the potential used in these cases are different and will therefore be described in their respective sections.

8.0.1 2015 CERN NA63 experiment with 10GeV electrons

For the calculation of the radiation emission of electrons we used an approximation of the potential of a single atomic string in a crystal given by

$$U(x) = V_0 \left[\ln \left(1 + \frac{1}{x + \eta} \right) - \ln \left(1 + \frac{1}{x_0 + \eta} \right) \right], \quad (8.0.14)$$

where $x = \rho^2/a_s^2$, ρ is the radial distance to the center of the string, $a_s = 0.326\text{\AA}$, $x_0 = 5.5$, $\eta = 0.025$ and $V_0 = 29\text{eV}$. This approximation is found in [16].

In figure 8.0.1 such a calculation is shown using the traditional approach of just the Lorentz force, and the result when including the reaction force. Here the effects of multiple scattering and beam divergence are neglected. Before the experiment was conducted the design was based on these results. We have since then made more refined calculations which show that the effect is smaller than seen here, such that seeing the effect of the derivative term would be difficult while the effect of radiation reaction including all terms should be seen.

In May 2015 an experiment was conducted at the CERN SPS H4 beam line to measure the effects seen in figure 8.0.1. The setup used can be seen in figure 8.0.2. S1-S3 are used to generate the trigger signal. A signal should be present in S1&S3 and not in S2 which is a hole scintillator. The electron then passes through the MIMOSA pixel detectors M1 and M2 such that the incoming particle angle can be measured. Afterwards, the electron impinges upon the crystal target where several photons and secondary charged particles are emitted. We are interested in the spectrum of the photons and therefore a large magnet deflects the charged particles away. Several photons then strike the converter foil of $200\mu\text{m}$ Ta (roughly $5\%X_0$) such that only a single photon converts to an electron-positron pair. This pair undergoes multiple scattering within the converter foil, after which their positions are measured in M3 and M4 before they encounter a smaller magnet which deflects the electron and positron. Based on this deflection,

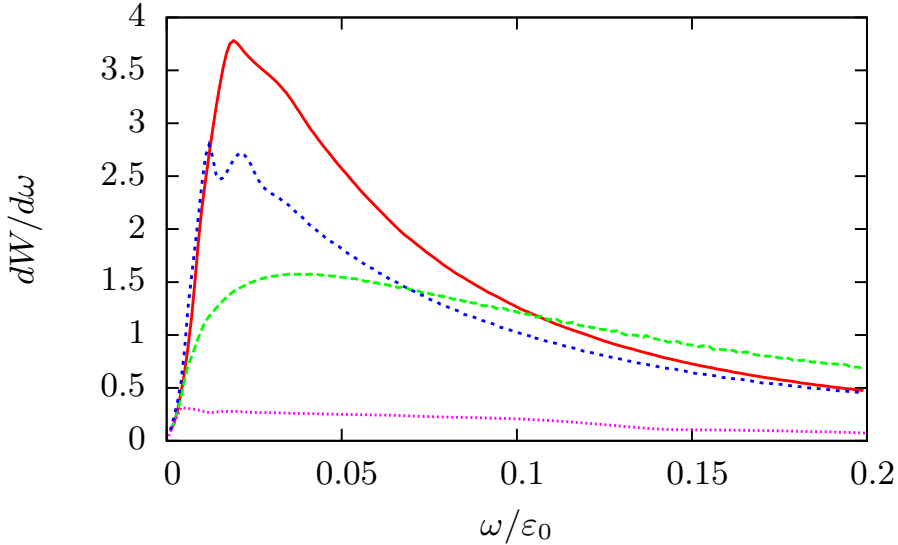


Figure 8.0.1: The differential energy emitted from electrons hitting a 1mm diamond aligned along the $\langle 111 \rangle$ axis. The red curve is the spectrum when radiation reaction is included but the Schott term is neglected. The blue curve includes all terms of the radiation reaction force. The green curve is using just the Lorentz force. The purple curve is the coherent bremsstrahlung emitted from the dechanneled electrons.

the momentum of the positron and electron can be determined, and their sum is the energy of the original photon.

A tracking algorithm has been constructed for the 6 MIMOSA detectors. The ideal event contains one particle trigger, however, if another trigger is received within the time frame window, the window is extended and an event can contain several triggers. The M3 and M4 will be denoted 'arm 1' while M5 and M6 'arm 2' and the first 3 detectors 'arm 3'. Between arm 1 and arm 2 the small dipole magnet is placed, see figure 8.0.2. Hypothetical tracks in each arm are constructed using all possible combinations of hits in each of the two planes. The tracks in arm 2 must be matched with those in arm 1 giving a full particle track. These are identified by the conditions.

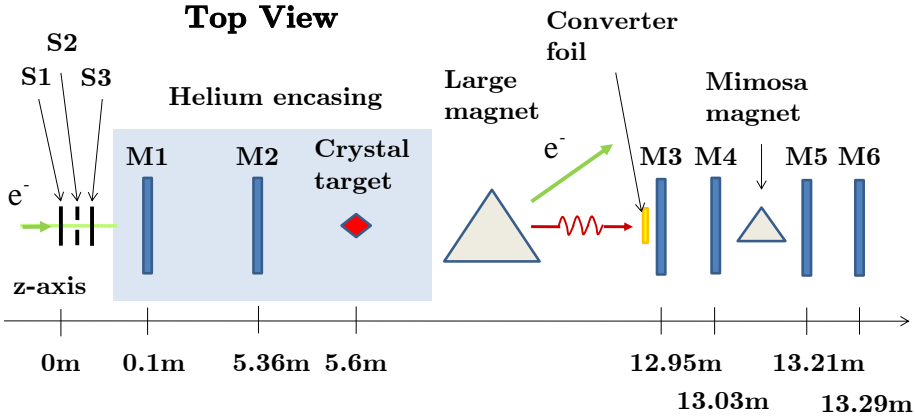


Figure 8.0.2: A schematic of the 2016 experimental setup. The only difference between the setups in 2015 and 2016 is the distance between M1 and M2 which was shorter in 2015.

- 1) The tracks for individual electrons and positrons from each arm must be within a certain distance in the center of the magnet, e.g. $800\mu\text{m}$.
- 2) The size of the deflection angle in the y -direction must be smaller than a certain value, e.g. 2mrad since the magnet deflects in the x -direction.
- 3) The closest approach of the two tracks must happen before a certain z -position, roughly the center of the magnet. A track constructed from one point from particle 1 and another point from particle 2 will have the wrong z -position of closest approach. See figure 8.0.4.

In the ideal event only a single pair is produced from the converter foil. More pairs produced could cause wrong track reconstruction and we therefore select events by

- 4) A single trigger in the event.
- 5) Pairs are identified by requiring that an electron and positron track must originate from within a certain distance in x and y coordinates in the first plane in arm 1, e.g. $20\mu\text{m}$.
- 6) In each event all tracks are found in arm 3 and the track in this arm with the closest approach to the pair origin in arm 1 is chosen. The particle entry angle is then determined from the hits in M1 and M2 of this track. In figure 8.0.3 a photograph of the diamond is seen and a 2d histogram of

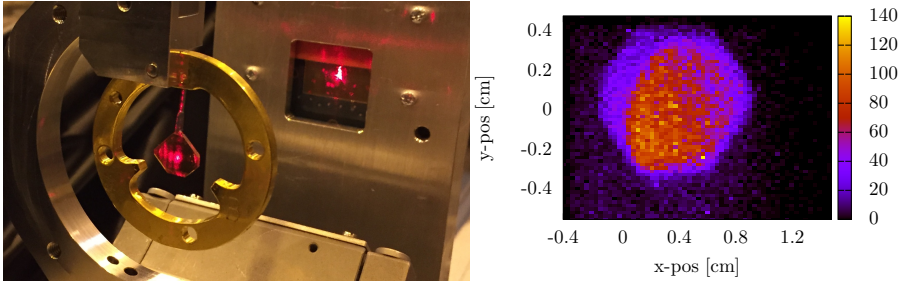


Figure 8.0.3: The 1mm diamond mounted in the experiment (left). The diamond seen using the reconstructed tracks of produced pairs (right). The scintillator hole 'S2' is seen as the orange contour.

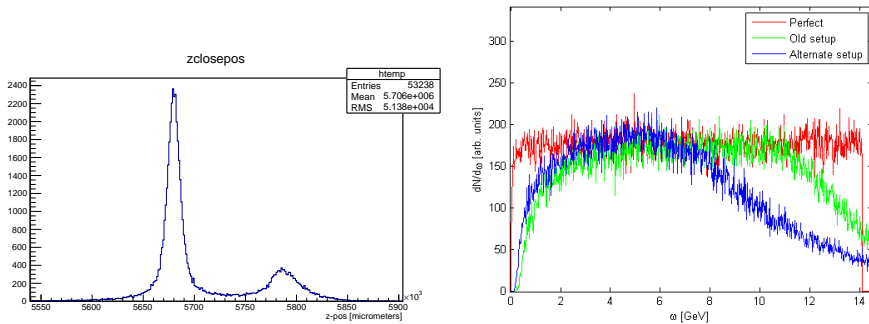


Figure 8.0.4: A histogram of the z -coordinate of closest approach between tracks from 'arm 1' and 'arm 2' (here the positrons). The magnet is placed at 5.86m which is the location of the first peak. The second peak is due to tracks being constructed using hits from different particles and are excluded by a cut of e.g. $zclosepos < 5720e3$.

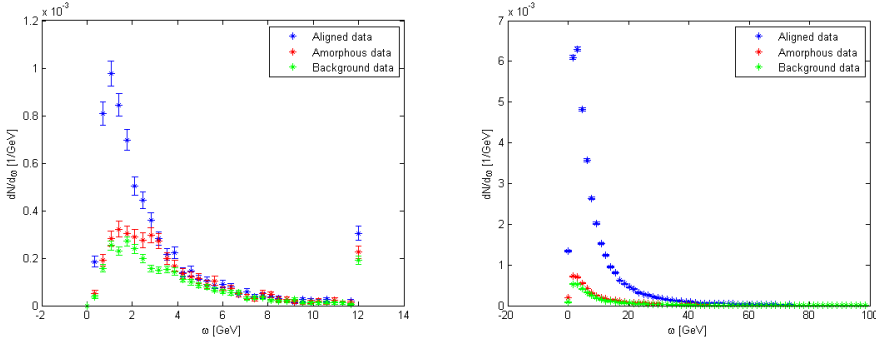


Figure 8.0.5: Measured data on 1mm diamond. With incoming electrons of 10GeV (left) and 100GeV (right). The y -axis is the number of reconstructed photons per event with 1 trigger. The true photon number spectrum is therefore 20 times this due to using a converter foil of thickness $5\% X_0$.

where the pairs originate in the converter foil is seen when the diamond is aligned for incoming 100GeV electrons. Since many high energy photons are generated in the diamond as compared to the background the shape of the diamond can be seen. The orange circular contour is due to the scintillator hole 'S2'. That the diamond is visible outside of the scintillator hole means that often another electron was present within the trigger time window, generating radiation outside of the trigger hole as well.

In figure 8.0.5 we present the reconstructed photon spectra for the case of a 1mm $\langle 100 \rangle$ axially aligned diamond in the cases of 10GeV (left) and 100GeV (right) incoming electrons. We were in principle only interested in the 10GeV measurement, but since the crystal was aligned using 100GeV electrons, a short measurement was carried out at this energy as well, as this could prove helpful in understanding the setup, which turned out to be the case.

In both figures a drop-off is seen below $\sim 1.5\text{GeV}$ which we found were due to the detection efficiency of the setup. As seen in figure 8.0.1 the peak in the power spectrum is located at around 200MeV which is too far below the 1.5GeV cutoff. For the case of 100GeV electrons a higher electron rate was accessible and the radiation becomes harder which was

a better match for this setup, giving us better statistics as seen on the error bars in figure 8.0.5. Typically the 'Enhancement spectrum' is the interesting quantity which is defined as the aligned spectrum subtracted the background spectrum divided by the amorphous spectrum subtracted the background spectrum. For 100GeV electrons this can be seen in figure 8.0.6. The fitting function in this figure is of the type

$$f(\omega) = a \frac{\omega}{b} \int_{\frac{\omega}{b}}^{\infty} K_{5/3}(x) dx + c \quad (8.0.15)$$

where a , b , c are parameters determined by fitting. Performing a fit using the inverse of the size of the error as weights one obtains the fit seen in figure 8.0.6 with parameters $a = 14.5 \pm 2.0$, $b = 17.1\text{GeV} \pm 3.5\text{GeV}$ and $c = 4.9 \pm 1.0$. When the critical angle $\theta_c = \sqrt{\frac{2U_0}{\varepsilon}}$ where $U_0 \sim 100\text{eV}$ is the crystal continuum potential depth and ε the electron energy, becomes larger or comparable to the characteristic radiation angle $1/\gamma$ the constant field approximation becomes applicable i.e. the radiation becomes synchrotron like. The functional form of the classical synchrotron radiation power spectrum is that of equation (8.0.15) which is why this is a good choice for a fitting function in this case. While this was a good measurement it is not sufficient to definitively show the effect of radiation reaction. To do this, a measurement using the same energy but a different thickness crystal is necessary where radiation reaction is negligible and measurements on a 0.5mm crystal was only done for the 10GeV case where detector efficiency was lacking. The spectrum seen in figure 8.0.6 could be compared with a theoretical calculation with and without radiation reaction, but the calculated spectrum has a significant dependence on the beam divergence and the dechanneling length. The measurement on the 'thin' crystal is needed to confirm the used values of beam divergence and dechanneling length in the theoretical calculation, such that the effect of radiation reaction is not confused with e.g. a different beam divergence than expected. The beam divergence is measured experimentally using M1 and M2.

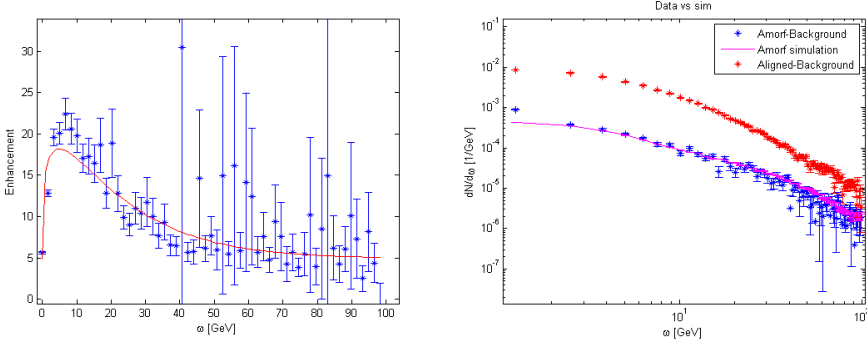


Figure 8.0.6: The 'Enhancement' for the 100GeV case (left). Enhancement is defined as 'Data-Background'/'Amorf-Background' and the shape of this spectrum is not affected by detector efficiency, except for a smearing, and can be compared with theory. A fit has been performed to a function of the same shape as the power spectrum of synchrotron radiation. The number spectrum in the amorphous case has been simulated (right) and compared with experiment.

8.0.2 Simulation of the setup

To test the tracking code and for comparison of experimental data to theoretical calculations, a Monte-Carlo simulation of the experimental setup has been developed. This code takes the theoretically calculated radiation spectrum of a channeled particle as input which is then sampled when an electron is sent through the setup. If a pair is produced in the converter foil, the energy of the electron and positron is selected based on the Bethe-Heitler cross section of pair production in amorphous media. Multiple scattering of the produced particles in the detectors and air between the detectors is simulated using normal distributions and the PDG formula equation (2.1.10). The output of this Monte-Carlo simulation are simulated detector data files which are then sent through the tracking algorithm which is also used for the experimental data. This way potential problems with the tracking algorithm could also be identified. This allows us to go from the theoretically calculated spectrum, see figure 8.0.1, to the spectrum which would be seen in the experiment. In figure 8.0.6 (right) such a simulation has been carried out for the amorphous case of

100GeV electrons and good agreement is observed. A similar agreement is found in the case of 10GeV, although here the uncertainty on the measurement is larger as seen in figure 8.0.5. In figure 8.0.4 (right) the measured photon spectrum has been simulated in the case of a flat input number spectrum from 0-14GeV as seen in the 'Perfect' case. In the 'Alternate setup' the 4 last detectors have had their spacing reduced from 8cm to 2cm which means a better resolution at lower energies, but worse at high energies. 'Old setup' is that used during the 2015 run and which was later also the distance used in the 2016 experiment. The lower drop-off in efficiency is mainly due to multiple Coulomb scattering in the converter foil, or the magnet deflecting particles outside of the acceptance, and the upper drop-off due to the spatial resolution of the MIMOSA detector of $\sigma \simeq 4\mu\text{m}$.

8.1 2016 CERN NA63 180 GeV positrons

Based on the lessons learned during the 2015 experiment, it was necessary to redesign the experiment such that the interesting region in the radiation emission spectrum moved up into the region of good efficiency of the setup. Based on the simulation routine developed after the previous experiment, it was found that it was not possible to move this detection threshold significantly further down. This, along with the fact that positrons have a longer dechanneling length, making this effect less important, meant that the possibility of using high energy positrons was investigated. Since the radiation spectrum from positrons is generally softer than that of electrons, a higher energy of the incoming particle energy was possible while the emitted radiation spectrum stays soft. Since positrons generally radiate less power than electrons, longer crystals were necessary for the radiation reaction effect to come into play which meant a transition from Diamond crystals to Silicon crystals was made.

8.1.1 Theory

In figure 8.1.1 I show the theoretical calculations made for different thicknesses of axial channeling along the $\langle 100 \rangle$ axis in silicon based on equa-

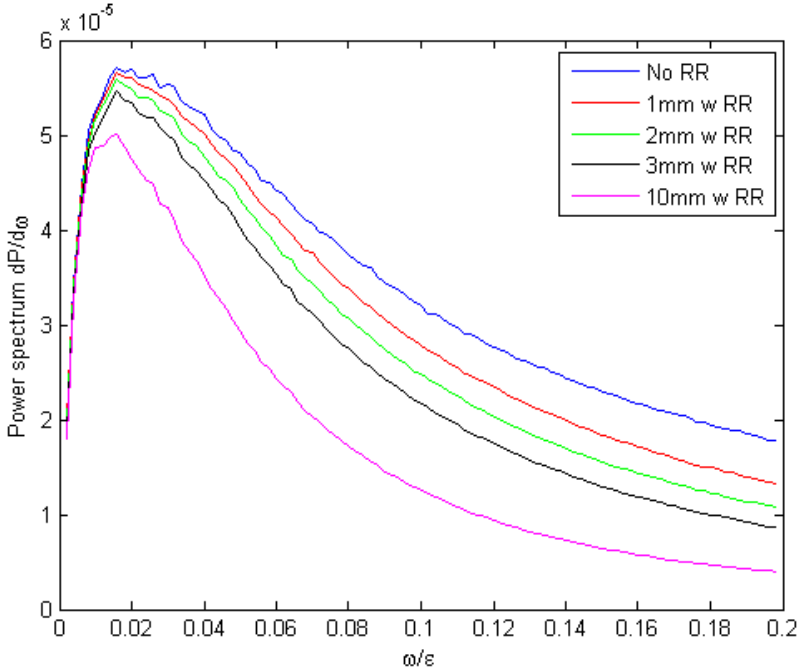


Figure 8.1.1: Theoretical calculations of the power spectra when including the radiation reaction force of the Landau & Lifshitz equation for 180 GeV positrons with no beam divergence entering along the $\langle 100 \rangle$ axis.

tion (8.0.13) and equation (2.2.1). To find the motion of the positrons, the thermally averaged Doyle-Turner potential was used. This is given by

$$U(r_{\perp}) = \frac{e^2}{a_0} \frac{2a_0^2}{d} \sum_{i=1}^4 \frac{a_i}{B_i + \rho^2} \exp\left(-\frac{r_{\perp}^2}{B_i + \rho^2}\right), \quad (8.1.1)$$

where r_{\perp} is the distance to the string, $\rho = 0.075 \text{ \AA}$ is the thermal vibrational amplitude of Si at 300K, $B_i = \frac{b_i}{4\pi^2}$, d is the distance between the atoms in the string, a_0 is the Bohr radius and the parameters a_i and b_i can be found in table 4.1, taken from [39]. The total potential is then the sum of many such strings with different centers based on the crystal in question. For the $\langle 100 \rangle$ orientation, the potential is periodic over the

region where $-\frac{aL}{4} < x < \frac{aL}{4}$ and $-\frac{aL}{4} < y < \frac{aL}{4}$. The potential is therefore always evaluated within this square and by summing over the nearest 41 strings within and surrounding this area. In chapter 6 and chapter 7 it was described how the radiation emission can be determined from the classical trajectory, but which includes quantum effects. In the experiment the beam divergence turned out to have an unexpectedly large effect on the spectrum, making the radiation harder than what was expected from figure 8.1.1. Therefore quantum effects, unintentionally, became important. An approximative approach at calculating the radiation spectrum when including quantum effects, and damping of the motion has been developed and is based on applying a reduction factor on the LL equation of equation (8.0.13). This approach is also investigated in [105, 106]. The time derivative of the energy of a charge is given by $\dot{\epsilon} = \mathbf{F} \cdot \mathbf{v}$ and from equation (8.0.13) it is seen that the last term is parallel to the velocity \mathbf{v} while the others are transverse. Therefore we get

$$\dot{\epsilon} = -\frac{2e^4}{3m^2}\gamma^2 v^2 \left\{ (\mathbf{E})^2 - (\mathbf{E} \cdot \mathbf{v})^2 \right\} \simeq -\frac{2e^4}{3m^2}\gamma^2 \mathbf{E}^2$$

which is the result you would obtain for the radiated power in a constant field. In the quantum case, the constant field case can be studied analytically, and the power is therefore known in this case. We therefore modify the LL equation by multiplying the force with $P_{\text{QED}}(\chi)/P_{\text{classical}}(\chi)$ where χ is evaluated locally. In [16] a useful approximation of $P_{\text{QED}}(\chi)$ can be found, accurate to within 2% for any value of χ , and gives us

$$\frac{P_{\text{QED}}(\chi)}{P_{\text{classical}}(\chi)} = \frac{1}{[1 + 4.8(1 + \chi) \ln(1 + 1.7\chi) + 2.44\chi^2]^{2/3}} \quad (8.1.2)$$

In addition we must reconsider the formulas for radiation emission stated in chapter 6 which can be written as

$$\frac{d^2 I}{d\omega d\Omega} = \frac{e^2}{4\pi^2} \left(\frac{\epsilon'^2 + \epsilon^2}{2\epsilon^2} \left| \int_{-\infty}^{\infty} \mathbf{f}(t, \mathbf{n}) e^{ik'x} dt \right|^2 + \frac{\omega^2 m^2}{2\epsilon^4} \left| \int_{-\infty}^{\infty} \frac{\mathbf{n} \cdot \dot{\mathbf{v}}}{(1 - \mathbf{n} \cdot \mathbf{v})^2} e^{ik'x} dt \right|^2 \right). \quad (8.1.3)$$

When damping is present, ϵ is no longer a constant but a time dependent quantity, which raises the question of how equation (8.1.3) should be used.

I posit that as long as $\varepsilon(t)$ varies slowly over the formation length, $\varepsilon l_f / \varepsilon \ll 1$ (see chapter 7) the factors involving the energy can be taken inside of the integration and then be time dependent. This approach is denoted 'damping' in figure 8.1.2. It should be emphasized that this approach is not rigorously correct.

If χ is small, the radiation emission occurs by emission of many low energy photons while in the quantum case, emission happens by fewer emissions of larger energy. The latter case meaning that the stochastic nature of the process becomes prominent. Quantum radiation reaction has been investigated recently in [105, 107, 108] but there the constant field approximation is employed, i.e. $\eta \gg 1$ where

$$\eta = \frac{p_{\perp, \max}}{\sqrt{2}m}. \quad (8.1.4)$$

For the case at hand, we will encounter values of $0.5 \lesssim \eta \lesssim 5$. Therefore only some particles are in the regime of $\eta \gg 1$ and using the constant field approximation would not be accurate for the particles with low values of η . I therefore employ a different and more general approach where the length of the crystal is divided into a number of sections, 100 for the 1cm case and 40 for the 3.8mm case. The radiation emission is then calculated numerically using equation (6.2.20) in the first section from which the total probability of emission above a certain cutoff can be calculated.

This lower cutoff must be chosen such that it is below where the power spectrum starts to go towards 0, see figure 8.1.2, such that the emitted energy below the cutoff is negligible. Based on this calculated probability of emission, given by the integral over ω and Ω in equation (6.2.20), I decide by using a Monte-Carlo approach if emission happens or not. If emission does not happen, the trajectory in the next section is calculated by using the final coordinates in the previous section as the initial conditions. If emission does happen, a Monte-Carlo approach is used to sample the angular integrated spectrum to find a photon energy ω of emission and then another Monte-Carlo approach to sample the angular distribution of emission for this ω . The momentum of the emitted photon is then known, and the initial conditions for the next sections is then found from 4-momentum conservation at the end of the previous section. This process is then repeated in every section. The final radiation spectrum is then the sum over that from each of these sections. One must consider carefully

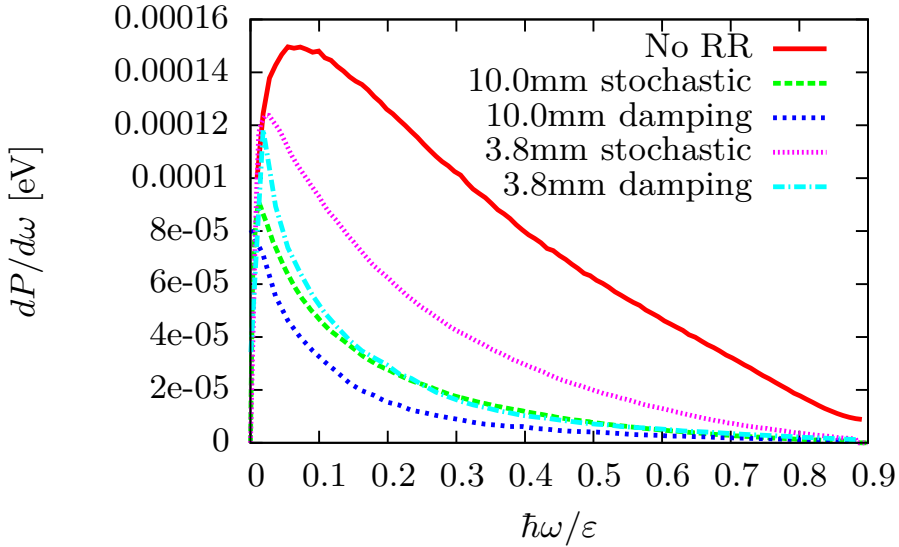


Figure 8.1.2: Here I show the theoretical power spectra in the case of no kind of radiation reaction 'No RR' and for the stochastic and damping approaches described in the text.

what the length of each section should be. It should be so short that the average energy emitted over this length is small compared to the particle energy i.e. the calculated probability of emission above the previously mentioned cut-off should be smaller than 1. At the same time the length of the section must be significantly longer than the formation length of the radiation, otherwise the interference from radiation emitted at different parts of the trajectory will not be taken into account properly.

In the case studied here we will encounter values of χ up to 1.44 such that quantum effects are important. This is also clear from looking at the 'No RR' case in figure 8.1.2 which shows that the radiation without radiation reaction is hard. In this figure the experimentally measured values of $\sigma_x = 44.4\mu\text{rad}$ and $\sigma_y = 67.0\mu\text{rad}$ in the initial entry angle is included and the difference compared to no beam divergence as seen in figure 8.1.1 is

large. The dechanneling length for positive particles is given by

$$L_D^+ = \frac{256}{9\pi^2} \frac{pv}{\ln(2m\gamma/I) - 1} \frac{a_{\text{TF}}d_p}{r_e m},$$

[40] where $I \simeq 172\text{eV}$ is the ionization potential for Si and d_p is the interplanar distance. For the (110) plane and high energy positrons this is approximately $L_D^{(110)} \simeq 0.63 \frac{\text{mm}}{\text{GeV}} \cdot \varepsilon$. This is the planar case, and a simple estimate based on this can be made in the axial case. As dechanneling is caused by multiple scattering heating the transverse motion, the dechanneling length is proportional to the potential energy depth, and therefore we can estimate the dechanneling length in the axial case by multiplying the above formula by the ratio of the potential depths in the axial vs. planar case. Using the values of the potential depth as found in [16] we estimate the axial dechanneling length along the $\langle 111 \rangle$ axis of Si as $L_D^{\langle 111 \rangle} \simeq 2.9 \frac{\text{mm}}{\text{GeV}} \cdot \varepsilon$, which in the case of 180GeV gives 52.2cm, meaning dechanneling can be neglected when the thickest crystal is 1cm.

In figure 8.1.3 I have used the results of the calculations shown in figure 8.1.1 in the procedure to simulate the experimental setup. The results in this figure should therefore resemble what will be seen in the experiment. The calculations seen in figure 8.1.1 and figure 8.1.3 were done before the experiment and the design and measurement times were based on these. New calculations were needed to include the beam divergence which will be shown in section 8.1.2.

8.1.2 Experiment

In this experiment we used an almost identical setup compared to the year before, as seen in figure 8.0.2, the only change being the first two MIMOSA detectors having an increased spacing to match the higher incoming energy.

When time came for the experiment, a delay on cutting the $\langle 100 \rangle$ crystals for which the measurements were planned, meant that I could only start with $\langle 111 \rangle$ crystals of thickness 3.8mm and 1cm. During the experiment the $\langle 100 \rangle$ crystals started to arrive, but unfortunately after having measured on the $\langle 111 \rangle$ crystals and the newly arrived 1cm $\langle 100 \rangle$ crystal, accident struck and a fire in a power supply on the PS meant we lost the remaining 5 days of planned beam time. We therefore intend to redo

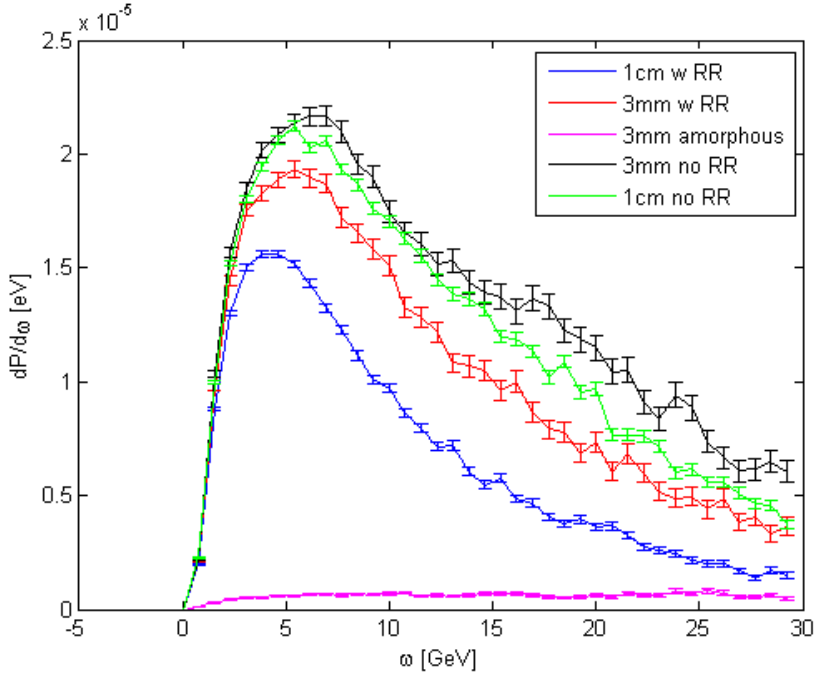


Figure 8.1.3: In this figure, the theoretical spectra have been used in a simulation of the setup. Here the the difference made by the inclusion of the RR force is seen between the cases of 3mm vs. 10mm crystal thickness.

the experiment in 2017 such that we have measurements for 4 (or more) crystal thicknesses of the same orientation while in the classical regime of radiation reaction such that the LL is fully applicable.

In figure 8.1.4 I show the experimentally obtained power spectrum for the two $\langle 111 \rangle$ crystals along with some new simulations that were done after the experiment as opposed to those in figure 8.1.3 which were done before the experiment, and were the basis for the design of the experiment. These new simulations were for the $\langle 111 \rangle$ axis instead, and now including the experimentally measured beam divergence. The simulation results shown in this figure are for the 'stochastic' approach as described in section §4.1. In figure 8.1.5 I show the experimentally obtained enhancement spectra

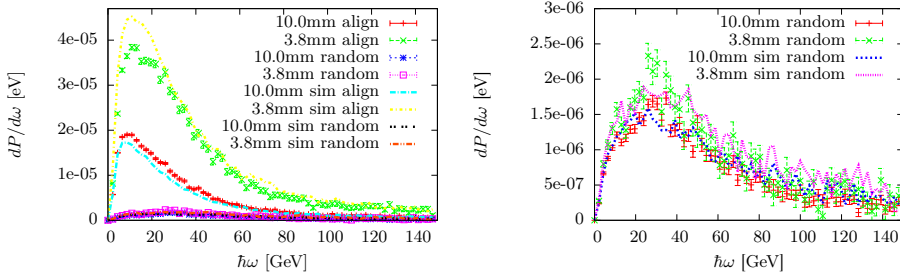


Figure 8.1.4: (Left) The power spectra obtained from the experiment on the $\langle 111 \rangle$ crystals with curves from simulation for comparison. (Right) A zoom on the amorphous curves.

and compare to simulations using both the 'stochastic' and 'damping' approach. In the analysis after the experiment it was discovered that the beam divergence had an unexpectedly large effect on the shape of the spectrum which is shown in figure 8.1.7. The effect of the beam divergence is to make the radiation harder, whereby a purely classical calculation is no longer adequate which is the reason for the development of the procedure described in equation (8.1.3). In figure 8.1.6 the number spectra are shown for the two thicknesses of $\langle 111 \rangle$ crystals. In the absence of RR effects, the counting spectrum of the 1cm crystal should be 1cm/3.8mm times that of the 3.8mm crystal. During the experiment we were surprised that the two counting spectra for large photon energies seem to approach each other. This was not seen in the calculations done before the experiment and the concern that a saturation effect in the experimental setup was causing this prompted us to switch from the 200 μm Ta foil to one of a thickness of 42.5 μm , meaning a reduction from a roughly 5% X_0 foil to roughly 1% X_0 . This was done when switching from the $\langle 111 \rangle$ crystals to the $\langle 100 \rangle$ crystal. The results from the 1cm $\langle 100 \rangle$ crystal with the 'thin' foil are seen in figure 8.1.8.

The results of the simulation are normalized by a constant factor such that the result in the amorphous case matches as best as possible with the experimental, see figure 8.1.4. This normalization factor is between 0.82 and 0.96 in the results presented here.

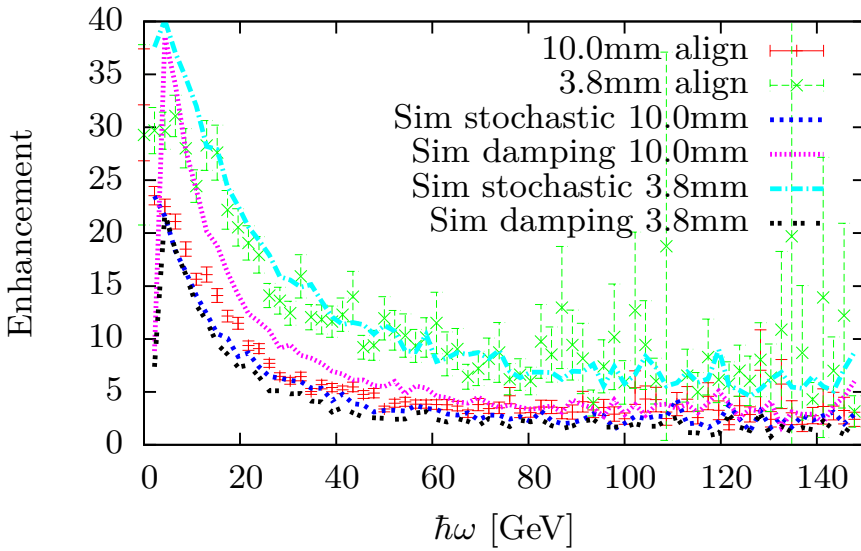


Figure 8.1.5: The enhancement spectra compared to the two theoretical approaches of 'damping' and 'stochastic'.

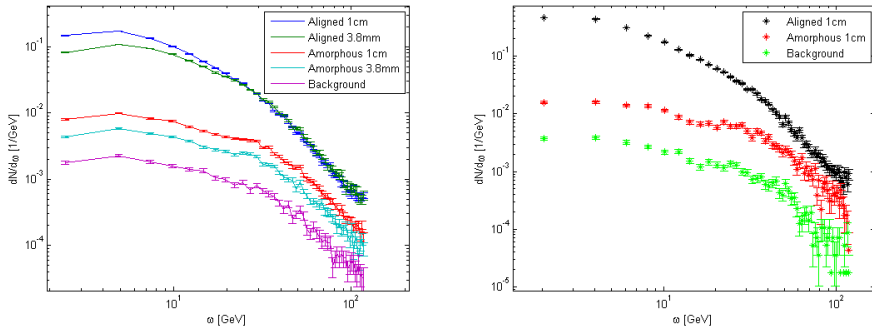


Figure 8.1.6: (Left) A figure showing the number spectra for the two $\langle 111 \rangle$ crystals and the $\langle 100 \rangle$ 1cm crystal (right).

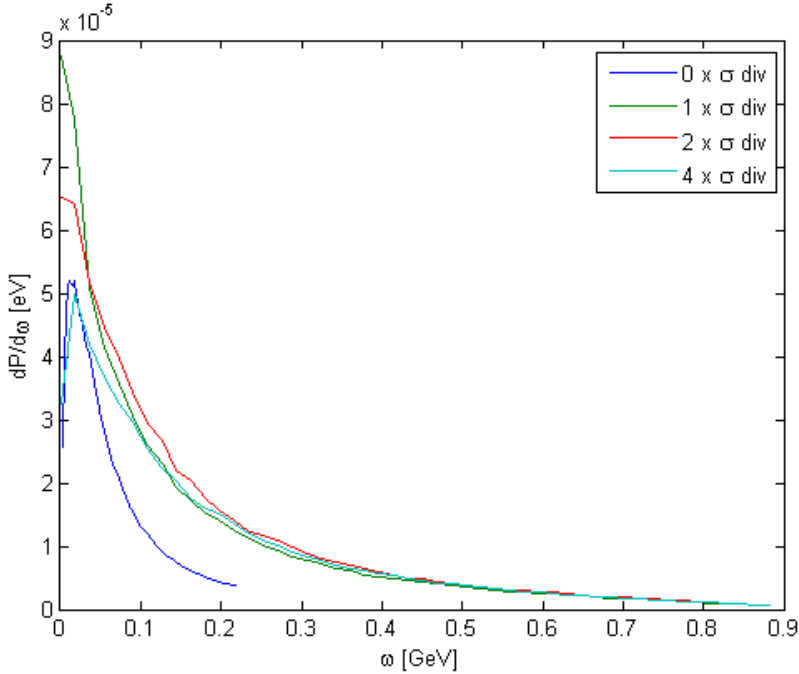


Figure 8.1.7: A figure showing the power spectrum for different factors of the experimentally measured beam divergence using the the approach described in connection to equation (8.1.3).

8.1.3 Deconvoluting the experimental data

In e.g. figure 8.1.4 and figure 8.1.8 I have shown the experimentally obtained power spectra, but these are not directly comparable to the theoretical calculations which is easily seen in the amorphous case in figure 8.1.4 which from theory is expected to be roughly a constant, see equation (2.2.10). This is the case since the detection efficiency is energy dependent, and in addition there is an energy dependent broadening i.e. if a monochromatic source of photons entered the detector, an approximately Gaussian distribution of photon energies around the actual value would be observed - and the width of this Gaussian depends on the photon energy of the monochromatic source. Because of this, one cannot simply

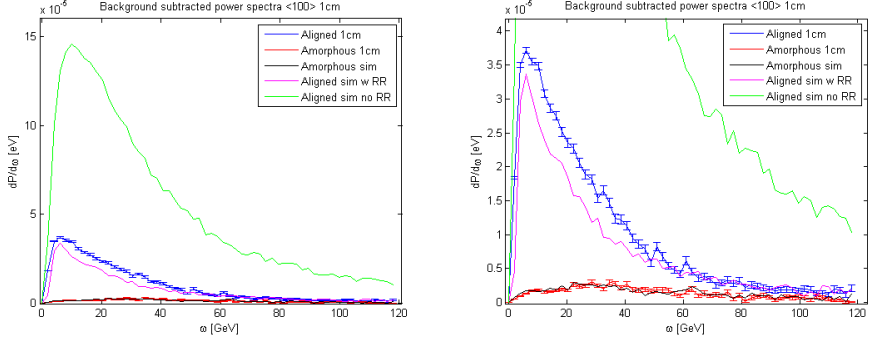


Figure 8.1.8: In this figure I show the experimentally obtained power spectra for the 1cm $\langle 100 \rangle$ crystal compared to simulations with and without the damping of the LL equation. (Right) figure is a zoom of the (left).

find the efficiency by comparing the experimental spectrum in the amorphous case, to the theoretical one and then apply this efficiency to the aligned case. What must be done is to suggest a trial emission spectrum from the crystal, send it through the routine that simulates the experimental response to this, and compare this result with the experimental results. For this I have employed a model which is a linear combination of two of the functions describing the quantum synchrotron radiation as seen in equation (7.1.13) which will now be denoted as $f(\omega, \chi)$

$$\frac{dP}{d\omega}(\omega) = \frac{a}{\chi_1} \cdot f(\omega, \chi_1) + \frac{b}{\chi_2} \cdot f(\omega, \chi_2). \quad (8.1.5)$$

This results in 4 free parameters. To find these parameters, an initial guess was made, then a simulation of the setup with such an emission spectrum was carried out and an efficiency function given by simply the ratio of the simulated result to the trial function was made. A function of the type equation (8.1.5) multiplied by this efficiency was then fitted to the experimental results to obtain new values of these 4 parameters. From these new parameters a new simulation was carried out and the procedure repeated. After a few iterations convergence is achieved.

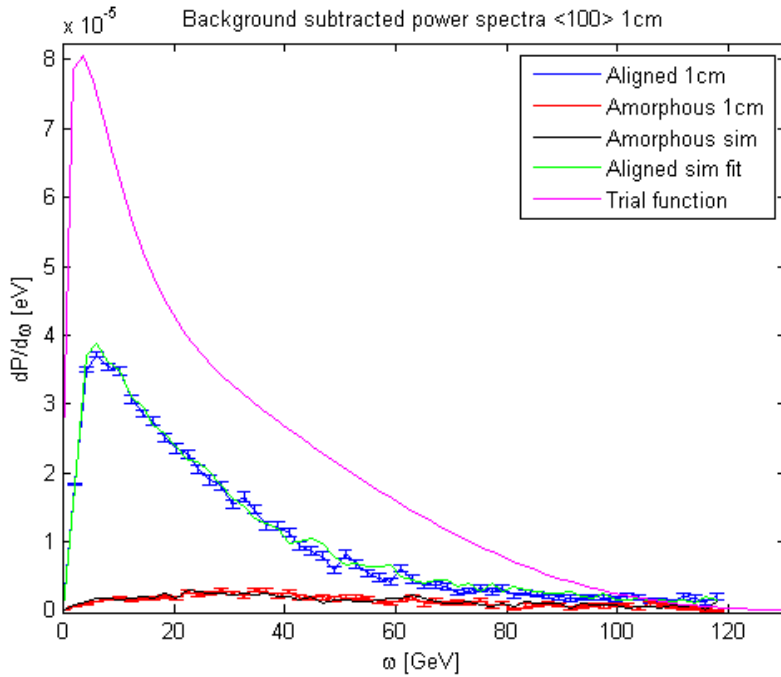


Figure 8.1.9: In this figure the experimental power spectrum for the $\langle 100 \rangle$ 1cm crystal is seen again with the trial function producing the best agreement when the experiment is simulated using this radiation emission spectrum.

In figure 8.1.9 it is seen how this procedure can produce results which agree very well with the experiment.

In table 8.1 I show the parameters obtained. This provides a simple way for external groups to compare theoretical results with our experimental results, without having to simulate the experimental setup as I have done. For the $\langle 111 \rangle$ crystals a similar agreement as that seen in figure 8.1.9 is seen.

In figure 8.1.10 it is seen that the theoretical calculations with and without RR are almost identical for the $\langle 100 \rangle$ and $\langle 111 \rangle$ axis. It is also seen that the experimentally obtained results for the 1cm case in $\langle 100 \rangle$ and $\langle 111 \rangle$

Case	a	b	χ_1	χ_2
$\langle 111 \rangle$ 3.8mm	0.0335	0.0133	0.2710	0.0247
$\langle 111 \rangle$ 1.0cm	0.0165	0.0169	0.2371	0.0258
$\langle 100 \rangle$ 1.0cm	0.0171	0.0172	0.2134	0.0223

Table 8.1: A table of the parameters of the trial functions giving the best agreement with experimental data.

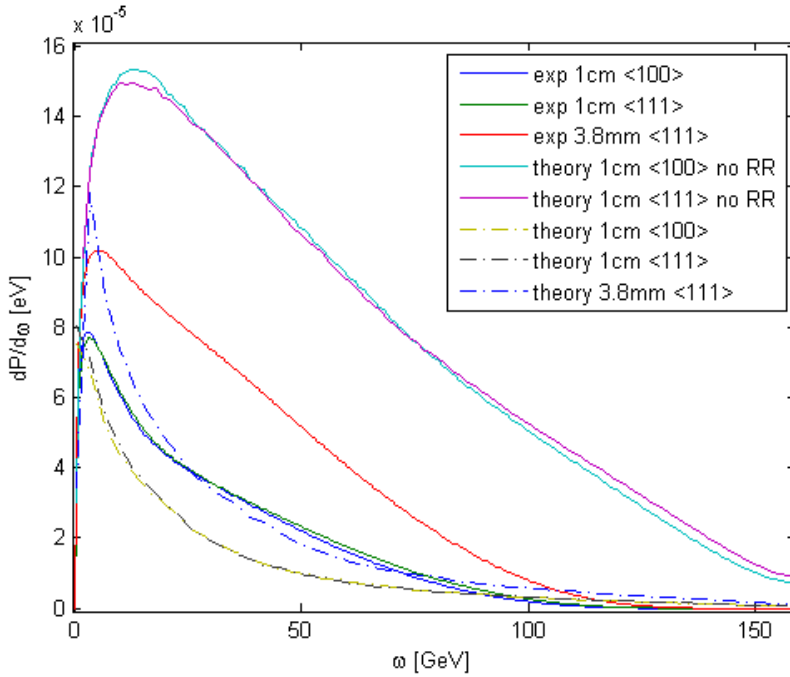


Figure 8.1.10: A comparison of the reconstructed emission spectra from the experimental data, compared to the theoretical results in the 'damping' approach and without radiation reaction.

are almost identical which is also expected from figure 8.1.10, but which also suggests that even though it was a worry during the experiment, no saturation effect due to a high rate is present.

8.2 MIMOSA detectors and data analysis routines

The MIMOSA detectors are CMOS-based position sensitive detectors with 1152 columns of 576 pixels, $\sim 18.4\mu\text{m}$ pitch and represent about $50\mu\text{m}$ Si of material in the beam ($\sim 0.05\%$ of the radiation length). Using a setup as the one sketched in figure 8.0.2 the hit positions of the incoming and produced electrons/positrons can be measured on an event-basis. The raw data format consists of a series of events, and in each event is a series of hits - the (x, y) pixel coordinates where a particle hit the detector and in which of the detectors this hit was registered, also denoted the “plane number” (see figure 8.2.1 for a histogram of hits). From these hits we wish to build tracks, i.e. finding the trajectory of the particles causing these hits. This way we can measure both the angular and momentum distribution of the produced particles. The development of such a tracking algorithm was eased by getting data with 2.5GeV electrons from a setup running 6 MIMOSA detectors at DESY in which I participated in June, 2013. The setup here consisted of 2 sets of 3 detectors and the possibility of putting a device in between where we placed a permanent dipole magnet, in order to measure the momentum of the electron beam. This data-set allowed us to develop functioning tracking algorithms which could subsequently be used for our own MIMOSA detectors as shown at a test run at ASTRID, November 2013 with an electron energy of 580MeV, using the 4 available detectors without a magnet.

To obtain as high precision as possible, one must first do a data-taking run with no magnet, in order to establish how the detectors are aligned with each other. This is the so-called “alignment run”. Here we know that the electrons follow straight trajectories, and we can therefore figure out how the coordinates of the hits in each detector must be transformed. We choose the coordinates in the first plane to be unchanged, and transform the coordinates in the rest of the planes. This is an iterative process. For each event and for each hit in the plane 1, one checks if a hit is present

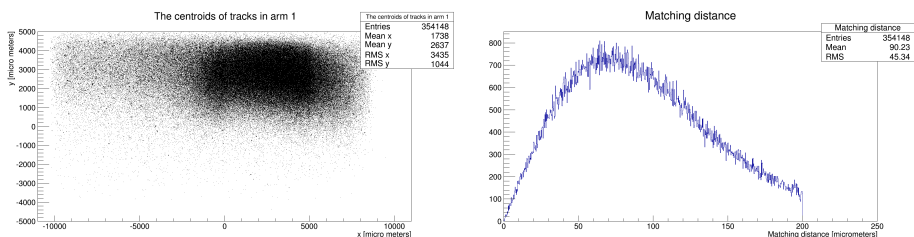


Figure 8.2.1: (Left) A histogram of the (x,y) hit positions of electrons for which a track could be found for the detector test at ASTRID, November 2013. (Right) A histogram of the matching distance between the two sets of 2 planes used in the ASTRID test run. The matching tolerance was set to $200\mu\text{m}$.

in plane j within some small circle, for instance $r = 2\text{mm}$, for the first iteration, of the hit in plane 1. If this is the case the hit coordinate in plane j are stored in a matrix X of the form

$$X = \begin{pmatrix} x_1 & y_1 & 1 \\ x_2 & y_2 & 1 \\ \dots & \dots & \dots \end{pmatrix} \quad (8.2.1)$$

And the expected coordinates (the ones in plane 1) are stored in a matrix of the form

$$X' = \begin{pmatrix} x'_1 & y'_1 & 1 \\ x'_2 & y'_2 & 1 \\ \dots & \dots & \dots \end{pmatrix} \quad (8.2.2)$$

I then seek the matrix A which transforms according to

$$\begin{pmatrix} x' \\ y' \\ 1 \end{pmatrix} = A \begin{pmatrix} x \\ y \\ 1 \end{pmatrix} \quad (8.2.3)$$

This is an affine transformation between coordinates (x, y) and (x', y') , meaning a translation and a linear transformation. All the hits in the matrices X and X' turns this into an overdetermined matrix system, which is solved according to

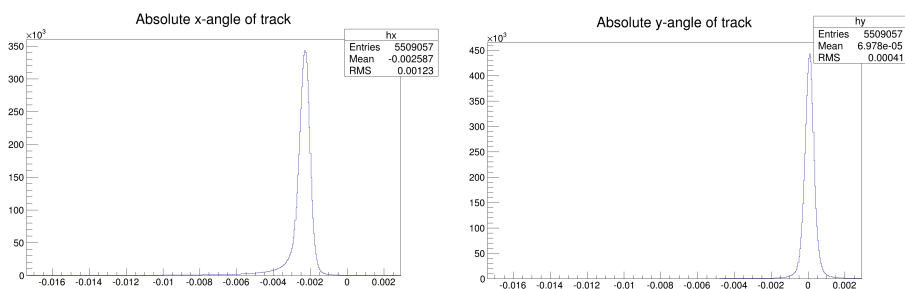


Figure 8.2.2: Histograms of the deflection angles (radians) in the x- and y-directions for the DESY data. The magnet is oriented such that it deflects in the x-direction.

$$A = X^T X (X^T X)^{-1} \quad (8.2.4)$$

This transformation is applied to the coordinates of plane j , and the procedure can be run again with a decreased value of r and for all planes, decreasing the number of false identifications of tracks due to noise. This approach assumed that the tracks were orthogonal to the first detector-plane which is not necessarily true. Therefore an alignment process where one aligns a third plane according to the two previous planes is carried out. For each hit in the first plane and for each hit in the second plane, it is checked if there is a hit within some small circle of radius r in the third plane, and as before the coordinates of the third plane are transformed based on the actual coordinates vs. those expected from the first two planes - this is how the tracks are found in 3 planes.

Chapter 9

Modification of particle production cross sections in strong fields

This chapter serves mostly as an outlook towards a new research project which I plan to undertake after my Ph.D.

It is well known that the presence of the strong field present during bunch collisions in ILC or CLIC should produce abundant radiation emission, the so-called 'beamstrahlung' as discussed in chapter 7, but the effect of this field on the particle production cross section itself is (to the best of my knowledge) unknown. This would be an interesting and potentially very important effect. The main reason this has not yet been studied is due to these processes requiring 2. order perturbation theory in the Volkov states. The process of beamstrahlung or strong field pair production are calculated from 1st order transitions between Volkov states or the Baier, Katkov & Strakhovenko semi-classical operator method which is also based on 1. order perturbation theory as seen in chapter 2. Now, however, 2nd order transitions between Volkov states have been studied, such as double Compton scattering [109, 110] and studies of electron/positron annihilation s-channel processes in a monochromatic laser background field, allowing to calculate e.g. the Higgs-strahlung cross section [111, 112]. I found these papers very interesting and while the strong field in this paper is that of a monochromatic plane wave as obtained from a laser, this calcu-

lation serves as an educational introduction to solving this problem. The 'only' difference is that the external field should be replaced by something that can represent that from the electron/positron bunch. An important question in these problems is if the results obtained from the quantum calculation as presented in e.g. [112] are any different from the results obtained using simple classical laser pre-acceleration and the usual production cross-section. The paper [112] already addresses this issue and finds that there is a significant difference. In this chapter I will try to address this issue in a bit greater detail. One could imagine that when many photon quanta from the external field are involved in the process, the classical picture would hold. Therefore I found a scheme to replace the discrete summation over number of quanta with an integration. This makes it possible to avoid an otherwise very large and numerically heavy summation. Besides this the calculation presented here is initially in many respects the same as that in [112], but in the end I choose to express the production cross section as a differential in the Higgs particle emission angle θ instead of the energy P_H^0 as in [112]. This allows me to find simple equations for the production thresholds for each harmonic of photon emission/absorption and for the total production threshold (corresponding to the highest contributing harmonic), which are not found in [112]. It is then found that the classical and quantum predictions for the cross section differ, even in the value of the production threshold.

9.1 Theory

The wave function of an electron in an electromagnetic field characterized by a vector potential $A^\mu(\varphi)$ with $\varphi = kx$, $k^\mu = (\omega, \mathbf{k})$ and $x = (t, \mathbf{x})$ is given by [111, 112]

$$\psi_{e^-} = N_p \left(1 - \frac{e\mathbf{k}\cdot\mathbf{A}}{2kp_-} \right) u e^{iS_-} \quad (9.1.1)$$

where p_- is the electron 4-momentum, u the free Dirac electron bispinor, N_p is a normalization constant to be determined, and

$$S_- = -p_-x + \frac{e}{kp_-} \int^\varphi d\varphi' \left[p_-A(\varphi') + \frac{e}{2}A^2(\varphi') \right]. \quad (9.1.2)$$

This is the so-called Volkov state. The positron state is obtained by replacing $p_- \rightarrow -p_+$ and $u \rightarrow v$ where v is the free Dirac positron bispinor. We therefore consider a monochromatic plane wave and define

$$A^\mu = a^\mu \cos \varphi \quad (9.1.3)$$

To find the normalization constant N_p we consider the current [112]

$$\begin{aligned} j^\mu &= \bar{\psi}_{e^-} \gamma^\mu \psi_{e^-} \\ &= 2|N_p|^2 \left(p^\mu + eA^\mu - e \left[\frac{pA}{kp} + \frac{eA^2}{2kp} \right] k^\mu \right). \end{aligned} \quad (9.1.4)$$

The time averaged current in the case of equation (9.1.3) then becomes

$$\bar{j}^\mu = 2|N_p|^2 \left(p^\mu - \frac{e^2 a^2}{4kp} k^\mu \right) = 2|N_p|^2 q^\mu. \quad (9.1.5)$$

We then normalize according to $\bar{j}^0 = \frac{1}{V}$ and therefore obtain $N_p = 1/\sqrt{2Vq^0}$ where we have defined

$$q^\mu = p^\mu - \frac{e^2 a^2}{4kp} k^\mu \quad (9.1.6)$$

Using equation (9.1.3) in equation (9.1.2) we obtain

$$S^- = -q_- x + \frac{e}{kp_-} \left[p_- a \sin \varphi - \frac{ea^2}{8} \sin 2\varphi \right] \quad (9.1.7)$$

when the field is present. The \mathcal{S} matrix element is given by [111], [112]

$$\begin{aligned} \mathcal{S} &= -\frac{ig}{2 \cos \theta_W} \iint d^4x d^4y \bar{\psi}_{e^+}(x) \gamma^\mu (g_V - g_A \gamma^5) \\ &\quad \times \psi_{e^-}(x) \mathcal{D}_{\mu\nu}(x-y) \frac{igM_Z}{\cos \theta_W} \frac{1}{\sqrt{2E_H V \cdot 2E_Z V}} \epsilon_Z^{*\nu} e^{i(P_Z + P_H)y} \end{aligned} \quad (9.1.8)$$

where ψ_{e^-} and ψ_{e^+} are the electron and positron wave functions respectively, θ_W is the Weinberg angle, $g = e/\sin \theta_W$, g_V and g_A are the leptonic

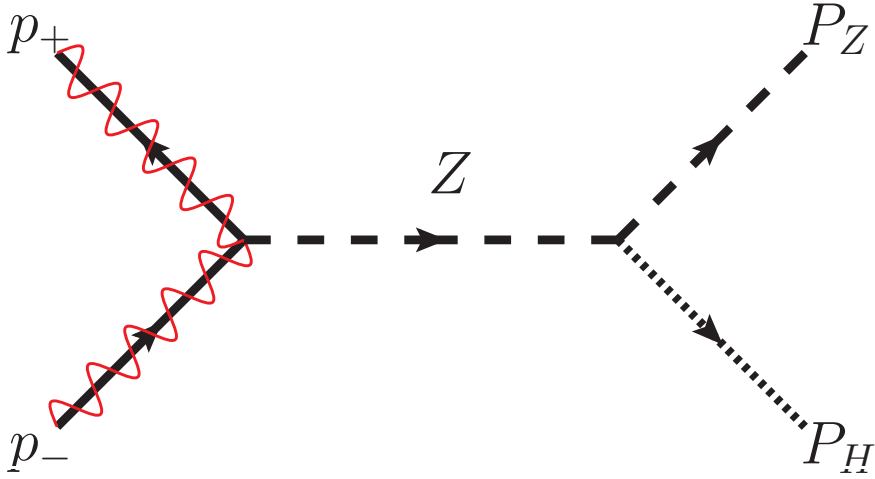


Figure 9.1.1: A Feynman diagram depicting the process corresponding to equation (9.1.8). The incoming electron and positron of momentum p_- and p_+ in the background field fuse to a virtual Z -boson which decays to a real Z -boson and a Higgs-boson.

weak neutral coupling constants, M_Z the mass of the Z -boson, P_H and P_Z the 4-momentum of the Higgs- and Z -boson respectively, ϵ_Z^ν is the Z -boson polarization vector and $\mathcal{D}_{\mu\nu}$ is the Z -boson propagator given by

$$\mathcal{D}_{\mu\nu}(x-y) = -4\pi i \int \frac{d^4 q}{(2\pi)^4} e^{iq(x-y)} \frac{g_{\mu\nu} - \frac{q_\mu q_\nu}{M_Z^2}}{q^2 - M_Z^2}. \quad (9.1.9)$$

See figure 9.1.1 for a Feynman diagram depicting this process. The goal of the calculation is to obtain the interaction cross section given by

$$d^6\sigma = \frac{1}{4} \sum_{\text{spins}} \frac{|\mathcal{S}|^2}{\tau|j|} \frac{V d^3 P_H}{(2\pi)^3} \frac{V d^3 P_Z}{(2\pi)^3}, \quad (9.1.10)$$

where τ is an interaction time and $|j|$ is the particle flux given by v_{rel}/V where v_{rel} is the relative velocity of the colliding particle beams. The summation is to be performed over the electron/positron spins and the Z -boson polarization.

We will first consider the parts of equation (9.1.8) involving the x-coordinate:

$$\int d^4 x \bar{v}_+ \left(1 + \frac{e\phi k \cos \varphi}{2kp_+} \right) e^{-i \left(q_+ x + \frac{e}{kp_+} \left[p_+ a \sin \varphi + \frac{ea^2}{8} \sin 2\varphi \right] \right)} \\ \times \gamma^\mu (g_V - g_A \gamma^5) e^{iqx} \\ \times \left(1 - \frac{e k \phi \cos \varphi}{2kp_-} \right) u_- e^{i \left(-q_- x + \frac{e}{kp_-} \left[p_- a \sin \varphi - \frac{ea^2}{8} \sin 2\varphi \right] \right)}, \quad (9.1.11)$$

which can be rewritten

$$J_x^\mu = \int d^4 x \bar{v} \left(\gamma^\mu (g_V - g_A \gamma^5) + B^\mu \cos \varphi + C^\mu \cos^2 \varphi \right) u \\ \times e^{i(x(q_- - q_+ - q_-) + \alpha \sin \varphi + \beta \sin 2\varphi)}, \quad (9.1.12)$$

where we have defined

$$\alpha = e \left[\frac{p_- a}{kp_-} - \frac{p_+ a}{kp_+} \right], \quad (9.1.13)$$

and

$$\beta = -\frac{e^2 a^2}{8} \left[\frac{1}{kp_+} + \frac{1}{kp_-} \right], \quad (9.1.14)$$

and the vectors

$$B^\mu = \left[\frac{e\phi k}{2kp_+} \gamma^\mu (g_V - g_A \gamma^5) - \gamma^\mu (g_V - g_A \gamma^5) \frac{ek\phi}{2kp_-} \right], \quad (9.1.15)$$

$$C^\mu = -\frac{e\phi k}{2kp_+} \gamma^\mu (g_V - g_A \gamma^5) \frac{ek\phi}{2kp_-} = \frac{e^2 a^2 k^\mu k}{2(kp_+)(kp_-)} (g_V - g_A \gamma^5). \quad (9.1.16)$$

We can then write

$$\cos^n \varphi e^{i(\alpha \sin \varphi + \beta \sin 2\varphi)} = \sum_{s=-\infty}^{\infty} A_n(s, \alpha, \beta) e^{is\varphi}, \quad (9.1.17)$$

for $n = 0, 1, 2$ where

$$A_n(s, \alpha, \beta) = \frac{1}{2\pi} \int_{-\pi}^{\pi} d\varphi \cos^n \varphi e^{if(\varphi)}, \quad (9.1.18)$$

and

$$f(\varphi) = \alpha \sin \varphi + \beta \sin 2\varphi - s\varphi. \quad (9.1.19)$$

The A_n functions encode how the cross-section depends on the external field and will be discussed in detail later in section §9.2.

Inserting equation (9.1.17) into equation (9.1.12) and carrying out the integration over d^4x one obtains

$$J_x^\mu = \sum_{s=-\infty}^{\infty} \bar{v} \left(A_0 \gamma^\mu (g_V - g_A \gamma^5) + A_1 B^\mu + A_2 C^\mu \right) u \times (2\pi)^4 \delta(sk + q - q_+ - q_-). \quad (9.1.20)$$

Here the interpretation of the delta function is that of conservation of momentum at the vertex which now includes a momentum sk from the field. The momentum provided by the field is discrete as seen by the summation over s . I now look at the part of equation (9.1.8) containing the y-coordinate:

$$J_y^\nu = \int d^4y e^{-iqy} \epsilon_Z^{*\nu} e^{i(P_Z + P_H)y} = (2\pi)^4 \epsilon_Z^{*\nu} \delta(P_Z + P_H - q). \quad (9.1.21)$$

Next we carry out the integration over the propagator momentum from equation (9.1.8) by considering

$$\begin{aligned} & \int d^4q J_x^\mu J_y^\nu \\ &= \sum_{s=-\infty}^{\infty} \bar{v} \left(A_0 \gamma^\mu (g_V - g_A \gamma^5) + A_1 B^\mu + A_2 C^\mu \right) u \epsilon_Z^{*\nu} \\ & \quad \times (2\pi)^8 \delta(sk + P_Z + P_H - p_+ - p_-) \end{aligned} \quad (9.1.22)$$

where we have now fixed $q = P_Z + P_H = p_+ + p_- - sk$

Now we can consider

$$\begin{aligned}
& \sum_{\text{spins}} \left| \int d^4q J_x^\mu J_y^\nu \left(g_{\mu\nu} - \frac{q_\mu q_\nu}{M_Z^2} \right) \right|^2 \\
&= \sum_{\text{spins}} \sum_{s, s' = -\infty}^{\infty} \left[\bar{v} \left(A_0 \gamma^\mu (g_V - g_A \gamma^5) + A_1 B^\mu + A_2 C^\mu \right) (s) u \right] \\
&\quad \times \left[\bar{v} \left(A_0 \gamma^\alpha (g_V - g_A \gamma^5) + A_1 B^\alpha + A_2 C^\alpha \right) (s') u \right]^* \\
&\quad \times \left(g_{\mu\nu} - \frac{q_\mu q_\nu}{M_Z^2} \right) \epsilon_Z^{*\nu} \left(g_{\alpha\beta} - \frac{q_\alpha q_\beta}{M_Z^2} \right) \epsilon_Z^\beta \\
&\quad \times (2\pi)^{16} \delta(sk + q - p_+ - p_-) \delta(s'k + q - p_+ - p_-) \quad (9.1.23)
\end{aligned}$$

Due to the delta functions there is only a contribution when $s = s'$ and therefore we have a the delta function squared.

We now define

$$\begin{aligned}
O_{\mu\alpha} &= \sum_{\text{pol}} \left(g_{\mu\nu} - \frac{q_\mu q_\nu}{M_Z^2} \right) \epsilon_Z^{*\nu} \left(g_{\alpha\beta} - \frac{q_\alpha q_\beta}{M_Z^2} \right) \epsilon_Z^\beta \\
&= \left(g_{\mu\nu} - \frac{q_\mu q_\nu}{M_Z^2} \right) \left(g_{\alpha\beta} - \frac{q_\alpha q_\beta}{M_Z^2} \right) \left(-g^{\nu\beta} + \frac{P_Z^\nu P_Z^\beta}{M_Z^2} \right) \\
&= -g_{\mu\alpha} + \frac{P_{Z,\mu} P_{Z,\alpha}}{M_Z^2} + \frac{q_\alpha q_\mu}{M_Z^2} - \frac{q_\alpha P_{Z,\mu} (q \cdot P_Z)}{M_Z^4} + \frac{q_\mu q_\alpha}{M_Z^2} \\
&\quad - \frac{(q \cdot P_Z) q_\mu P_{Z,\alpha}}{M_Z^4} - \frac{q_\alpha q_\mu q^2}{M_Z^4} + \frac{q_\alpha q_\mu (q \cdot P_Z)^2}{M_Z^6} \quad (9.1.24)
\end{aligned}$$

Using then the identity

$$[\bar{v} O_\alpha u] [\bar{v} O_\beta u]^* = \text{Tr} \left[v \bar{v} O_\alpha u \bar{u} \bar{O}_\beta \right], \text{ equation (9.1.23) reduces to}$$

$$\begin{aligned}
 & \sum_{\text{spins}} \left| \int d^4 q J_x^\mu J_y^\nu \left(g_{\mu\nu} - \frac{q_\mu q_\nu}{M_Z^2} \right) \right|^2 \\
 &= \sum_{\text{spins } s=-\infty}^{\infty} O_{\mu\alpha} \\
 & \times \text{Tr} \left[v\bar{v} \left(A_0 \gamma^\mu (g_V - g_A \gamma^5) + A_1 B^\mu + A_2 C^\mu \right) (s) \right. \\
 & \quad \left. \times u\bar{u} \left(\overline{A_0 \gamma^\alpha (g_V - g_A \gamma^5) + A_1 B^\alpha + A_2 C^\alpha} \right) (s) \right] \\
 & \quad \times (2\pi)^{16} \delta(sk + q - p_+ - p_-) \frac{VT}{(2\pi)^4} \quad (9.1.25)
 \end{aligned}$$

where we employed the usual trick when dealing with a delta function squared, $\delta(sk + q - p_+ - p_-)\delta(sk + q - p_+ - p_-) = \delta(sk + q - p_+ - p_-)\frac{VT}{(2\pi)^4}$. We can then replace $\sum_{\text{spins}} v\bar{v} \simeq \not{p}_+$ (we neglect the positron mass) and likewise for the electron to obtain

$$\begin{aligned}
 & \sum_{\text{spins}} \left| \int d^4 q J_x^\mu J_y^\nu \left(g_{\mu\nu} - \frac{q_\mu q_\nu}{M_Z^2} \right) \right|^2 \\
 &= \sum_{\text{spins } s=-\infty}^{\infty} O_{\mu\alpha} \\
 & \times \text{Tr} \left[\not{p}_+ \left(A_0 \gamma^\mu (g_V - g_A \gamma^5) + A_1 B^\mu + A_2 C^\mu \right) (s) \right. \\
 & \quad \left. \times \not{p}_- \left(\overline{A_0 \gamma^\alpha (g_V - g_A \gamma^5) + A_1 B^\alpha + A_2 C^\alpha} \right) (s) \right] \\
 & \quad \times (2\pi)^{16} \delta(sk + q - p_+ - p_-) \frac{VT}{(2\pi)^4} \quad (9.1.26)
 \end{aligned}$$

We will evaluate the contraction of the $O_{\mu\alpha}$ with the tensor inside the trace numerically using a basis of the Dirac gamma matrices, thus the integration of the delta function in equation (9.1.26) remains. We integrate over the final state Z-boson momentum and obtain

$$\int \delta(P_Z + P_H - q_s) d^3 P_Z = \delta(P_H^0 + P_Z^0 - q_s^0) \quad (9.1.27)$$

where $q_s = q_+ + q_- - sk$ and then we have fixed $\vec{P}_Z = \vec{q}_s - \vec{P}_H$. We then rewrite $d^3P_H = |\vec{P}_H|P_H^0 dP_H^0 \sin\theta d\theta d\varphi$ and carry out the integration over P_H^0 , meaning I consider

$$\int \delta(P_H^0 + P_Z^0 - q_s^0) \sqrt{(P_H^0)^2 - M_H^2} P_H^0 dP_H^0 \sin\theta d\theta d\varphi \quad (9.1.28)$$

the delta function fixes $P_H^0 = -P_Z^0 + q_s^0 = q_s^0 - \sqrt{(\vec{q}_s - \vec{P}_H)^2 + M_Z^2}$. The argument of the delta-function is a function of P_H^0 given by

$$\begin{aligned} f(P_H^0) &= P_H^0 - q_s^0 + \sqrt{(\vec{q}_s - \vec{P}_H)^2 + M_Z^2} \\ &= P_H^0 - q_s^0 + \sqrt{\vec{q}_s^2 + (P_H^0)^2 + M_Z^2 - M_H^2 - 2\vec{q}_s \cdot \vec{P}_H} \end{aligned} \quad (9.1.29)$$

Therefore we will use the identity $\delta(f(x)) = \frac{\delta(x-x_0)}{|f'(x_0)|}$ where x_0 is the zero of $f(x)$. Thus we must solve $f(P_H^0) = 0$ which after a lengthy but straightforward calculation yields

$$\begin{aligned} P_H^0 &= \frac{q_s^0 |q_s^2 - M_Z^2 + M_H^2|}{2 \left((q_s^0)^2 - \vec{q}_s^2 \cos^2 \theta \right)} \left(\text{sign}(q_s^2 - M_Z^2 + M_H^2) \right. \\ &\quad \left. \pm \sqrt{1 - \left(1 - \frac{\vec{q}_s^2}{(q_s^0)^2} \cos^2 \theta \right) \left(1 + \frac{4M_H^2 \vec{q}_s^2 \cos^2 \theta}{(q_s^2 - M_Z^2 + M_H^2)^2} \right)} \right) \end{aligned} \quad (9.1.30)$$

where $\cos\theta = \frac{\vec{q}_s \cdot \vec{P}_H}{|\vec{q}_s| |\vec{P}_H|}$. The + solution is chosen when $0 \leq \theta \leq \frac{\pi}{2}$ and the - solution when $\frac{\pi}{2} < \theta \leq \pi$. We need to find the derivative of $f(P_H^0)$ as well for which we obtain

$$f'(P_H^0) = 1 + \frac{P_H^0 \left(1 - \frac{\vec{q}_s \cdot \vec{P}_H}{|\vec{P}_H|^2} \right)}{\sqrt{M_Z^2 + (\vec{q}_s - \vec{P}_H)^2}} \quad (9.1.31)$$

Reality condition on equation (9.1.30) gives us that

$$1 - \left(1 - \frac{\vec{q}_s^2}{(q_s^0)^2} \cos^2 \theta \right) \left(1 + \frac{4M_H^2 \vec{q}_s^2 \cos^2 \theta}{(q_s^2 - M_Z^2 + M_H^2)^2} \right) > 0 \quad (9.1.32)$$

which reduces to

$$\cos^2 \theta > \frac{(q_s^0)^2}{\bar{q}_s^2} - \frac{(q_s^2 - M_Z^2 + M_H^2)^2}{4M_H^2 \bar{q}_s^2} \quad (9.1.33)$$

In principle equation (9.1.33) gives us three different regimes. If we define $a = \frac{(q_s^0)^2}{\bar{q}_s^2} - \frac{(q_s^2 - M_Z^2 + M_H^2)^2}{4M_H^2 \bar{q}_s^2}$ these three regimes are $a < 0$, $0 \leq a \leq 1$ and $a > 1$. The last regime is clearly forbidden since then equation (9.1.33) has no solution, while the first regime $a < 0$ means there is no restriction on the values of θ - there is always a solution. In the intermediate regime there would be certain angles in which emission would be forbidden while allowed in others. The case $a = 1$ corresponds to the production threshold and gives us that

$$\frac{(q_s^0)^2}{\bar{q}_s^2} - \frac{(q_s^2 - M_Z^2 + M_H^2)^2}{4M_H^2 \bar{q}_s^2} = 1 \quad (9.1.34)$$

this can be rewritten as

$$q_s^2 - \frac{(q_s^2 - M_Z^2 + M_H^2)^2}{4M_H^2} = 0 \quad (9.1.35)$$

which can be solved for

$$q_s^2 = (M_H + M_Z)^2 \quad (9.1.36)$$

corresponding to 4-momentum conservation in the case when the produced particles have no momentum. This can then be solved to find the production threshold corresponding to the s 'th harmonic which is then

$$\varepsilon_{\text{th},s} = \frac{s\omega + \sqrt{s^2\omega^2 + \left(1 + \frac{\eta^2}{2}\right) (M_H + M_Z)^2}}{2\left(1 + \frac{\eta^2}{2}\right)} \quad (9.1.37)$$

Combining all of these results we can now obtain the cross section differential in the angles θ and φ of emission of the Higgs-boson.

$$\begin{aligned}
d^2\sigma = & \left(\frac{e^2 M_Z}{2 \cos^2 \theta_W \sin^2 \theta_W} \right)^2 \frac{1}{v_{\text{rel}}} \frac{1}{16 q_-^0 q_+^0 P_H^0 P_Z^0} \\
& \times \frac{1}{((P_H + P_Z)^2 - M_Z^2)^2} \sum_{s=-\infty}^{\infty} O_{\mu\alpha} \\
& \times \text{Tr} \left[\not{p}_+ \left(A_0 \gamma^\mu (g_V - g_A \gamma^5) + A_1 B^\mu + A_2 C^\mu \right) (s) \right. \\
& \times \left. \not{p}_- \left(A_0 \gamma^\alpha (g_V - g_A \gamma^5) + A_1 B^\alpha + A_2 C^\alpha \right) (s) \right] \\
& \times \frac{P_H^0}{|f'(P_H^0)|} \sqrt{(P_H^0)^2 - M_H^2} \sin \theta d\theta d\varphi, \quad (9.1.38)
\end{aligned}$$

where P_H^0 is now the solution found in equation (9.1.30).

9.2 Considerations on the A_n functions

The function

$$A_0(s, \alpha, \beta) = \frac{1}{2\pi} \int_{-\pi}^{\pi} d\varphi e^{i(\alpha \sin \varphi + \beta \sin 2\varphi - s\varphi)} \quad (9.2.1)$$

is the integral representation of the generalized Bessel function \tilde{J} [113], that is

$$A_0(s, \alpha, \beta) = \tilde{J}_s(\alpha, \beta) \quad (9.2.2)$$

which has the series representation

$$\tilde{J}_s(\alpha, \beta) = \sum_{k=-\infty}^{\infty} J_{s-2k}(\alpha) J_k(\beta) \quad (9.2.3)$$

where J is the Bessel function. It is therefore known that \tilde{J} for real arguments α and β . We then have that

$$\tilde{J}_{s-1}(\alpha, \beta) = \frac{1}{2\pi} \int_{-\pi}^{\pi} d\varphi e^{i\varphi} e^{i(\alpha \sin \varphi + \beta \sin 2\varphi - s\varphi)} \quad (9.2.4)$$

and

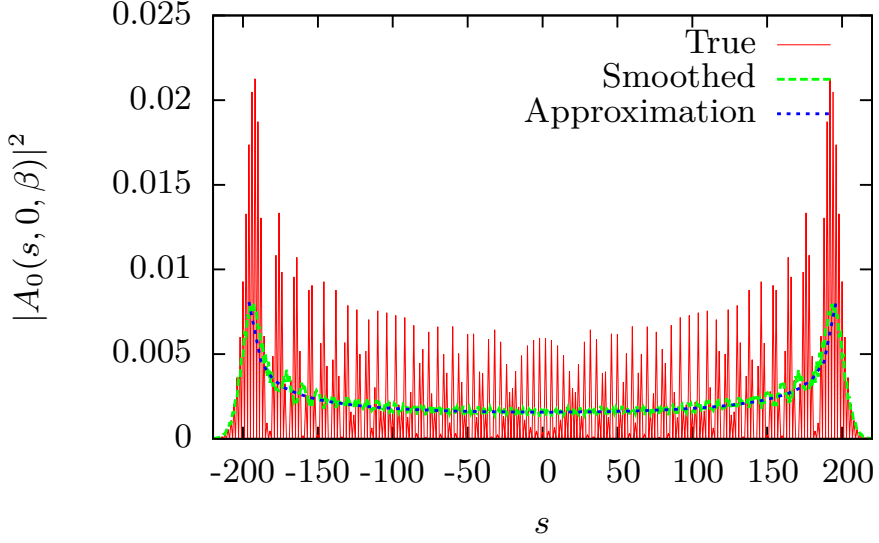


Figure 9.2.1: A plot of $|A_0(s, \alpha, \beta)|^2$ when using the exact formula equation (9.2.8) named 'True' in this figure, a plot of the same function but sent through the smoothing routine of Matlab, and a plot of the continuous approximation of equation (9.2.10).

$$\tilde{J}_{s+1}(\alpha, \beta) = \frac{1}{2\pi} \int_{-\pi}^{\pi} d\varphi e^{-i\varphi} e^{i(\alpha \sin \varphi + \beta \sin 2\varphi - s\varphi)} \quad (9.2.5)$$

and so

$$\begin{aligned} & \frac{1}{2} \left(\tilde{J}_{s-1}(\alpha, \beta) + \tilde{J}_{s+1}(\alpha, \beta) \right) \\ &= \frac{1}{2\pi} \int_{-\pi}^{\pi} d\varphi \frac{e^{i\varphi} + e^{-i\varphi}}{2} e^{i(\alpha \sin \varphi + \beta \sin 2\varphi - s\varphi)} \\ &= \frac{1}{2\pi} \int_{-\pi}^{\pi} d\varphi \cos \varphi e^{i(\alpha \sin \varphi + \beta \sin 2\varphi - s\varphi)} \\ &= A_1(s, \alpha, \beta) \quad (9.2.6) \end{aligned}$$

And similarly

$$\begin{aligned}
 A_2(s, \alpha, \beta) &= \frac{1}{2\pi} \int_{-\pi}^{\pi} d\varphi \left(\frac{e^{i\varphi} + e^{-i\varphi}}{2} \right)^2 e^{i(\alpha \sin \varphi + \beta \sin 2\varphi - s\varphi)} \\
 &= \frac{1}{2\pi} \int_{-\pi}^{\pi} d\varphi \left(\frac{1}{2} + \frac{e^{i2\varphi} + e^{-i2\varphi}}{4} \right) e^{i(\alpha \sin \varphi + \beta \sin 2\varphi - s\varphi)} \\
 &= \frac{1}{2} \tilde{J}_s(\alpha, \beta) + \frac{1}{4} \left(\tilde{J}_{s-2}(\alpha, \beta) + \tilde{J}_{s+2}(\alpha, \beta) \right) \quad (9.2.7)
 \end{aligned}$$

Case: $\alpha = 0$

In the perfectly head-on collision where \mathbf{k} and \mathbf{p}_+ are parallel, we have $\alpha = 0$ in which case we only have a contribution in equation (9.2.3) when $s = 2k$, since the Bessel function of 0 is only non-zero if the order of the Bessel function is 0, meaning s must be even and in which case

$$\tilde{J}_s(0, \beta) = J_{\frac{s}{2}}(\beta). \quad (9.2.8)$$

From equation (9.1.38) it is seen that we are interested in the products $A_m A_n^*$ but due to the conditions written above we must have that $m + n$ is even. In an application β will typically be large as can be seen by

$$\beta \simeq -\frac{e^2 a^2}{8} \frac{1}{kp_+} = \frac{\eta^2 m^2}{8} \frac{2\gamma^2}{\omega\varepsilon} = \frac{\eta^2}{4} \frac{\varepsilon}{\omega}, \quad (9.2.9)$$

where we have defined $\eta = eE_0/m\omega$ where E_0 is the peak electric field strength. In the interesting regime η must be on the order of unity or larger, and thus $\beta \sim 10^{10}$. Therefore approximations which can be applied when $\beta \gg 1$ will be useful. As stated earlier, there will be contributions from terms where s is comparable in size to the very large parameter β . Therefore, since β is large, many photon quanta will take part in the process, and therefore the quantization in integer s is only of minor importance. A property of the Bessel function is that in our case, a sharp drop off is seen when $|s| > 2\beta$. We therefore seek continuous approximations of the functions $A_m A_n^*$ over the interval $-2\beta < s < 2\beta$ and found the functions below based on fits to the smoothed values of the discrete A_n functions. The normalization constant was then found by requiring the

integral to equal the sum, e.g. $\int_{-2\beta}^{2\beta} |\tilde{A}_0(s, 0, \beta)|^2 ds = \sum_s |A_0(s, 0, \beta)|^2$. Here \tilde{A}_n denotes the continuous version of A_n

$$|\tilde{A}_0(s, 0, \beta)|^2 = \frac{1}{(4\beta)^{1-\frac{1}{\sqrt{3}}}(3+\sqrt{3})} \left(\frac{1}{(2\beta-s)^{1/\sqrt{3}}} + \frac{1}{(s+2\beta)^{1/\sqrt{3}}} \right) \quad (9.2.10)$$

$$\begin{aligned} \tilde{A}_0(s, 0, \beta)\tilde{A}_2(s, 0, \beta)^* &= |\tilde{A}_1(s, 0, \beta)|^2 \\ &= (4\beta)^{1/\sqrt{3}-2} \frac{(s+2\beta)}{(3+\sqrt{3})} \left(\frac{1}{(2\beta-s)^{1/\sqrt{3}}} + \frac{1}{(s+2\beta)^{1/\sqrt{3}}} \right) \end{aligned} \quad (9.2.11)$$

$$\begin{aligned} |\tilde{A}_2(s, 0, \beta)|^2 &= \frac{3}{8}(2\beta)^{1/\sqrt{3}-3} \frac{143(s+2\beta)^2}{2^{2-1/\sqrt{3}}(315+113\sqrt{3})} \\ &\quad \times \left(\frac{1}{(2\beta-s)^{1/\sqrt{3}}} + \frac{1}{(s+2\beta)^{1/\sqrt{3}}} \right) \end{aligned} \quad (9.2.12)$$

If we use equation (9.2.9) and equation (9.1.37) and that for large β values the production threshold corresponds to $s = -2\beta$. We then obtain the equation

$$\varepsilon_{\text{th}} = \frac{-\frac{\eta^2}{2}\varepsilon_{\text{th}} + \sqrt{\left(\frac{\eta^2}{2}\varepsilon_{\text{th}}\right)^2 + \left(1 + \frac{\eta^2}{2}\right)(M_H + M_Z)^2}}{2\left(1 + \frac{\eta^2}{2}\right)}$$

which can be solved to obtain

$$\varepsilon_{\text{th}} = \frac{(M_H + M_Z)}{2} \frac{1}{\sqrt{1 + \eta^2}} \quad (9.2.13)$$

9.3 Classical approach

The classical approach consists of calculating the classical motion of the charge in the laser field and based on this, find the probability distribution of the energies that the charge possesses. The external field is given by

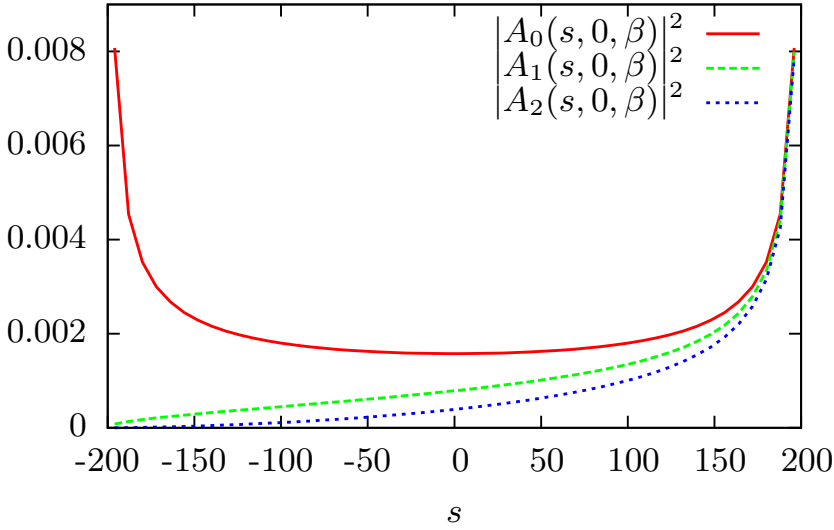


Figure 9.2.2: A comparison of the obtained approximations seen in equation (9.2.10), equation (9.2.11) and equation (9.2.12) for the case of $\beta = 100$.

$$\mathbf{E} = \hat{x}E_0 \cos(\omega(t - z) + \phi_0) \quad (9.3.1)$$

$$\mathbf{B} = \hat{y}E_0 \cos(\omega(t - z) + \phi_0) \quad (9.3.2)$$

Where E_0 is the electric field amplitude and ϕ_0 is an initial phase which can be between 0 and 2π . We then have

$$\frac{d}{dt}(\gamma m \mathbf{v}) = eE_0 \cos(\omega(t - z) + \phi_0) (\hat{x} + \mathbf{v} \times \hat{y}) \quad (9.3.3)$$

$$\dot{\gamma} m \mathbf{v} + \gamma m \dot{\mathbf{v}} = eE_0 \cos(\omega(t - z) + \phi_0) (\hat{x}(1 - v_z) + \hat{z}v_x) \quad (9.3.4)$$

We then use that $\dot{\gamma} m = e\mathbf{E} \cdot \mathbf{v} = eE_0 \cos(\omega(t - z))v_x$ so that

$$\gamma m \dot{\mathbf{v}} = eE_0 \cos(\omega(t - z) + \phi_0) \left(\hat{x}(1 - v_x^2 - v_z) + \hat{z}v_x(1 - v_z) \right) \quad (9.3.5)$$

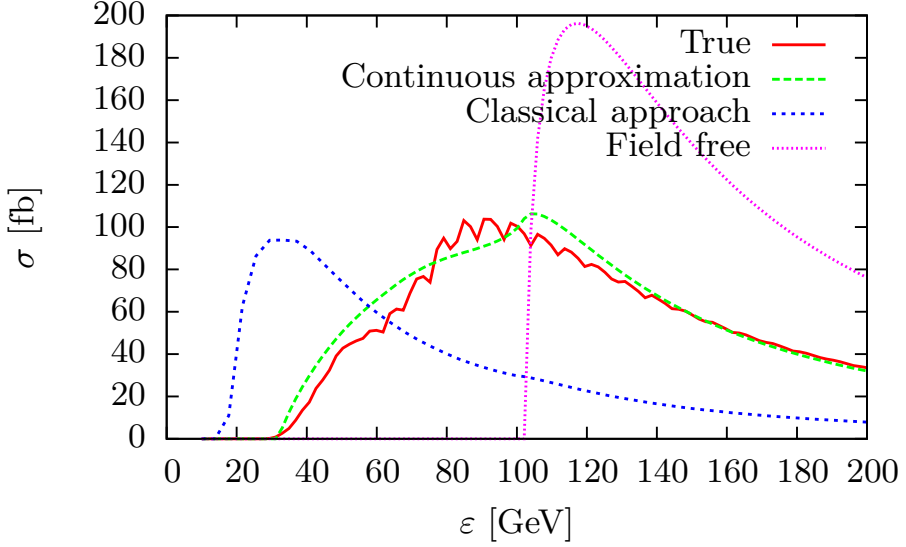


Figure 9.3.1: Here I show the results for the case of $\eta = 3$ using the exact solution (red curve), the continuous approximation (green curve), the classical approach (blue curve) and the field free case (magenta curve).

In this problem we have a precise dependence on the difference between two large quantities $t - z$ and $1 - v_z$ which can become problematic numerically. For this reason we once again change variable to

$$z = v_0 t + \delta z \quad (9.3.6)$$

and thus

$$v_z = v_0 + \delta v_z \quad (9.3.7)$$

where $v_0 \simeq 1 - \frac{1}{2\gamma_0^2}$ where γ_0 is the initial value of the Lorentz gamma factor. Then $\dot{v}_x = \delta \dot{v}_z$. Therefore we obtain the three coupled equations

$$\dot{v}_x = \frac{eE_0}{\gamma m} \cos\left(\omega\left(\frac{t}{2\gamma_0^2} - \delta z\right) + \phi_0\right)\left(\frac{1}{2\gamma_0^2} - \delta v_z - v_x^2\right) \quad (9.3.8)$$

$$\delta\dot{v}_z = \frac{eE_0}{\gamma m} \cos\left(\omega\left(\frac{t}{2\gamma_0^2} - \delta z\right) + \phi_0\right) v_x \left(\frac{1}{2\gamma_0^2} - \delta v_z\right) \quad (9.3.9)$$

$$\dot{\gamma} = \frac{eE_0}{\gamma m} \cos\left(\omega\left(\frac{t}{2\gamma_0^2} - \delta z\right) + \phi_0\right) v_x. \quad (9.3.10)$$

These can be solved numerically. By solving these equations over one period of oscillation of the charge T , we can obtain the probability distribution of energies by evaluating $m\gamma(t)$ over an equidistant grid of times from 0 to T and produce a histogram over these energies. This is the relevant distribution since each time is weighted equally, meaning we assume particle production to happen at a random time. This procedure is then averaged over the initial phase ϕ_0 . In [78] it is seen in eq. (1) that the energy of the charge in our case is given by

$$\varepsilon(\phi) = \varepsilon_0 + \frac{e^2}{2} \frac{(\mathbf{A}(\phi) - \mathbf{A}(\phi_0))^2}{\varepsilon_0 - p_0}$$

It is therefore seen that the maximum energy possible classically occurs when $\phi_0 = 0$ and $\phi = \pi$ and is $\varepsilon = \varepsilon_0 + \frac{4e^2 a^2}{2\varepsilon_0} 2\gamma_0^2 = \varepsilon_0(1 + 4\eta^2)$. Since only the electron which co-propagates with the field experiences this large acceleration, the center of mass energy is

$$E_{\text{cm}} = \sqrt{s} \simeq \sqrt{(\varepsilon_1 + \varepsilon_0)^2 - (\varepsilon_1 - \varepsilon_0)^2} = \sqrt{4\varepsilon_1\varepsilon_0} = \sqrt{4\varepsilon_0^2(1 + 4\eta^2)}$$

The condition that $E_{\text{cm}} = M_H + M_Z$ therefore gives us the production threshold

$$\varepsilon_{\text{th}} = \frac{M_H + M_Z}{2} \frac{1}{\sqrt{1 + 4\eta^2}}.$$

In figure 9.3.1 I have shown the results of these calculations for the case of $\eta = 3$ and $\omega = 25\text{GeV}$. This is not a realistically achievable photon energy and it is only chosen since fewer harmonics are necessary in the sum over s in equation (9.1.38) making comparison possible with the continuous approximation. In this case I have summed from $s = -450$ to $s = 450$ which from equation (9.1.37) can be determined to be adequate since $s = -450$ has a production threshold above the end of the interval in this figure.

From the continuous approximation it is seen that the direct dependence on ω disappears, and the only important parameter in the problem is η when $\beta \gg 1$ and $\alpha = 0$. Only when β is small, is it important that the field delivers the energy in quanta of ω . A deviation from the field free result is seen when η approaches or is larger than 1. It is interesting that such a disagreement is seen with the classical approach, which also hints that the problem stated in the beginning of this chapter could show interesting results. In the case of crossing bunches, there is not any appreciable extra energy available from the external field, as is the case with the laser, but the field could still have an influence to change the cross section beyond that which would be expected from a 'classical approach' as outlined here.

Bibliography

- [1] Tobias N Wistisen. Leptons and photons in strong electromagnetic fields, part a - progress report. 2014.
- [2] Tobias N. Wistisen and Ulrik I. Uggerhøj. Vacuum birefringence by compton backscattering through a strong field. *Phys. Rev. D*, 88:053009, Sep 2013.
- [3] Tobias N. Wistisen, Kristoffer K. Andersen, Serdar Yilmaz, Rune Mikkelsen, John Lundsgaard Hansen, Ulrik I. Uggerhøj, Werner Lauth, and Hartmut Backe. Experimental realization of a new type of crystalline undulator. *Phys. Rev. Lett.*, 112:254801, Jun 2014.
- [4] Tobias N. Wistisen. Interference effect in nonlinear compton scattering. *Phys. Rev. D*, 90:125008, Dec 2014.
- [5] Tobias N. Wistisen. Quantum synchrotron radiation in the case of a field with finite extension. *Phys. Rev. D*, 92:045045, Aug 2015.
- [6] T. N. Wistisen, U. I. Uggerhøj, U. Wienands, T. W. Markiewicz, R. J. Noble, B. C. Benson, T. Smith, E. Bagli, L. Bandiera, G. Germogli, V. Guidi, A. Mazzolari, R. Holtzapple, and S. Tucker. Channeling, volume reflection, and volume capture study of electrons in a bent silicon crystal. *Phys. Rev. Accel. Beams*, 19:071001, Jul 2016.
- [7] K. K. Andersen, S. L. Andersen, J. Esberg, H. Knudsen, R. E. Mikkelsen, U. I. Uggerhøj, T. N. Wistisen, P. Sona, A. Mangiarotti, and T. J. Ketel. Experimental investigation of the

- landau-pomeranchuk-migdal effect in low- z targets. *Phys. Rev. D*, 88:072007, Oct 2013.
- [8] K.K. Andersen, S.L. Andersen, H. Knudsen, R.E. Mikkelsen, H.D. Thomsen, U.I. Uggerhøj, T.N. Wistisen, J. Esberg, P. Sona, A. Mangiarotti, and T.J. Ketel. Measurements of the spectral location of the structured target resonance for ultrarelativistic electrons. *Physics Letters B*, 732(0):309 – 314, 2014.
- [9] U. Wienands, T. W. Markiewicz, J. Nelson, R. J. Noble, J. L. Turner, U. I. Uggerhøj, T. N. Wistisen, E. Bagli, L. Bandiera, G. Germogli, V. Guidi, A. Mazzolari, R. Holtzapple, and M. Miller. Observation of deflection of a beam of multi-gev electrons by a thin crystal. *Phys. Rev. Lett.*, 114:074801, Feb 2015.
- [10] U.I. Uggerhøj and T.N. Wistisen. Intense and energetic radiation from crystalline undulators. *Nuclear Instruments and Methods in Physics Research Section B: Beam Interactions with Materials and Atoms*, 355:35 – 38, 2015.
- [11] Ulrik I Uggerhøj and Tobias N Wistisen. A method to measure vacuum birefringence at fcc-ee. *arXiv preprint arXiv:1605.02861*, 2016.
- [12] Stephen John Sque. *Bulk and transfer doping of diamond*. PhD thesis, University of Exeter, 2005.
- [13] J.C. Kimball and N. Cue. Quantum electrodynamics and channeling in crystals. *Physics Reports*, 125(2):69 – 101, 1985.
- [14] J. Lindhard. Influence of crystal lattice on motion of energetic charged particles. *Danske Vid. Selsk. Mat. Fys. Medd.*, 34:14, 1965.
- [15] V.B. Berestetskii, E.M. Lifshitz, and L.P. Pitaevskii. *Quantum Electrodynamics*. Elsevier, 1982.
- [16] V.N. Baier, V.M. Katkov, and V.M. Strakhovenko. *Electromagnetic Processes at High Energies in Oriented Single Crystals*. World Scientific, 1998.

- [17] J. Beringer, J. F. Arguin, R. M. Barnett, and et. al. Review of particle physics. *Phys. Rev. D*, 86:010001, Jul 2012.
- [18] W. Scandale, R. Losito, E. Bagli, L. Bandiera, P. Dalpiaz, M. Fiorini, V. Guidi, A. Mazzolari, D. Vincenzi, G. Della Mea, E. Vallazza, A.G. Afonin, Yu.A. Chesnokov, V.A. Maisheev, I.A. Yazynin, A.D. Kovalenko, A.M. Taratin, A.S. Denisov, Yu.A. Gavrikov, Yu.M. Ivanov, L.P. Lapina, V.V. Skorobogatov, D. Bolognini, S. Hasan, and M. Prest. Measurement of the dechanneling length for high-energy negative pions. *Physics Letters B*, 719(1-3):70 – 73, 2013.
- [19] A. Mazzolari, E. Bagli, L. Bandiera, V. Guidi, H. Backe, W. Lauth, V. Tikhomirov, A. Berra, D. Lietti, M. Prest, E. Vallazza, and D. De Salvador. Steering of a sub-gev electron beam through planar channeling enhanced by rechanneling. *Phys. Rev. Lett.*, 112:135503, Apr 2014.
- [20] V.I. Ritus. Quantum effects of the interaction of elementary particles with an intense electromagnetic field. *Journal of Soviet Laser Research*, 6(5):497–617, 1985.
- [21] John David Jackson. *Classical Electrodynamics*. John Wiley & Sons, Inc., New Jersey, USA, 3 edition, 1991.
- [22] KA Olive et al. Particle data group collaboration. *Chin. Phys. C*, 38:090001, 2014.
- [23] Andriy Kostyuk. Crystalline undulator with a small amplitude and a short period. *Phys. Rev. Lett.*, 110:115503, Mar 2013.
- [24] Ulrik I. Uggerhøj. The interaction of relativistic particles with strong crystalline fields. *Rev. Mod. Phys.*, 77:1131–1171, Oct 2005.
- [25] Andriy Kostyuk. Strained layer crystalline undulator. *arXiv preprint arXiv:1301.4491*, 2013.
- [26] Donald S. Gemmell. Channeling and related effects in the motion of charged particles through crystals. *Rev. Mod. Phys.*, 46:129–227, Jan 1974.

- [27] Mikhail Leonovich Ter-Mikaelian. *High-energy electromagnetic processes in condensed media*. Wiley-Interscience, 1972.
- [28] Walter Scandale, Alberto Carnera, Gianantonio Della Mea, Davide De Salvador, Riccardo Milan, Alberto Vomiero, Stefano Baricordi, Pietro Dalpiaz, Massimiliano Fiorini, Vincenzo Guidi, Giuliano Martinelli, Andrea Mazzolari, Emiliano Milan, Giovanni Ambrosi, Philipp Azzarello, Roberto Battiston, Bruna Bertucci, William J. Burger, Maria Ionica, Paolo Zuccon, Gianluca Cavoto, Roberta Santacesaria, Paolo Valente, Erik Vallazza, Alexander G. Afonin, Vladimir T. Baranov, Yury A. Chesnokov, Vladilen I. Kotov, Vladimir A. Maishev, Igor A. Yazynin, Sergey V. Afanasiev, Alexander D. Kovalenko, Alexander M. Taratin, Alexander S. Denisov, Yury A. Gavrikov, Yuri M. Ivanov, Vladimir G. Ivochkin, Sergey V. Kosyanenko, Anatoli A. Petrunin, Vyacheslav V. Skorobogatov, Vsevolod M. Suvorov, Davide Bolognini, Luca Foggetta, Said Hasan, and Michela Prest. Deflection of 400 GeV/c proton beam with bent silicon crystals at the cern super proton synchrotron. *Phys. Rev. ST Accel. Beams*, 11:063501, Jun 2008.
- [29] R. A. Carrigan, D. Chen, G. Jackson, N. Mokhov, C. T. Murphy, S. Baker, A. Bogacz, D. Cline, S. Ramachandran, J. Rhoades, J. Rosenzweig, A. Asseev, V. Biryukov, A. Taratin, J. A. Ellison, A. Khanzadeev, T. Prokofieva, V. Samsonov, G. Solodov, B. Newberger, E. Tsyganov, H.-J. Shih, W. Gabella, B. Cox, V. Golovatyuk, and A. McManus. Beam extraction studies at 900 gev using a channeling crystal. *Phys. Rev. ST Accel. Beams*, 5:043501, Apr 2002.
- [30] S.P. Møller, E. Uggerhøj, H.W. Atherton, M. Clement, N. Doble, K. Elsener, L. Gatignon, and P. Grafstr. High efficiency bending of 450 gev protons using channeling. *Physics Letters B*, 256(1):91 – 96, 1991.
- [31] N.V. Mokhov, G.E. Annala, A. Apyan, R.A. Carrigan, A.I. Drozhdin, T.R. Johnson, A.M. Legan, R.E. Reilly, V. Shiltsev, D.A. Still, R.J. Tesarek, J. Zagel, S. Peggs, R.W. Assmann, V. Previtalli, S. Redaelli, W. Scandale, S. Shiraishi, Y.A.

- Chesnokov, I.A. Yazynin, V. Guidi, M. Prest, and Y.M. Ivanov. *CRYSTAL COLLIMATION STUDIES AT THE TEVATRON (T-980)*. WORLD SCIENTIFIC, 2012.
- [32] N Mokhov, J Annala, R Carrigan, M Church, A Drozhdin, T Johnson, R Reilly, V Shiltsev, G Stancari, D Still, A Valishev, X L Zhang, and V Zvoda. Tevatron beam halo collimation system: design, operational experience and new methods. *Journal of Instrumentation*, 6(08):T08005, 2011.
- [33] R. Carrigan, V. Lebedev, N. Mokhov, S. Nagaitsev, V. Shiltsev, G. Stancari, D. Still, and A. Valishev. *Accelerator Physics at the Tevatron Collider*, chapter Emittance Growth and Beam Loss, pages 187–258. Springer New York, New York, NY, 2014.
- [34] A. Kostyuk. Recent progress in the theory of the crystalline undulator. *Nuclear Instruments and Methods in Physics Research Section B: Beam Interactions with Materials and Atoms*, 309(0):45 – 49, 2013.
- [35] U. Mikkelsen and E. Uggerhøj. A crystalline undulator based on graded composition strained layers in a superlattice. *Nuclear Instruments and Methods in Physics Research Section B: Beam Interactions with Materials and Atoms*, 160(3):435 – 439, 2000.
- [36] R. O. Avakyan, L. A. Gevorgyan, K. A. Ispiryan, and R. K. Ispiryan. Radiation from particles in crystal undulators with allowance for a polarization of the medium. *Journal of Experimental and Theoretical Physics Letters*, 68(6):467–471, 1998.
- [37] Andrei V Korol, Andrey V Solov'yov, and Walter Greiner. Coherent radiation of an ultrarelativistic charged particle channelled in a periodically bent crystal. *Journal of Physics G: Nuclear and Particle Physics*, 24(5):L45, 1998.
- [38] S. Bellucci, S. Bini, V. M. Biryukov, Yu. A. Chesnokov, S. Dabagov, G. Giannini, V. Guidi, Yu. M. Ivanov, V. I. Kotov, V. A. Maishev, C. Malagù, G. Martinelli, A. A. Petrunin, V. V. Skorobogatov, M. Stefancich, and D. Vincenzi. Experimental study

- for the feasibility of a crystalline undulator. *Phys. Rev. Lett.*, 90:034801, Jan 2003.
- [39] Søren Pape Møller. High-energy channeling - applications in beam bending and extraction. *Nuclear Instruments and Methods in Physics Research Section A: Accelerators, Spectrometers, Detectors and Associated Equipment*, 361(3):403 – 420, 1995.
- [40] V.M. Biryukov, Y.A. Chesnokov, and V.I. Kotov. *Crystal Channeling and its Application at High-Energy Accelerators*. Springer-Verlag Berlin Heidelberg, 1997.
- [41] W. Scandale, A. Vomiero, S. Baricordi, P. Dalpiaz, M. Fiorini, V. Guidi, A. Mazzolari, R. Milan, Gianantonio Della Mea, G. Ambrosi, B. Bertucci, W. J. Burger, M. Duranti, P. Zuccon, G. Cavoto, F. Iacoangeli, C. Luci, S. Pisano, R. Santacesaria, P. Valente, E. Vallazza, A. G. Afonin, Yu. A. Chesnokov, V. I. Kotov, V. A. Maisheev, I. A. Yazynin, A. D. Kovalenko, A. M. Taratin, A. S. Denisov, Yu. A. Gavrikov, Yu. M. Ivanov, L. P. Lapina, L. G. Malyarenko, V. V. Skorobogatov, V. M. Suvorov, S. A. Vavilov, D. Bolognini, S. Hasan, D. Lietti, A. Mozzanica, and M. Prest. Volume reflection dependence of 400 GeV/c protons on the bent crystal curvature. *Phys. Rev. Lett.*, 101:234801, Dec 2008.
- [42] V.M. Biryukov. The limits of volume reflection in bent crystals. *Nuclear Instruments and Methods in Physics Research Section B: Beam Interactions with Materials and Atoms*, 267(14):2457 – 2459, 2009.
- [43] W. Scandale, A. Vomiero, E. Bagli, S. Baricordi, P. Dalpiaz, M. Fiorini, V. Guidi, A. Mazzolari, D. Vincenzi, R. Milan, G. Della Mea, E. Vallazza, A. G. Afonin, Yu. A. Chesnokov, V. A. Maisheev, I. A. Yazynin, A. D. Kovalenko, A. M. Taratin, A. S. Denisov, Yu. A. Gavrikov, Yu. M. Ivanov, L. P. Lapina, L. G. Malyarenko, V. V. Skorobogatov, V. M. Suvorov, S. A. Vavilov, D. Bolognini, S. Hasan, A. Mattera, M. Prest, and V. V. Tikhomirov. Observation of multiple volume reflection by different planes in one bent silicon crystal for high-energy negative particles. *EPL (Europhysics Letters)*, 93(5):56002, 2011.

- [44] A.M. Taratin and S.A. Vorobiev. Volume reflection of high-energy charged particles in quasi-channeling states in bent crystals. *Physics Letters A*, 119(8):425 – 428, 1987.
- [45] G. Germogli, A. Mazzolari, L. Bandiera, E. Bagli, and V. Guidi. Manufacturing and characterization of bent silicon crystals for studies of coherent interactions with negatively charged particles beams. *Nuclear Instruments and Methods in Physics Research Section B: Beam Interactions with Materials and Atoms*, 355:81 – 85, 2015.
- [46] Riccardo Camattari, Vincenzo Guidi, Valerio Bellucci, and Andrea Mazzolari. The ‘quasi-mosaic’ effect in crystals and its applications in modern physics. *Journal of Applied Crystallography*, 48(4):977–989, Aug 2015.
- [47] Jamie Rosenzweig and Luca Serafini. *The Physics of High Brightness Beams: Proceedings of the 2nd ICFA Advanced Accelerator Workshop*. World Scientific, 2000.
- [48] AH Sørensen and E Uggerhøj. Channeling, radiation and applications. 1989.
- [49] E Bagli, M Asai, D Brandt, A Dotti, V Guidi, and DH Wright. A model for the interaction of high-energy particles in straight and bent crystals implemented in geant4. *Eur. Phys. J. C*, 74(8):2996, 2014.
- [50] Martin Schumacher. Delbrück scattering. *Radiation Physics and Chemistry*, 56(1–2):101 – 111, 1999.
- [51] Julian Schwinger. On gauge invariance and vacuum polarization. *Phys. Rev.*, 82:664–679, Jun 1951.
- [52] Ralf Schützhold, Holger Gies, and Gerald Dunne. Dynamically assisted schwinger mechanism. *Phys. Rev. Lett.*, 101:130404, Sep 2008.
- [53] D. B. Blaschke, A. V. Prozorkevich, G. Röpke, C. D. Roberts, S. M. Schmidt, D. S. Shkirmanov, and S. A. Smolyansky.

- Dynamical schwinger effect and high-intensity lasers. realising nonperturbative qed. *The European Physical Journal D*, 55(2):341–358, 2009.
- [54] James J. Klein and B. P. Nigam. Birefringence of the vacuum. *Phys. Rev.*, 135:B1279–B1280, Sep 1964.
- [55] Victor Dinu, Tom Heinzl, Anton Ilderton, Mattias Marklund, and Greger Torgrimsson. Vacuum refractive indices and helicity flip in strong-field qed. *Phys. Rev. D*, 89:125003, Jun 2014.
- [56] Thomas Heinzl, Ben Liesfeld, Kay-Uwe Amthor, Heinrich Schworer, Roland Sauerbrey, and Andreas Wipf. On the observation of vacuum birefringence. *Optics Communications*, 267(2):318 – 321, 2006.
- [57] Stephen L Adler. Vacuum birefringence in a rotating magnetic field. *Journal of Physics A: Mathematical and Theoretical*, 40(5):F143, 2007.
- [58] Guido Zavattini, Ugo Gastaldi, Ruggero Pengo, Giuseppe Ruoso, Federico Della Valle, et al. Measuring the magnetic birefringence of vacuum: the PVLAS experiment. *Int.J.Mod.Phys.*, A27:1260017, 2012.
- [59] F. Bielsa, R. Battesti, M. Fouché, P. Berceau, C. Robilliard, G. Bailly, S. Batut, J. Mauchain, M. Nardone, O. Portugall, and C. Rizzo. Status of the BMV experiment. *ArXiv e-prints*, November 2009.
- [60] W. Heisenberg and H. Euler. Folgerungen aus der diracschen theorie des positrons. *Zeitschrift für Physik*, 98(11-12):714–732, 1936.
- [61] Vladimir B Beresteckij, Evgenij M Lifsic, and Lev P Pitaevskij. *Quantum electrodynamics*. Butterworth-Heinemann, Oxford, 2008.
- [62] J.S. Toll. Thesis. *Princeton University*, 1952.
- [63] G.M. Shore. Superluminality and uv completion. *Nuclear Physics B*, 778(3):219 – 258, 2007.

- [64] Michael Bass. *Handbook of Optics: Volume I - Geometrical and Physical Optics, Polarized Light, Components and Instruments, Third Edition*. McGraw-Hill Professional: New York, Chicago, San Francisco, Lisbon, London, Madrid, Mexico City, Milan, New Delhi, San Juan, Seoul, Singapore, Sydney, Toronto, 2010.
- [65] I.F. Ginzburg, G.L. Kotkin, S.L. Panfil, V.G. Serbo, and V.I. Telnov. Colliding γe and $\gamma\gamma$ beams based on single-pass e^+e^- accelerators ii. polarization effects, monochromatization improvement. *Nuclear Instruments and Methods in Physics Research*, 219(1):5 – 24, 1984.
- [66] R. Cameron, G. Cantatore, A. C. Melissinos, G. Ruoso, Y. Semertzidis, H. J. Halama, D. M. Lazarus, A. G. Prodell, F. Nezirick, C. Rizzo, and E. Zavattini. Search for nearly massless, weakly coupled particles by optical techniques. *Phys. Rev. D*, 47:3707–3725, May 1993.
- [67] Tobias N. Wistisen. Erratum: Interference effect in nonlinear compton scattering [phys. rev. d **90** , 125008 (2014)]. *Phys. Rev. D*, 91:069903, Mar 2015.
- [68] C. Bula, K. T. McDonald, E. J. Prebys, C. Bamber, S. Boege, T. Kotseroglou, A. C. Melissinos, D. D. Meyerhofer, W. Ragg, D. L. Burke, R. C. Field, G. Horton-Smith, A. C. Odian, J. E. Spencer, D. Walz, S. C. Berridge, W. M. Bugg, K. Shmakov, and A. W. Weidemann. Observation of nonlinear effects in compton scattering. *Phys. Rev. Lett.*, 76:3116–3119, Apr 1996.
- [69] K.T. McDonald. Proposal for experimental studies of nonlinear quantum electrodynamics. September 1986.
- [70] K. K. Andersen, J. Esberg, H. Knudsen, H. D. Thomsen, U. I. Uggerhøj, P. Sona, A. Mangiarotti, T. J. Ketel, A. Dizdar, and S. Ballestrero. Experimental investigations of synchrotron radiation at the onset of the quantum regime. *Phys. Rev. D*, 86:072001, Oct 2012.

- [71] R. Moore, M.A. Parker, A. Baurichter, K. Kirsebom, R. Medenwaldt, U. Mikkelsen, S.P. Møller, E. Uggerhøj, T. Worm, N. Doble, K. Elsener, S. Ballestrero, P. Sona, V.M. Strakhovenko, C. Biino, and Z.Z. Vilakazi. Measurement of pair-production by high energy photons in an aligned tungsten crystal. *Nuclear Instruments and Methods in Physics Research Section B: Beam Interactions with Materials and Atoms*, 119(1-2):149 – 155, 1996.
- [72] D. Seipt and B. Kämpfer. Nonlinear compton scattering of ultrashort intense laser pulses. *Phys. Rev. A*, 83:022101, Feb 2011.
- [73] Madalina Boca and Viorica Florescu. Nonlinear compton scattering with a laser pulse. *Phys. Rev. A*, 80:053403, Nov 2009.
- [74] T. Heinzl, D. Seipt, and B. Kämpfer. Beam-shape effects in nonlinear compton and thomson scattering. *Phys. Rev. A*, 81:022125, Feb 2010.
- [75] E. S. Sarachik and G. T. Schappert. Classical theory of the scattering of intense laser radiation by free electrons. *Phys. Rev. D*, 1:2738–2753, May 1970.
- [76] Martin Lavelle, David McMullan, and Merfat Raddadi. Propagation in an intense background. *Phys. Rev. D*, 87:085024, Apr 2013.
- [77] Chris Harvey, Thomas Heinzl, Anton Ilderton, and Mattias Marklund. Intensity-dependent electron mass shift in a laser field: Existence, universality, and detection. *Phys. Rev. Lett.*, 109:100402, Sep 2012.
- [78] A. Di Piazza, C. Müller, K. Z. Hatsagortsyan, and C. H. Keitel. Extremely high-intensity laser interactions with fundamental quantum systems. *Rev. Mod. Phys.*, 84:1177–1228, Aug 2012.
- [79] F Ehlötzky, K Krajewska, and J Z Kaminski. Fundamental processes of quantum electrodynamics in laser fields of relativistic power. *Reports on Progress in Physics*, 72(4):046401, 2009.

- [80] Vladimir B Beresteckij, Evgenij M Lifsic, and Lev P Pitaevskij. *Quantum electrodynamics*. Butterworth-Heinemann, Oxford, 2008.
- [81] A. Belkacem, N. Cue, and J.C. Kimball. Theory of crystal-assisted radiation and pair creation for imperfect alignment. *Physics Letters A*, 111(1-2):86 – 90, 1985.
- [82] NP Klepikov. Emission of photons or electron-positron pairs in magnetic fields. *Zhur. Eksptl.'i Teoret. Fiz.*, 26, 1954.
- [83] Julian Schwinger and Wu yang Tsai. New approach to quantum corrections in synchrotron radiation. *Annals of Physics*, 110(1):63 – 84, 1978.
- [84] Arsenic Aleksandrovich Sokolov and Igor Michajlovic Ternov. Synchrotron radiation. *Akademia Nauk SSSR, Moskovskoie Obshchestvo Ispytatelei prirody. Sektsia Fiziki. Sinkhrotron Radiation, Nauka Eds., Moscow, 1966 (Russian title: Sinkhrotronnoie izluchenie), 228 pp., 1, 1966.*
- [85] Julian Schwinger, Wu yang Tsai, and Thomas Erber. Classical and quantum theory of synergic synchrotron-cherenkov radiation. *Annals of Physics*, 96(2):303 – 332, 1976.
- [86] J. Esberg, U. I. Uggerhøj, B. Dalena, and D. Schulte. Strong field processes in beam-beam interactions at the compact linear collider. *Phys. Rev. ST Accel. Beams*, 17:051003, May 2014.
- [87] KK Andersen, SL Andersen, H Knudsen, RE Mikkelsen, HD Thomsen, UI Uggerhøj, TN Wistisen, Jakob Esberg, P Sona, A Mangiarotti, et al. Measurements of the spectral location of the structured target resonance for ultrarelativistic electrons. *Physics Letters B*, 732:309–314, 2014.
- [88] A. Di Piazza, Tobias N. Wistisen, and Ulrik I. Uggerhøj. Investigation of classical radiation reaction with aligned crystals. 2015.
- [89] J. D. Jackson. *Classical Electrodynamics*. Wiley, New York, 1975.

- [90] M. Abraham. *Theorie der Elektrizität*. Teubner, Leipzig, 1905.
- [91] H. A. Lorentz. *The Theory of Electrons*. Teubner, Leipzig, 1909.
- [92] P. A. M. Dirac. *Proc. R. Soc. London, Ser. A*, 167:148, 1938.
- [93] L. D. Landau and E. M. Lifshitz. *The Classical Theory of Fields*. Elsevier, Oxford, 1975.
- [94] A. O. Barut. *Electrodynamics and Classical Theory of Fields and Particles*. Dover Publications, New York, 1980.
- [95] F. V. Hartemann. *High-Field Electrodynamics*. CRC Press, Boca Raton, 2001.
- [96] F. Rohrlich. *Classical Charged Particles*. World Scientific, Singapore, 2007.
- [97] R. T. Hammond. *Electron. J. Theor. Phys.*, 7:221, 2010.
- [98] A. Di Piazza, C. Müller, K. Z. Hatsagortsyan, and C. H. Keitel. *Rev. Mod. Phys.*, 84:1177, 2012.
- [99] David A. Burton and Adam Noble. *Contemp. Phys.*, 55:110, 2014.
- [100] A. G. R. Thomas, C. P. Ridgers, S. S. Bulanov, B. J. Griffin, and S. P. D. Mangles. *Phys. Rev. X*, 2:041004, 2012.
- [101] A. Gonoskov, A. Bashinov, I. Gonoskov, C. Harvey, A. Ilderton, A. Kim, M. Marklund, G. Mourou, and A. Sergeev. *Phys. Rev. Lett.*, 113:014801, 2014.
- [102] Naveen Kumar, Karen Z. Hatsagortsyan, and Christoph H. Keitel. *Phys. Rev. Lett.*, 111:105001, 2013.
- [103] Matteo Tamburini, Christoph H. Keitel, and Antonino Di Piazza. *Phys. Rev. E*, 89:021201, 2014.
- [104] A. Zhidkov, S. Masuda, S. S. Bulanov, J. Koga, T. Hosokai, and R. Kodama. *Phys. Rev. ST Accel. Beams*, 17:054001, 2014.

- [105] T. G. Blackburn, C. P. Ridgers, J. G. Kirk, and A. R. Bell. Quantum radiation reaction in laser–electron-beam collisions. *Phys. Rev. Lett.*, 112:015001, Jan 2014.
- [106] Thomas Erber. High-energy electromagnetic conversion processes in intense magnetic fields. *Rev. Mod. Phys.*, 38:626–659, Oct 1966.
- [107] N. Neitz and A. Di Piazza. Stochasticity effects in quantum radiation reaction. *Phys. Rev. Lett.*, 111:054802, Aug 2013.
- [108] A. Di Piazza, K. Z. Hatsagortsyan, and C. H. Keitel. Quantum radiation reaction effects in multiphoton compton scattering. *Phys. Rev. Lett.*, 105:220403, Nov 2010.
- [109] F. Mackenroth and A. Di Piazza. Nonlinear double compton scattering in the ultrarelativistic quantum regime. *Phys. Rev. Lett.*, 110:070402, Feb 2013.
- [110] B. King. Double compton scattering in a constant crossed field. *Phys. Rev. A*, 91:033415, Mar 2015.
- [111] Sarah J. M Higgs boson creation in laser-boosted lepton collisions. *Physics Letters B*, 730:161 – 165, 2014.
- [112] Sarah J. Müller, Christoph H. Keitel, and Carsten Müller. Particle production reactions in laser-boosted lepton collisions. *Phys. Rev. D*, 90:094008, Nov 2014.
- [113] Vladimir P. Krainov, Howard R. Reiss, and Boris M. Smirnov. *Appendix J: Properties of the Generalized Bessel Function*, pages 273–275. Wiley-VCH Verlag GmbH and Co. KGaA, 2005.